UNIVERSITY OF COPENHAGEN

FACULTY OF SCIENCE
NIELS BOHR INSTITUTE

MSC. THESIS

Inference of accumulation surfaces by consolidation of isochronous radio-echo sounding data and inverse Monte Carlo method applied on a simple flow model

---

Author:
Jakob Sievers

Academic advisor:
Dr. Aslak Grinsted

December 7, 2010

CENTRE FOR
ICE AND CLIMATE

Dansk resume

I takt med at interessen og bekymringerne omkring den globale opvarmning er steget i de senere år, er det blevet mere afgørende at forstå tidligere tiders klima-ændringer. I den forbindelse er mængden af snefald på den Grønlanske iskappe en god indikator for ændringer. Desuden er tidligere snefald afgørende for forståelsen af iskappers flydning og har derfor mange andre praktiske anvendelser i modellerings henseende.

Den Grønlandske iskappe repræsenterer et kæmpemæssigt klima arkiv. Gennem tiderne er vulkansk materiale fra tidligere udbrud blevet lagret i iskapperne, og disse kan måles vha. radar. Således vil et lag med vulkansk materiale fortælle os en hel del om flydningen siden selve vulkan udbruddet. Selve bestemmelsen af disse interne lag, kaldet *isochroner* fordi at de hver især repræsenterer en enkelt tidsperiode, er dog utrolig tidskrævende, og det meste arbejde med at fortolke data i dette felt er således også kun udført for enkelte radar målinger langs linjer, enten vha. fly eller landbaserede køretøjer. Modeller der er opstillet for at kunne beskrive iskappens flydning og beskrive de isochroner der er observeret er således også fortrinsvist blevet udført i to dimensioner, altså langs en enkelt radar måling, hvor antagelser så er lavet omkring iskappens transverse flydning.

Det har været et primært formål med dette speciale at bestemme snefaldsmængder, ikke kun langs en enkelt linje med radar målinger, men over et kæmpe område, vha. isochrone overflader skabt som samlinger af et større antal af disse enkelte radar linjer. Specifikt har vi analyseret 25 tidsbestemte isochroner i 55 forskellige radar linjer, således at isochrone overflader dækker et kæmpe 3-dimensionelt område mellem NGRIP og NEEM. Ydermere er der blevet opstillet både en 2D og en 3D model til sammenligning af resultater henover selve isdeleren mellem NGRIP og NEEM.

Preface

This thesis constitutes the concluding assignment of the authors' Master degree in Geophysics. It is a 60 ECTS project and have had a time frame of one year. Because courses were taken, and ECTS points awarded, on Svalbard in the fall/winter of 2009, two additional months were given to conclude the study as per standard procedure.

Additional information

University: University of Copenhagen
Institute: Niels Bohr Institute
Department: Centre for Ice and Climate

Author: Jakob Sievers
Signature:

Email: Jakob.Sievers@gmail.com

Study title: Inference of accumulation surfaces by consolidation of isochronous radio-echo sounding data and inverse Monte Carlo method applied on a simple flow model.

Academic advisor: Aslak Grinsted, Centre for Ice and Climate

Submitted: 4th of November, 2010.

abstract

Due to the recent increasing interest in global warming and its implications, an understanding of the highly climate-sensitive past patterns of snow accumulation across glaciers and ice sheets such as Greenland has become essential. The Greenland ice sheet represents a formidable climate archive describing many key factors of past climates. Within the ice sheet internal isochronous layers, reflecting past deposition layers, can be detected by radio-echo sounding techniques. This type of data describes the past flow of the ice sheet and can be directly linked to the accumulation above which feeds the flow. The analysis of such internal layers is however a tedious process and is therefore typically only carried out for single flight lines. The insight into the physical flow field along the internal layer is thus limited by assumptions made about the transverse flow.

In an effort to investigate the differences in results when making assumptions about the transverse flow and when using actual flow, 25 isochronous layers, which are dated from their depths at NGRIP, have been analyzed in a large number of interconnected aerial radio-echo sounding datasets across the Greenland ice sheet to form 25 large isochronous surfaces. A simple two-dimensional and three-dimensional flow model for the Greenland ice sheet has been developed to infer accumulation rates for a number of past periods down to, and including, 7496 yrs before present day, along the NGRIP-NEEM traverse and across said isochronous surfaces. To determine the correct past accumulation patterns, an inverse Monte Carlo method, in the form of a combined Simulated Annealing and Metropolis-Hastings approach, is applied to the simple models. Results from the 2D and 3D models are compared along the NGRIP-NEEM traverse.

Results feature accumulation maps for the times 1981 b2k, 2728 b2k, 3938 b2k 5927 b2k and 7496 b2k, across a large surface in Northern Greenland, covering the NGRIP-NEEM traverse. While results found by the 2D model are trustworthy, results found by the 3D model are slightly affected by the fact that slow model computation time prevented us from reaching an optimal solution using the inverse Monte Carlo approach. Nevertheless they both reveal several interesting aspects of the accumulation pattern, among which its sensitivity to climate changes in coastal regions versus inland regions. Furthermore, the importance of accurate GPS data when assuming no transverse flow because the model is run along the ice divide, is discussed.

Acknowledgments

I would like to thank the following people, marked individually by affiliation, for providing their help, data, experience and encouragement:

- (***CIC***) My thesis advisor Aslak Grinsted for his open door policy and continued help and involvement in this thesis.
- (***CIC***) Michelle Koutnik for her valuable comments and encouragement.
- (***PG***) My Masters advisor Eigil Kaas for his guidance and insight.
- (***UK***) CReSIS for providing their radio echo sounding datasets for the Greenland ice sheet.
- (***CIC***) Hans Christian Steen-Larsen and Susanne Lilja Buchardt, for tracing the original layers used in the 2D case of this study, from the CReSIS dataset.
- (***CIC***) Sebastian B. Simonsen, for providing data concerning the amount of air in the firn across the Greenland ice sheet.
- (***BA***) Dr. Wolfgang Schwanghart for his comments on the use of his topotoolbox.

CIC: Centre for Ice and Climate, University of Copenhagen, Juliane Maries Vej 30, DK-2100 Copenhagen O, Denmark.

PG: Planet and Geophysics, University of Copenhagen, Juliane Maries Vej 30, DK-2100 Copenhagen O, Denmark.

UK: University of Kansas.

BA: Physical Geography and Environmental Change, University of Basel, Klingelbergstrasse 27, CH-4056 Basel/Switzerland

Contents

Acronyms

Below is a list of commonly used acronyms in the present paper:

- **b2k**: Before the year 2000
- **CC**: Camp Century
- **CReSIS**: Center for Remote Sensing of Ice Sheets
- **DEM**: Digital Elevation Model
- **DR**: Data Region
- **EMR**: Electro Magnetic Radiation
- **GIS**: Greenland Ice Sheet
- **GPS**: Global Positioning System
- **HF**: High Frequency
- **ieq.**: Ice Equivalent
- **IRH**: Internal Reflection Horizon
- **MH**: Metropolis-Hastings
- **NGRIP**: North Greenland Ice core Project
- **NEEM**: North Greenland Eemian Ice Drilling
- **RES**: Radio-Echo Sounding
- **SA**: Simulated Annealing
- **UHF**: Ultra High Frequency
- **UTM**: Universal Transverse Mercator (coordinate system)
- **VHF**: Very High Frequency
- **weq.**: Water Equivalent

1 Motivation

As will be established during the present study *isochronous* features, which constitute features of same age, can be detected within glaciers and ice sheets using the technique of Radio-Echo Sounding (RES). Such isochronous features, or *isochrones*, hold valuable information about past climate and flow of the glaciers and ice sheets. To establish the amount of ice on Greenland much aerial RES monitoring has been carried out on the Greenland ice sheet (GIS), providing us with an substantial amount of data. Within these data the isochrones are often discernible for the length of entire RES flights. Based on these, we are thus encouraged to attempt the inferring of past climatic information across large expanses of the GIS.

The analysis of isochrones, in terms of depth, is however a tedious process, slowed down by the often very varied clarity with which the isochrones are undulating through the data. Subsequently most work done in this field has been based on data from single RES flights, and has included assumptions regarding the transverse flow of the ice sheet.

It is the motivation of the present study to analyze isochrones for a large number of interconnected RES flights, thus forming isochronous *surfaces* spanning a large region in the northwestern part of the GIS. We will then attempt to infer past deposition (accumulation) patterns in said region based on a simple flow model. For comparison we setup both a 2D model, in which our model describes the 2-dimensional flow along the traverse between the drillsites NGRIP and NEEM (Fig. 1.1), and a 3D model in which our model describes the 3-dimensional flow in a large region corresponding to the region for which we have analyzed RES flights. We will setup the models such that the accumulation is the parameter to be determined through an inverse method called a Monte Carlo method.

The data used in the 3D model will center around the NGRIP-NEEM traverse to ensure comparability of results. We find that the comparison is an important aspect of the transition into 3D modeling, in that it will likely answer questions pertaining to transverse flows and its effect on the eventual deposition results.

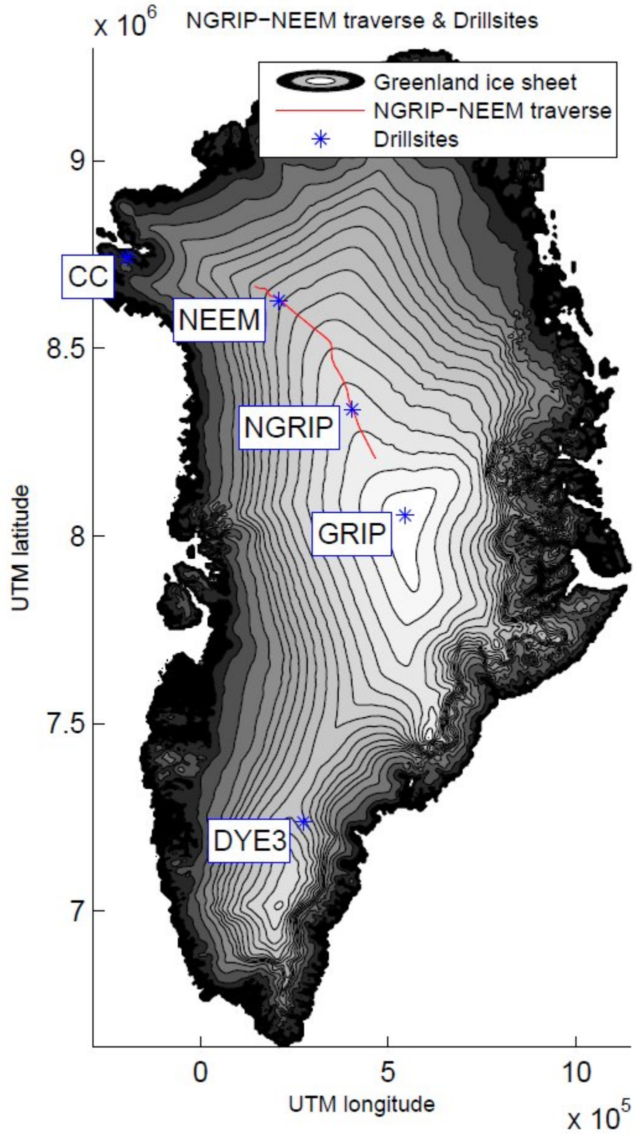

Figure 1.1: NGRIP-NEEM traverse and drillsites across the Greenland ice sheet.

2 Background

The first discoveries suggesting the transparency of glacier ice to electromagnetic radiation (EMR) were made in the 1930s at Admiral Bird's base, in Antarctica, but the origins of the Radio-Echo Sounding (RES) technique can be traced forward to 1946 where American pilots reported that their altimeters were useless when flying over ice masses [Gogineni et al., 1998]. The consequent investigation led in 1957 to the demonstration of the transparency of glaciers to EMR in the VHF[1] and UHF bands [Waite and Schmidt, 1962], as well as allowed for the first determinations of glacier thickness. This led to the development of VHF/UHF radar-systems intended entirely for measurements of ice-thicknesses and basal features of polar glaciers.

In addition to the ice-thickness and basal features, the RES technique was found to also reveal internal layers, also known as *internal reflection horizons* (IRHs), which were traceable for hundreds of kilometers in RES images. These internal features have been attributed to a wide range of physical sources. For shallow IRHs, proposed sources include density change [Harrison, 1973] [Paren and Robin, 1975] [Clough, 1977], and acidity changes as a result of volcanic events [Hammer, 1980] [Hempel et al., 2000]. For deep IRHs however, there is general agreement that density changes alone cannot explain the strength of the observed reflections. Proposed sources at this depth include the aforementioned acidity changes by volcanic events, which here are supported by [Hammer, 1980] [Millar, 1981] [Hempel et al., 2000] who found the layers of changed acidity to coincide with depth of reflection. Another proposed source for deep IRHs is changes in crystal orientation [Harrison, 1973] [Fujita and Mae, 1994]. Layers where the reflecting properties are caused by variations in density or impurity content are generally accepted to be representative of former deposition surfaces, and are as such considered to be layers of equal age, or '*isochrones*', containing valuable climatic information. It is the purpose of this thesis to unearth the part of this information concerning the past accumulation pattern along a single flight line of radar data and across an expansive surface in Northwestern Greenland, composed by a series of interconnected flight-lines.

---

[1] HF: High Frequency 3-30MHz. VHF: Very High Frequency, 30-300MHz. UHF: Ultra high frequency, 300-3000MHz

3 Theory

3.1 Electrical properties of ice

Whatever the underlying reason, internal layers are revealed because of changes in permittivity of the layers in question, which, as we shall see, alters the speed of EMR and thus the return signal picked up during RES operations. The *permittivity*, ε is a measure of a materials ability to *polarize* in response to an incident electric field. To understand the posed connection between impurity content of the ice and its permittivity, a more thorough discussion of polarization is required.

3.1.1 Polarization

Most everyday objects belong to one of two large classes: *conductors* and *insulators* (dielectrics) or a combination of these. Whereas conductors are characterized by having many free electrons that are able to roam around, thus resulting in current, dielectrics, the category to which ice belongs, are characterized by the absence of free electrons. Consequently *stretching* and *rotating* become the principal mechanisms by which a field distorts the charge distribution.

- **Stretching:** Regardless of whether or not an atom is electrically neutral or active, the activation of an electric field on it, will result in shifting of the positive (nucleus) and negative (electrons) charges in the direction of the field and in the opposite direction respectively, thus *polarizing* the atom and giving it an added dipole moment.
- **Rotation:** When applying an electric field to a molecule with an inherent dipole moment, such as the water molecule (Fig. 3.1a), the force on the positive and negative end exactly balance each other provided that the field is uniform. The molecule will however be subject to a torque of strength:

  $$\mathbf{N} = \mathbf{p} \times \mathbf{E}$$

  causing it to rotate such as to align the dipole moment $\mathbf{p}$ parallel to the applied field $\mathbf{E}$.

A closer look at the water molecule reveals that its relatively high inherent dipole moment is caused by the *covalent bonds*[2] joining both hydrogen atoms with the oxygen atom. The resulting direction of the positively charged hydrogen atoms lie toward two of the four vertices of a tetrahedron centered on the oxygen atom (Fig. 3.1b), while the remaining 2 vertices are occupied by negatively charged electron clouds.

Unlike for liquid water, water molecules in ice will, under normal conditions such as atmospheric pressure, form an open hexagonal arrangement[Petrenko and Whitworth, 1999] with each molecule neighboring 4 others and a principal axis[3], or '*c-axis*', directed orthogonally to the hexagonal faces (Fig. 3.2). This arrangement was proposed by

---

[2] ***Covalent bond*:** Chemical bonding characterized by the sharing of pairs of electrons between atoms

[3] ***Principal axis*:** Axis of unique symmetry.

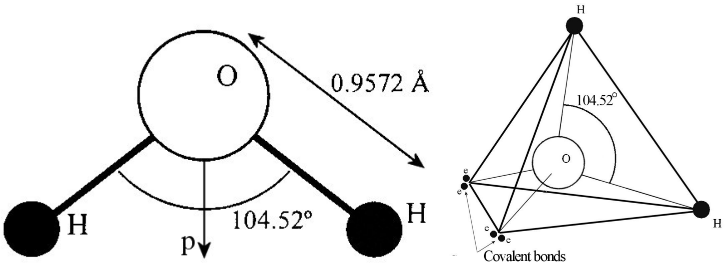

Figure 3.1: **(a)** The dipole moment of a water molecule is directed towards its positively charged hydrogen atoms. **(b)** The two hydrogen atoms and oxygen atom, comprising the water molecule, form a tetrahedron structure with the 2 positively charged (due to covalent bonds with the oxygen molecule) hydrogen atoms directed toward 2 of the 4 vertices, and the remaining 2 vertices occupied by the negatively charged electron clouds.

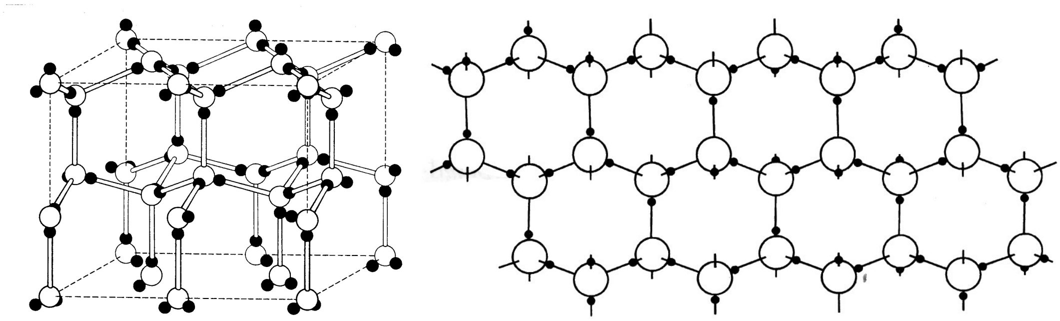

Figure 3.2: **(a)** The open hexagonal arrangement of ice formed under normal conditions. **(b)** The hexagonal arrangement in 2D

[Pauling, 1935] and is called *Ice Ih*, where the '*h*' refers to its hexagonal nature, as opposed to *Ice Ic* which is its cubic form, achieved under different conditions.

Whereas the oxygen atoms are fixed in this hexagonal arrangement, the two hydrogen atoms are not. In fact they are arranged at 'random' apart from their obedience of the Bernal-Fowler rules, which are also the basis for rotation in the crystal lattice [Glen and Paren, 1975]. These are:

1. There must be 2 hydrogen atoms to each oxygen atom.
2. There is only one hydrogen per oxygen-oxygen bond.

The internal re-arrangement of tetrahedra directions when exposed to an electric field, can be explained by violations of one or both of the Bernal-Fowler rules, and the migration of these inside the crystal lattice, as seen in Fig. (3.3). The two types of defects are called *ionic defects* and *bjerrum defects* and arise primarily due to vacancies and dissolved impurities in the ice, as suggested by [Bjerrum, 1951]. From this it becomes clear why ice with varying degree of impurity content will have varying permittivity as well.

Actual measurements [Dowdeswell and Evans, 2004] of the relative permittivity $\varepsilon_r = \frac{\varepsilon}{\varepsilon_0}$ in both *in situ* and laboratory grown ice, suggest linear relationships with ice temperature in the HF/VHF bands (Fig. 3.4) such that:

$$\varepsilon_r = (3.20 \pm 0.02) + 8 \cdot 10^{-4} T \quad , \ \texttt{for 1<f<100MHz} \tag{3.1}$$

$$\varepsilon_r = (3.18 \pm 0.01) + 8 \cdot 10^{-4} T \quad , \ \texttt{for f>100MHz} \tag{3.2}$$

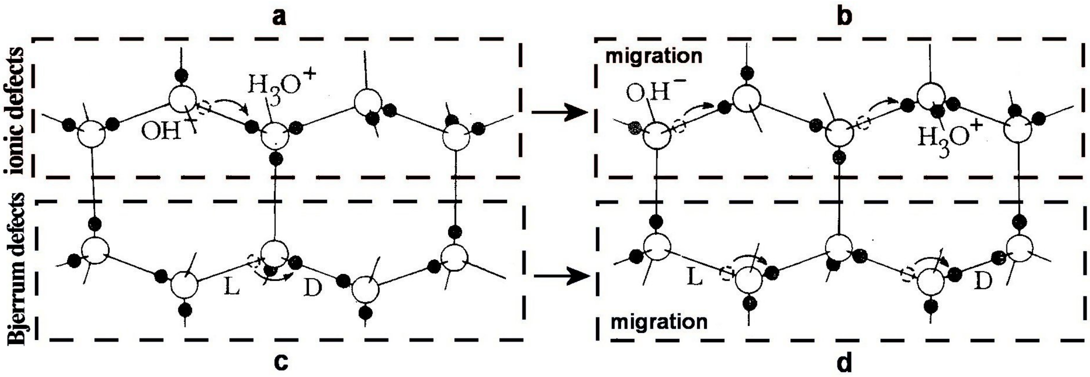

Figure 3.3: **(a)** Ionic defects and **(b)** their ability to migrate. **(c)** Bjerrum defects and **(d)** their ability to migrate. **Picture** taken from [Glen and Paren, 1975].

As will be shown below, this is important for understanding the velocity of EMR in ice.

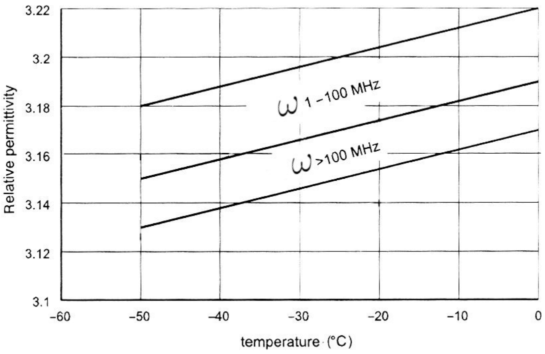

Figure 3.4: Relative Permittivity of ice according to equations eqn. (3.2) and eqn. (3.1). **Picture** taken from [Dowdeswell and Evans, 2004]

It is also worth noting that the anisotropic nature of ice introduces a slight uncertainty in permittivity depending on the angle of signal entry with respect to the hexagonal arrangement:

$$\varepsilon_r^{||} - \varepsilon_r^{\perp} = (0.035 \pm 0.007) + 3.6 \cdot 10^{-5} T$$

3.2 General radio-echo sounding theory

For our purposes, knowing the velocity of EMR, and understanding the reflective properties, within ice, should provide an initial insight into the workings and geometry of the process of radio-echo sounding. The latter, however, requires knowledge about specific properties of the EMR we emit into the ice sheet.

3.2.1 Electric Dipole Radiation

The simplest antennas used for RES are based on dipole radiation. A dipole (Fig. 3.5a) consists of two opposing point charges, $q(t)$ and $-q(t)$, separated by a distance d. While an electric field is always present around electric charges such as $q(t)$ and $-q(t)$, no

EMR is emitted from a static setup or a setup in which the charges have constant velocity, so the point charges are driven back and forth along the wire separating them, at the angular frequency ω:

$$q(t) = q_0 \cos(\omega t)$$

thus constantly accelerating and decelerating. The field created by such a dynamic setup, when observed in a spherical coordinate system, is determined by[Griffiths, 2009]

$$\mathbf{E} = -\frac{\mu_0 p_0 \omega^2}{4\pi}\left(\frac{\sin\theta}{r}\right)\cos\left[\omega(t - r/c)\right]\widehat{\theta}$$

where μ_0 is the permeability of free space, $p_0 = q_0 d$ is the maximum value of the dipole moment, ω is the angular frequency and c is the velocity of the EMR. The energy radiated is determined by the poynting vectors, and the intensity is obtained by time-averaging over one cycle:

$$\mathbf{S} = \frac{1}{\mu_0}(\mathbf{E}\times\mathbf{B}) = \frac{\mu_0}{c}\left\{\frac{p_0\omega^2}{4\pi}\left(\frac{\sin\theta}{r}\right)\cos\left[\omega(t-r/c)\right]\right\}^2\widehat{r} \qquad (3.3)$$

$$\langle\mathbf{S}\rangle = \left(\frac{\mu_0 p_0^2\omega^4}{32\pi^2 c}\right)\frac{\sin^2\theta}{r^2}\widehat{r} \qquad (3.4)$$

where **B** is the magnetic field. There is no radiation from the axis of the dipole. Rather, the intensity assumes a toroidal form (Fig. 3.5b) with its maximum in the equatorial plane. Thus at great distance $r >> 0$ from the source, the electric field imposed on the ice sheet will be planar for the dipole aligned parallel to the surface, which is the case in aerial RES (Fig. 3.6).

Note that the intensity, as given by eqn. (3.4) decreases by a factor of $1/r^2$. This is called the *geometric spreading* which is an essential component of the loss of energy associated with RES. Specifically it describes the loss of wave energy as the wave propagates and is spread out over a bigger area.

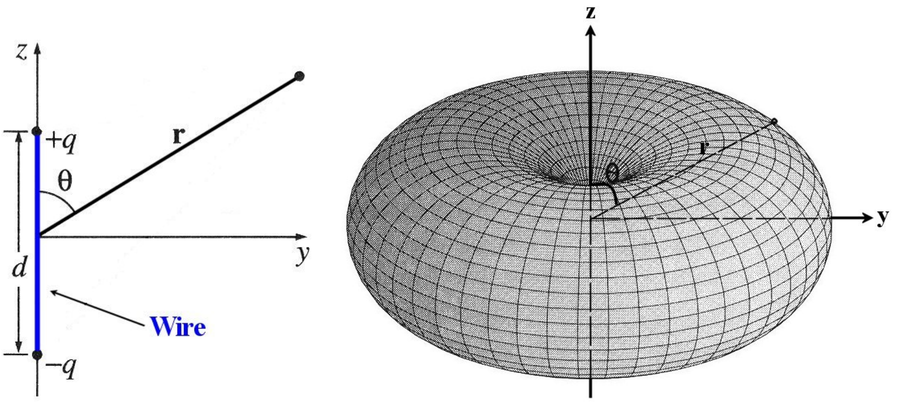

Figure 3.5: **(a)** Dipole setup. **(b)** Intensity pattern of an oscillating dipole. **Pictures** taken from [Hecht, 2008].

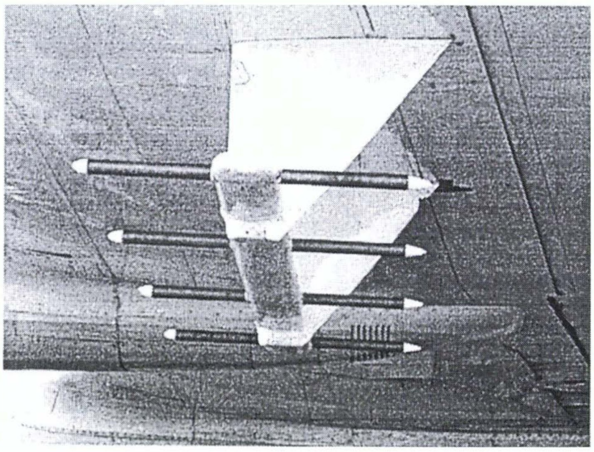

Figure 3.6: The transmit antenna used by CReSIS during the US NASA PARCA effort (described below), here seen mounted under the wing of a NASA P3-B aircraft. **Picture:** taken from [Gogineni et al., 1998]

3.2.2 Electromagnetic Waves in matter

Having determined the planar nature of the imposed electric field on the ice sheet, we are now ready to discuss the propagation of the electromagnetic waves within the ice sheet.

Common for all representations of waves are that they satisfy the wave-equation which in three dimensions is given by:

$$\nabla^2 E = \frac{1}{v^2}\frac{\partial^2 E}{\partial t^2}$$

where E is the wave-displacement, t is the time and v is the wave velocity. The latter is:

$$v = \frac{1}{\sqrt{\varepsilon\mu}} \tag{3.5}$$

for waves in linear homogeneous matter. Here μ is the *magnetic permeability* which is a measure of a materials ability to magnetize in response to an imposed magnetic field. As ice is nonmagnetic $\mu_{ice} = \mu_0 = 1.25 \cdot 10^{-6} NA^{-2}$ (Newton per ampere squared). such waves are conventionally described by the equation[Hecht, 2008]:

$$\widetilde{\mathbf{E}}(z,t) = \widetilde{\mathbf{E}}_0 e^{i(kz-\omega t)} \tag{3.6}$$

Where z is an arbitrary direction for now, t is time, $\widetilde{\mathbf{E}}_0$ is the complex amplitude allowing for all possible polarizations and phases (I.e.: $\mathbf{Re}(\widetilde{\mathbf{E}}_0)$ is the *physical field.*) and k is the angular wavenumber which also provide the wavelength: $\lambda = \frac{2\pi}{k}$.

Suppose now that said wave travels through ice. In such case loss effects will have an effect on the traveling wave, thus altering the velocity described by eqn. (3.5) to[Plewes and Hubbard, 2001]:

$$v_{loss} = \frac{c}{\sqrt{(\frac{\varepsilon_r \mu_r}{2})\left[(1+P^2)+1\right]^2}} \tag{3.7}$$

where μ_r is the relative magnetic permeability ($\mu_r = 1$ for non-magnetic materials such as ice) and $P = \frac{\sigma}{\omega\varepsilon}$ is the *loss factor*. Here σ is the *conductivity*, a measure of a materials ability to conduct a current. $\omega = 2\pi f$ and f is the frequency. The loss effects will be elaborated on shortly.

Using the linear relationships found between ice temperature and ε_r in eqn. (3.2) and eqn. (3.1), results in velocities between:

	1-100MHz	100MHz-10GHz
$0°C$	167.6 ± 0.6	168.2 ± 0.3
$-50°C$	168.6 ± 0.6	169.2 ± 0.3

Table 1: EM wave velocities in ice $[m/\mu s]$

3.2.3 Energy Loss, Attenuation and Geometric considerations

In order to accurately interpret the return signal from the ice sheet during a RES operation, one needs to understand the energy losses occurring as the wave travels, as well as the nature of its path.

Scattering To examine the path of an EMR wave in ice, we consider the case of oblique incidence, onto a boundary between materials with different dielectric properties (Fig. 3.7). The waves involved are the incident (I), reflected (R) and transmitted (T) waves:

$$\begin{aligned}
\widetilde{\mathbf{E}}_I(\mathbf{r},t) &= \widetilde{\mathbf{E}}_{0,I} e^{i(\mathbf{k}_I\cdot\mathbf{r}-\omega t)} \\
\widetilde{\mathbf{E}}_R(\mathbf{r},t) &= \widetilde{\mathbf{E}}_{0,R} e^{i(\mathbf{k}_R\cdot\mathbf{r}-\omega t)} \\
\widetilde{\mathbf{E}}_T(\mathbf{r},t) &= \widetilde{\mathbf{E}}_{0,T} e^{i(\mathbf{k}_T\cdot\mathbf{r}-\omega t)}
\end{aligned}$$

The angles between these, as seen in Fig. (3.7), are determined by:

$$\theta_I = \theta_R \quad , \quad \frac{\sin(\theta_T)}{\sin(\theta_I)} = \frac{n_I}{n_T}$$

The latter being recognized as *Snell's Law* from basic wave theory. Furthermore $n_\chi \equiv \sqrt{\varepsilon_r \mu_r} \approx \sqrt{\varepsilon_r}$ is the *index of refraction* for the material properties on each side of the boundary, identified by the subscript χ. The apparent change in angle of the transmitted wave, with respect to the incident wave, is called the *refraction*.

Furthermore the polarization and strength of the resulting wave amplitudes are described by the Fresnel equations[Hecht, 2008]:

$$\begin{aligned}
\left(\frac{E_{0R}}{E_{0I}}\right)_\perp &= \frac{\frac{n_I}{\mu_I}\cos\theta_I - \frac{n_T}{\mu_T}\cos\theta_T}{\frac{n_I}{\mu_I}\cos\theta_I + \frac{n_T}{\mu_T}\cos\theta_T} \\
\left(\frac{E_{0T}}{E_{0I}}\right)_\perp &= \frac{2\frac{n_I}{\mu_I}\cos\theta_I}{\frac{n_I}{\mu_I}\cos\theta_I + \frac{n_T}{\mu_T}\cos\theta_T}
\end{aligned}$$

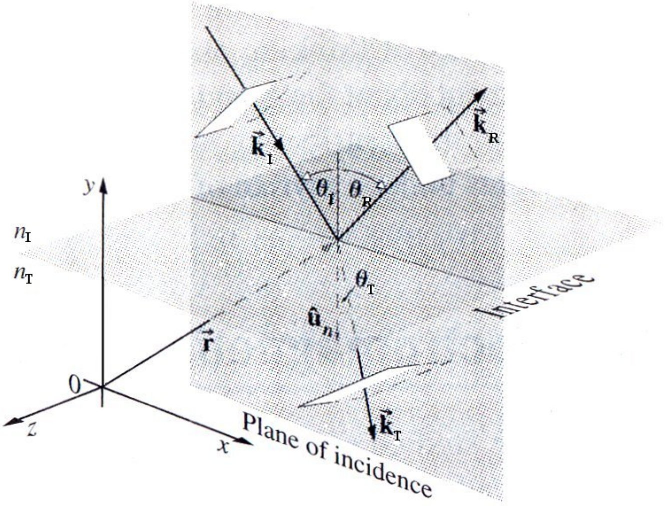

Figure 3.7: Plane EMR waves incident on a boundary between two media of different dielectric properties. **Picture** taken from [Hecht, 2008].

Which for dielectrics where $\mu_I \approx \mu_T \approx \mu_0$ and in the setting of aerial RES with $\theta_I \approx \theta_R \approx \theta_T \approx 0$, reduces to:

$$\begin{aligned} R_\perp &\equiv \left(\frac{E_{0R}}{E_{0I}}\right)_\perp = \frac{n_I - n_T}{n_I + n_T} = \frac{\sqrt{\varepsilon_I} - \sqrt{\varepsilon_T}}{\sqrt{\varepsilon_I} + \sqrt{\varepsilon_T}} \\ T_\perp &\equiv \left(\frac{E_{0T}}{E_{0I}}\right)_\perp = \frac{2n_I}{n_I + n_T} = \frac{2\sqrt{\varepsilon_I}}{\sqrt{\varepsilon_I} + \sqrt{\varepsilon_T}} \end{aligned}$$

This shows how the amplitude of the transmitted wave remains in phase with that of the incident wave, whereas the amplitude of the reflected wave shifts polarization $180°$ if $n_T > n_I$. The index of refraction for ice is $n_{ice} = 1.31$ meaning that for aerial RES 93.3% of the emitted EMR is being transmitted and 6.7% is being reflected at the boundary between air and ice.

Previously we have established that IRHs within the ice sheet are caused primarily by impurities in the form of volcanic fallout. Since each volcanic eruption is different in terms of fallout content it becomes clear that the reflection/transmission events taking place within the ice sheet as it is penetrated by EMR are very difficult to predict as well. Although many individual components exist in volcanic fallout, sulphuric acid, which has a refractive index of $n_{sulphur} = 2$, is among one of the primary.

The geometry of reflection events, and thus the return signals, can be quite complicated [Gruber and Ludwig, 1996] with events ranging from *specular*, in which reflected incident EMR is re-radiated in one specific direction (for smooth surfaces), **diffuse** where reflected incident EMR is re-radiated in all directions (for surfaces with texture on about the same scale as the EMR wavelength), or more likely **Lambertian** which is a combination of the two previous types (Fig. 3.8). To further complicate the situation, the boundary on which the signal impinges and is reflected, is naturally rarely flat and will therefore encourage diffraction events, which involves the spreading and focusing of wave signals as they are refracted through localized areas of different refractive index.

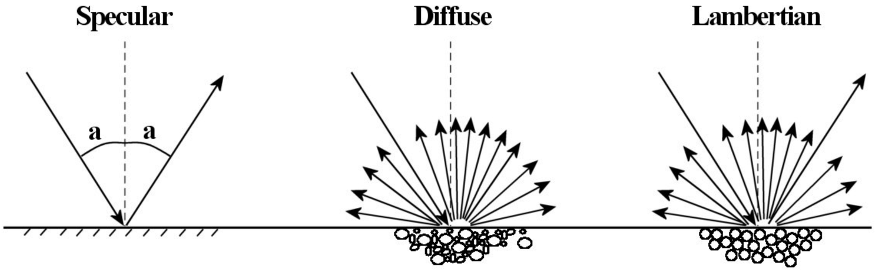

Figure 3.8: Reflection events are either *specular*, *diffuse* or the more likely combination, or '*lambertian*'. **Picture** taken from [Gruber and Ludwig, 1996]

Attenuation While not affecting the path of a wave, the attenuation of the propagating wave is critical for the interpretation of the return signal. The unattenuated wave eqn. (3.6) is easily modified to also include attenuation effects, by rendering the wave number into a complex number, $k \to \widetilde{k} = k + i\kappa$:

$$\widetilde{\mathbf{E}}(z,t) = \widetilde{\mathbf{E}}_0 e^{i(\widetilde{k}z - \omega t)}$$

with

$$k \equiv \omega\sqrt{\frac{\varepsilon\mu}{2}}\left[\sqrt{1+\left(\frac{\sigma}{\varepsilon\omega}\right)^2}+1\right]^{1/2} \quad , \quad \kappa \equiv \omega\sqrt{\frac{\varepsilon\mu}{2}}\left[\sqrt{1+\left(\frac{\sigma}{\varepsilon\omega}\right)^2}-1\right]^{1/2} \tag{3.8}$$

where κ is the *attenuation coefficient* [Griffiths, 2009].

- **The imaginary part** κ results in an attenuation of the wave with distance z:

  $$\widetilde{\mathbf{E}}(z,t) = \widetilde{\mathbf{E}}_0 e^{-\kappa z} e^{i(kz - \omega t)}$$

  thus resulting in a *skin depth* $d \equiv \frac{1}{\kappa}$ signifying the depth at which the energy is reduced by a factor of $\frac{1}{e}$.

- **The real part** k determines the wavelength, the propagation speed and the index of refraction in the usual way:

  $$\lambda = \frac{2\pi}{k} \quad , \quad v = \frac{\omega}{k} \quad , \quad n = \frac{ck}{\omega}$$

Examining the loss factor and eqn. (3.8) we can conclude the following:

- Materials with no or little loss does not attenuate EMR ($\kappa = 0$). I.e.: The energy of the EMR wave will be used to polarize the atoms in the material and is subsequently re-emitted back toward the aerial RES receiver, thus providing great EMR depth penetration.

- Materials with loss attenuate EMR to an extent determined by the ratio σ/ε. Specifically this means that materials with high conductivity limit the EMR depth penetration as the emitted energy is converted into heat rather than stored and returned to the receiver. Reversely, materials with high permittivity will ensure greater depth penetration since more energy is used to polarize atoms, and subsequently re-emitted back toward the aerial RES receiver.

- Resolution is a measure of the ability to differentiate between reflectors adjacent to each other in space or time. It can be shown that attenuation eqn. (3.8) is positively proportional to frequency, and signal penetration must therefore be traded off against resolution which is improved at high frequencies.

An illustration of a typical raw data output by an airborne RES operation is seen in Fig. (3.9a). After post processing [Paden et al., 2010] the data might look something like that seen in Fig. (3.9b), clearly indicating the presence of an IRH along the flightpath. The post processing is however beyond the scope of this project and will not be discussed further.

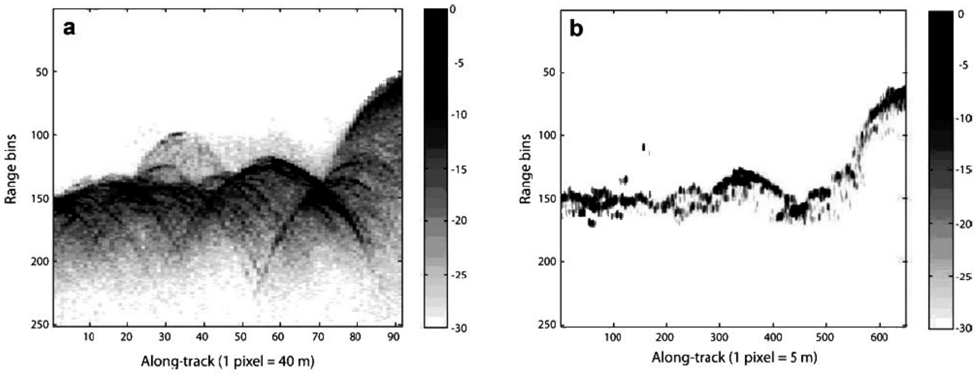

Figure 3.9: **(a)** Raw RES data. **(b)** RES data after post processing, clearly indicating the presence of an IRH along the flightpath. **Pictures** taken from [Paden et al., 2010].

4 Data

The following is a detailed description of the types of data used in the present study.

4.1 RES data used

Following the discovery of the RES method, airborne RES campaigns, aiming at large-scale coverage, were carried out on Antarctica and Greenland throughout the late 60s and 70s, by Cambridge's *Scott Polar Research Institute* (SPRI), *U.S. National Science Foundation* (NSF) and the *Technical University of Denmark* (DTU) [Gogineni et al., 1998]. Subsequent airborne RES campaigns, both on Antarctica and in Greenland, were however directed towards specific and very localized scientific activities only. For the case of Greenland this changed with the initiation in 1991 of the US NASA PARCA (*Program for Arctic Regional Climate Assessment*) polar research initiative which by coordinated surface, airborne and space borne measurements, aimed at determining the mass balance of the Greenland ice sheet. In accordance with this initiative, the *Center for Remote Sensing of Ice Sheets* (CReSIS) at the University of Kansas, US, began in 1993 conducting an extensive airborne RES survey of Greenland. The radar system used during this survey operated at a transmitting power of 200W with a center frequency of 150MHz, a bandwidth of 20MHz and a pulse duration of $3\mu s$ or $10\mu s$. The depth- and horizontal-resolution of this system was 4.2m and 160m respectively and the aircraft position was determined by GPS. The flight lines can be seen in (Fig. 4.1), color-coded for year of surveying.

As we will be using both single isochrones in the 2D case, and isochronous surfaces composed of several single isochrones, in the 3D case, care must be taken to maintain consistency in their naming. Thus isochronous features in the 2D and 3D case will henceforth always be referred to as *isochronous layers* and *isochronous surfaces* respectively, and both as *isochrones* in general. To that end the following data is used:

4.1.1 NGRIP-NEEM traverse

The isochronous layers used in the 2D part of this study consist of an analysis of IRHs along the ice divide between the ice core drilling sites NGRIP and NEEM (Fig. 4.2) constituting a single flight line originally recorded during the CReSIS effort under the US NASA PARCA initiative during the summer of 2007. The analyzed data, which are kindly provided by S.L. Buchardt[4] through her PhD-thesis [Buchardt, 2009], encompass a 435km long section, beginning 50km upstream from NGRIP and ending 20km downstream from NEEM. It describes the undulations of 25 isochronous layers, each dated very accurately from their depths at NGRIP using the GICC05 timescale [Vinter et al., 2006]. All ages and depths at NGRIP for the 25 en-glacial isochrones are listed in the appendix (section 12).

---

[4] **S.L. Buchardt:** *Centre for Ice and Climate*, University of Copenhagen, Denmark

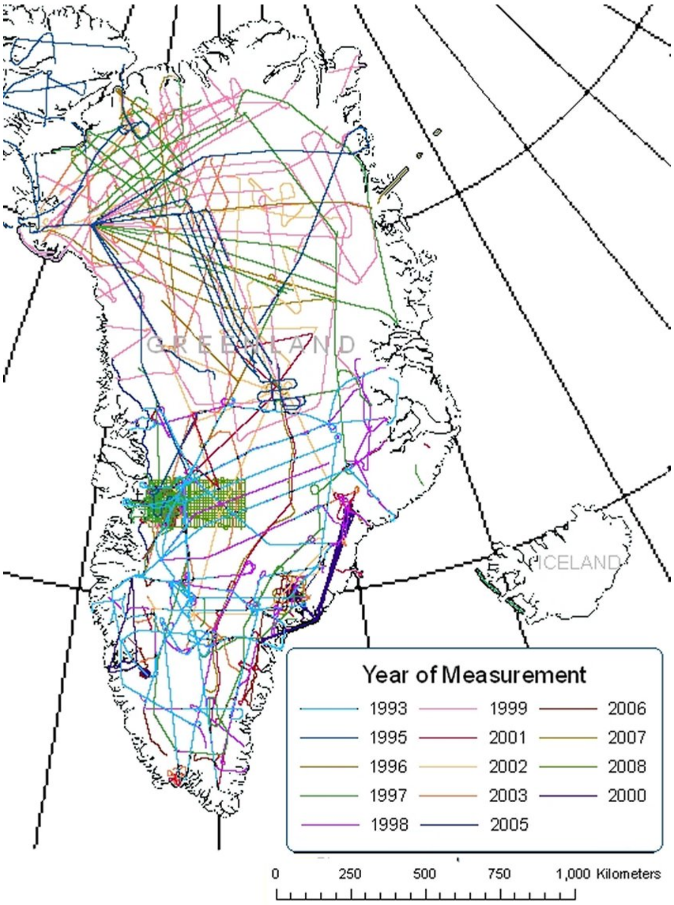

Figure 4.1: RES Flights conducted by CReSIS as part of the US NASA PARCA initiative. **Picture** provided by CReSIS

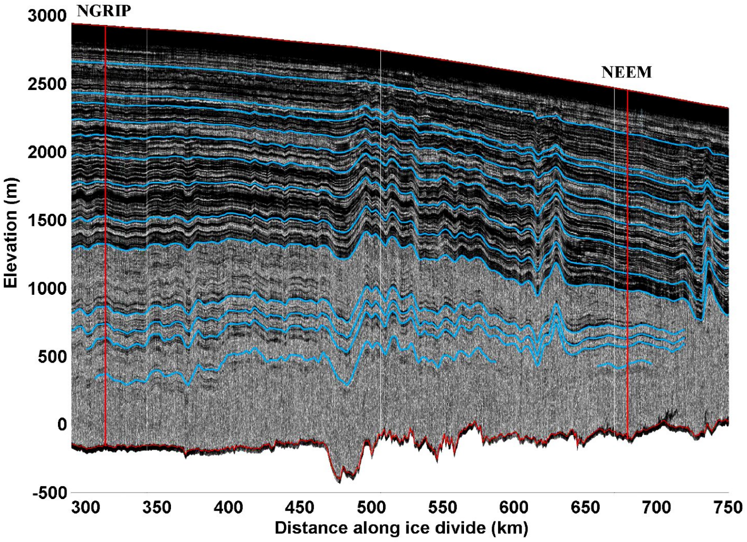

Figure 4.2: RES image collected along the ice divide separating NGRIP and NEEM. A selection of 13 out of 25 en-glacial isochronous layers are marked in Blue. **Picture** taken from [Buchardt, 2009].

As established in the work of [Buchardt, 2009] the deep IRHs coincide with variations in DC conductivity of ice from the NGRIP borehole. This supports the scenario of deep reflections by the presence of volcanic impurities. Note the three significant undulations in isochronous layers located approximately 475km, 625km and 730km downstream along the ice divide in (Fig 4.2). While the first feature is most likely caused by the clear change in bedrock topography, the two others cannot be explained this way. They are more likely attributable to changes in accumulation rate, variations in ice flow perpendicular to the ice ridge and changes in the geothermally induced basal melt rates. The two former causes are accounted for in the 3D approach.

4.1.2 Consolidating radio-echo sounding data

For the 3D case we downloaded from the CReSIS server a total of 1951 individual flight line segments (or 38.6GB of data), in the form of matlab-files, which combined make up the flight patterns seen in (Fig. 4.1). It should be noted that each individual flight line were often subdivided into several segments so the actual number of independent flights are significantly less than 1951. Contrary to expectations, individual files did not adhere to any unified style of labeling and consequently much work went into extracting data and arranging it in a unified scheme for subsequent analysis of IRHs. For this analysis we setup a matlab routine allowing for tracing of these isochronous features both manually and automatically. For consistency, the NGRIP-NEEM traverse data, used in the 2D case, were used as a starting point from which the grid of isochronous data were expanded as more flight lines were analyzed and added to the grid continuously. The raw data output following the entire process of analysis consists of a very large number of individual [*latitude*,*longitude*,*depth*]-points in 3D space for each of the 25 ages to which isochronous features where analyzed in [Buchardt, 2009]. A total of 55 individual flight line segments were analyzed this way.

The increased visibility of faint layer undulations in my visualization of the data, prompted a slight correction of the data provided by S.L. Buchardt. This correction affected the NGRIP region as well, thus calling for a re-dating of the newfound depths using the GICC05 timescale [Vinter et al., 2006]. As the correction occurred in the 11th hour of the study, all 2D results are still based on the original depths and ages provided in [Buchardt, 2009]. The re-dated ages found for the isochrones chosen for the actual modeling does however only deviate 17 years, or $2.6m$, on average, from those used in the 2D case (See Tab. 2), and we therefore feel that the 2D and 3D results remain very comparable.

The expanse of the analyzed grid of interconnected flight lines can be seen in Fig. (4.3) and a more detailed description of the analysis routine is found in the appendix (section 11).

4.2 Geographical Greenland data

Apart from RES data, geographical data describing the ice sheet surface and bedrock were also needed. All data were provided in a 5km grid by a website[5] hosted at the University of Montana. The data provided have been collected from many sources:

---

[5] http://websrv.cs.umt.edu/isis/index.php/Present_Day_Greenland

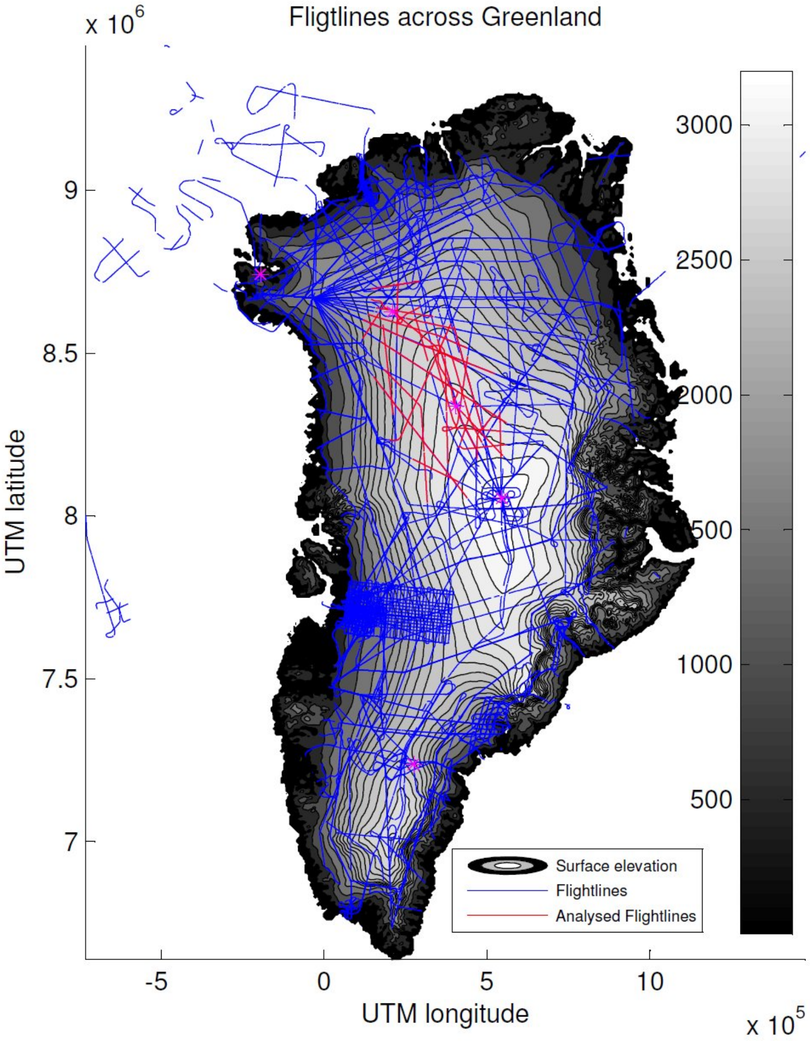

Figure 4.3: Flight lines across Greenland. Blue lines signify lines that have yet to be analyzed whereas red lines signify those already analyzed. Ice core drilling sites are marked by purple stars. from south to north: Dye3, GRIP, NGRIP, NEEM, Camp Century.

Bedrock and ice thickness: Bedrock and ice thickness data is taken from [Bamber et al., 2001]. As part of CReSIS' involvement in the US NASA PARCA initiative to determine the mass balance of Greenland, a coherent ice penetrating radar system was developed and used from 1993-1999. The radar system operated at 150MHz with a chirped $1.6\mu s$-pulse and peak power of 200W. Data from an old ice thickness grid developed from data collected during the 1970s [Letreguilly et al., 1991] was used to fill in the gaps of the CReSIS measurements, despite its markedly lower quality [Bamber et al., 2001]. Both bedrock and ice thickness can be seen in Fig. (4.4).

Present precipitation pattern: Present precipitation is provided for the entire region of Greenland and surrounding ocean by [Ettema et al., 2009]. The data is achieved by regional climate modeling using the regional atmospheric climate model RACMO2/GR at unprecedented high horizontal resolution of $\approx 11km$. The atmospheric part of the model is forced at the lateral boundaries and the sea surface by the global model of the *European Centre for Medium-Range Weather Forecasts* (ECMWF) with simulations covering the period of September 1957 to September 2008 (September 1957 to September 2002 being data from the ERA-40 re-analysis). The resulting data were subsequently interpolated to the 5km grid by natural neighbor interpolation (based on Delaunay triangulation). The present precipitation pattern can be seen in Fig. (4.4).

Present surface velocity: Present surface velocity is a composite map of 5 years of observations (2000, 2005-2008) using RADARSAT interferometric synthetic aperture radar (InSAR) data and optical-image-tracking methods. Data from two such years of survey are described in detail in [Joughin et al., 2010]. The map is limited by gaps in satellite coverage and by InSAR variability in regions with high accumulation rates and will primarily be used to justify the use of balance velocities later in the present paper. The present surface velocity can be seen in Fig. (4.4).

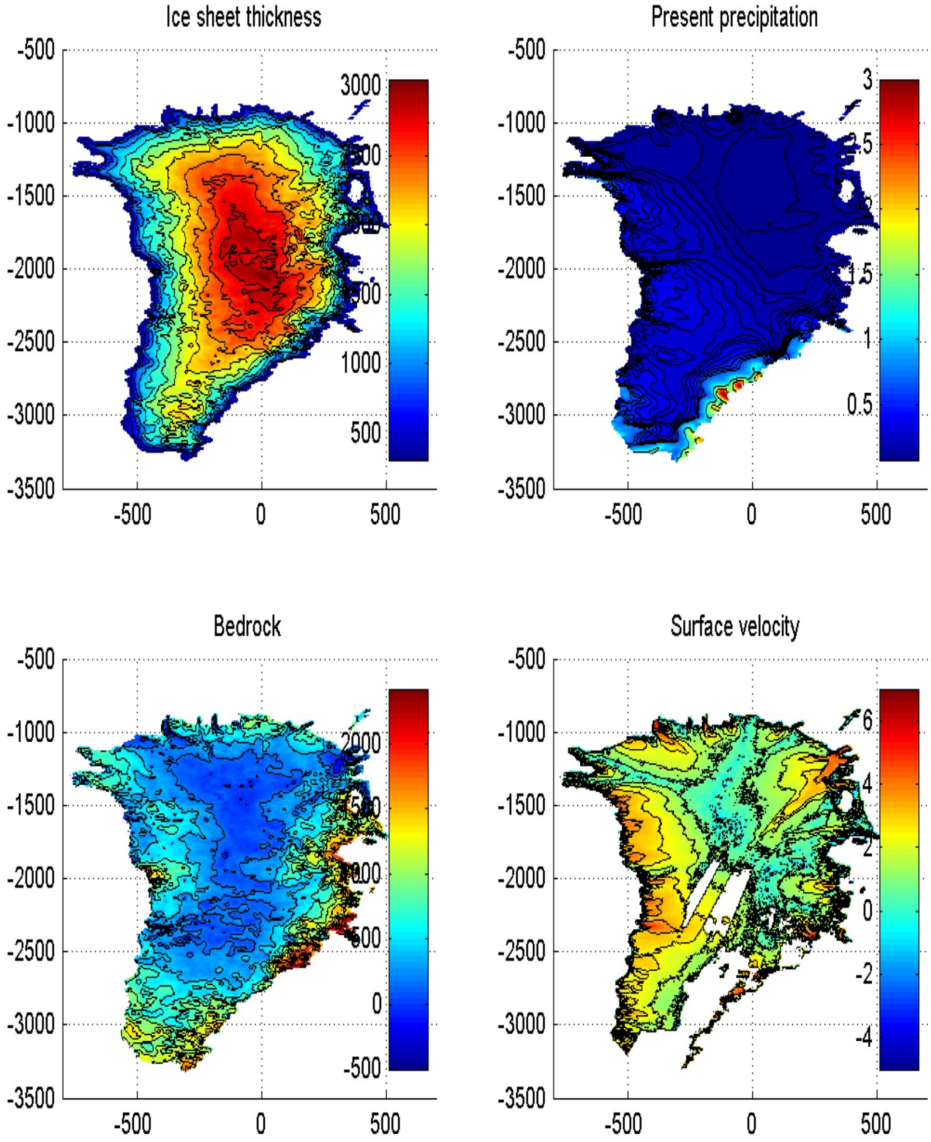

Figure 4.4: Datasets of ice sheet thickness, present precipitation, bedrock and surface Velocity. White regions in the surface velocity are areas where there is no data cover.

5 Modeling the ice flow

A simple model for the flow of an ice sheet in both 2D and 3D settings will now be developed. To maintain consistency and comparability between the results found for the 2D and the 3D case a high degree of similarity between the two models is essential. Furthermore a certain degree of theoretical simplicity is required as computational limitations rapidly become a very real factor when dealing with 2D and 3D models in particular.

For our purposes, a model should for realistic values of accumulation trace ice particles vertically and horizontally from the surface of the ice sheet for specific lengths of time, corresponding to the ages of the individual isochrones used. The end-pattern of particles constitute modelled isochrones. The misfit between these modeled isochrones and the actual measured isochrones allow for a minimization by way of inverse methods to determine the most likely accumulation pattern for a given time. The inverse method is described in section 6.

The steps in defining the presented flow model includes describing:

- geographical constraints on the problem, based on our data coverage.
- the number and age of isochrones used to infer accumulation patterns from.
- the vertical and horizontal velocities present within the modeled ice sheet.
- how we trace particles into the ice sheet.
- smoothing of data
- the use of ice equivalent values.

5.1 The data region

The first task is to define a data region (DR) corresponding to the region in which we have data. This is important because we are using isochrones from different depths and each are likely to cover different regions. Apart from ensuring equal coverage of all data, we also require the data to be on the same grid. Both requirements are easily met for the 2D case as much of the work concerning the preparation of data has been done by [Buchardt, 2009]. It is merely the case that our information on bedrock, surface and isochronous layers overlap for a certain length only, prompting a simple cropping of some of the data.

For the 3D case however the problem is less straightforward. When choosing a set of isochronous surfaces to model from, the different surfaces will inevitably cover different areas. The difference in coverage occurs because not all 25 isochronous surfaces were traceable in all RES datasets (flight lines). Again we require all information to be on the same grid and covering the same region. Remember that each isochronous surface in fact consists of a large set of single points determined during the tracing in the radar datasets. Equal coverage is therefore ensured by finding the minimum and maximum x and y coordinates of each individual dataset and then choosing the maximum of all the minimum values and vice versa, to represent the DR. This amounts to defining rectangular boundaries around each dataset, such as shown in Fig. (5.1a), and defining the actual boundary in which data from all individual rectangles exist, as the inner rectangle.

It is clear however from a closeup of the analyzed flight lines seen in Fig. (5.1b) that placing squares around the data will inevitably result in regions of no actual data coverage and we thus also choose to add the minimum and maximum of x+y and x-y constituting lines angled at $45°$ and $-45°$ respectively, as well as a few manually chosen points in the West to South-Western part of the DR. This further constrains the DR to the area containing actual data (illustrated by the blue line in in Fig. 5.1b). As expected some flight lines in Fig. (5.1b) cross the DR boundaries, illustrating well the case of different coverage by different isochronous surfaces. Once the boundaries of the DR has been obtained we formulate a uniform grid based on the rectangles surrounding the DR and perform gridding by kriging to determine values at each grid point for each isochronous surface depth. The consequent recurring extrapolation of data outside the DR toward the SW, NW, SE and NE is irrelevant as we will not use data from these regions. Thus we have determined a series of isochronous surfaces from a consolidation of isochronous layers throughout the ice sheet. An example of one such isochronous surface is illustrated in Fig. (5.2).

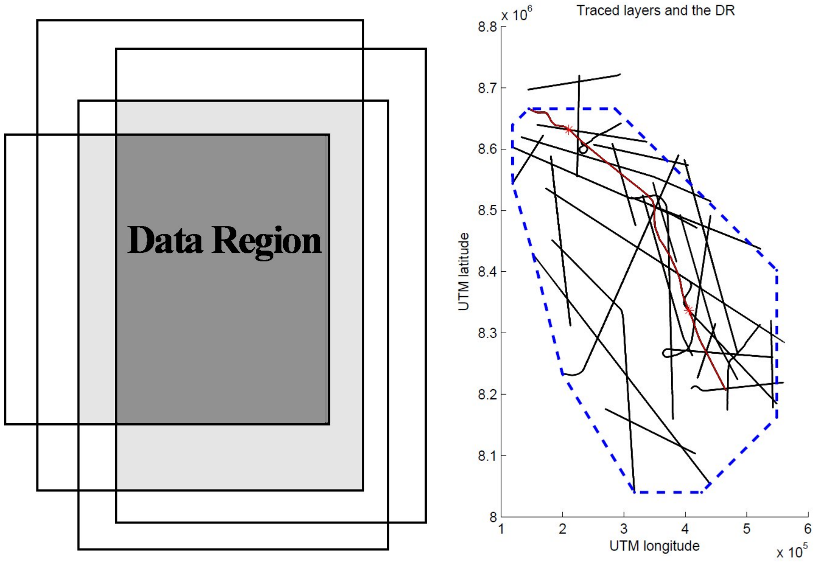

Figure 5.1: **(a)** The square data regions. **(b)** Traced flight lines constrained by a decagon drawn in blue. Flight lines outside the DR are caused by inconsistencies in coverage of the set of n isochrones chosen for the analysis. The NGRIP-NEEM traverse and drillsites are marked in red.

5.2 Choice of Isochrones

The choice of isochrones used in the coming analysis is made from the following requirements:

1. Isochrones must be of same age in both the 2D and 3D model.
2. Isochrones must have reasonable coverage in both the 2D data and the 3D data.

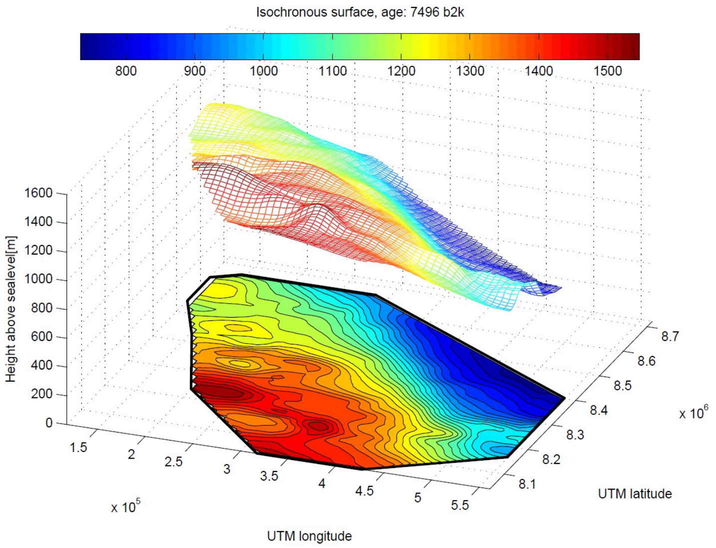

Figure 5.2: An example of an isochronous surface within the DR dated at 7496 b2k.

3. No isochrones older than 9700 b2k (before the year 2000) are allowed.

4. Reasonable difference in age between individual isochrones such as to cover the entire age scale evenly.

(1) Maintains comparability. As mentioned before the isochrones are strictly speaking not of same age due to a last minute correction of the 3D data. They are however very alike in age and comparability is thus ensured. **(2)** The coverage is acceptable for all isochronous layers. The same can however not be said for the isochronous surfaces. Therefore the requirement eliminates the use of the most recent isochrone at 1371 b2k, which was notoriously difficult to track away from the NGRIP-NEEM ice-divide traverse. **(3)** Due to an assumption of steady state we are not allowed to use isochrones from pre-holocene times (older than 9700 b2k). This will be elaborated on shortly. **(4)** Prevents unnecessary strain on the computer by limiting the number of time-periods evaluated.

In the end, isochrones representing accumulations at the following times and depths (at NGRIP) have been chosen for analysis in the 2D and 3D cases respectively:

age (b2k)	Depth (m)
1951	372.4
2736	501.1
3962	688.9
5913	954.6
7487	1146.3

age (b2k)	Depth (m)
1981	377.9
2728	499.9
3938	685.4
5927	956.5
7496	1147.4

Table 2: Ages and depths at NGRIP for all isochrones used in this study. **(Left:)** 2D data. **(Right:)** 3D data.

5.2.1 Horizontal velocity

A key assumption of the presented approach is that the geometry of the ice sheet is in steady state. Effectively this forbids the use of isochrones dating back to pre-holocene times. It does however allow us to use the theory of balance velocities to determine the depth averaged horizontal velocity $\overline{u}(z)$. The accuracy of such method was determined by [Bamber et al., 2000] who evaluated the difference between the results of a balance velocity model and regional surface velocities found by synthetic-aperture radar interferometry (InSAR) as well as a series of inland GPS-derived velocities. He found a high degree of agreement between balance velocities and InSAR/GPS in the inland regions but found the balance velocities to be unreliable at the ice sheet margins where errors in ice thickness, surface slope and ablation rate are large. Thus we have avoided analyzing data close to the ice sheet margin.

Horizontal velocities in the 2D case For the 2D case, in which the region of interest experiences little accumulation and low surface velocities (see section 5.10), we assume that changes in accumulation within the range specified below in section 6 will cause only little change in surface velocity. We shall therefore adopt the surface velocity u_s along the NGRIP-NEEM traverse, as found by [Buchardt, 2009], and apply it vertically throughout the ice sheet for the duration of the inverse routine, described below. The use of u_s as a depth averaged velocity for both the 2D and the 3D case, is justified both by [Bamber et al., 2000] who finds that the ratio of $\overline{u}(z)/u_s$ to be 0.87-1.00 and by [Hvidberg, C. & Grinsted, A. - personal communication] who estimate the ratio to be even closer to unity for this region.

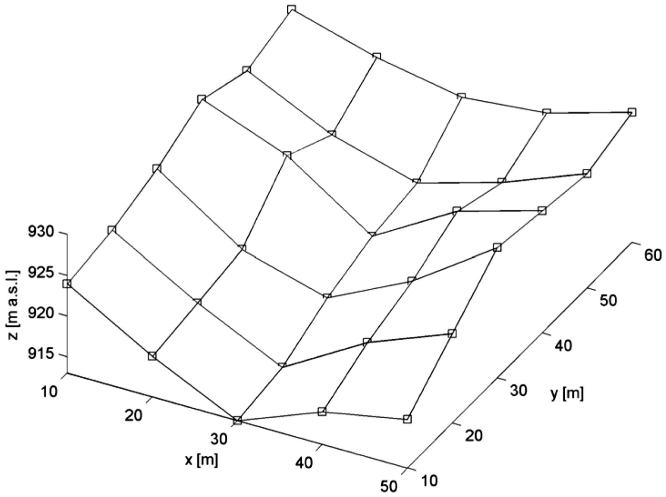

Figure 5.3: A digital elevation model **Z** of size $[m, n]$ used to illustrate the workings of the topotoolbox. **Picture** taken from [Schwanghart and Kuhn, 2010].

Horizontal velocities in the 3D case Contrary to the 2D case, the 3D case feature both faster horizontal velocities and higher accumulation rates. We therefore expect changes in horizontal velocity to have an effect in the 3D case and will therefore recalculate it continuously during the inverse routine. To calculate the balance velocity in the 3D case, we use a matlab toolbox called *topotoolbox*. This toolbox contains utilities for relief analysis in a hydrological and geomorphological context, involving digital elevation models (DEM), material fluxes and the spatial variability of physical and chemical tracers. This description follows [Schwanghart and Kuhn, 2010]. Given a DEM **Z** as a matrix of size $[m, n]$ (Fig. 5.3), the toolbox can be used to first calculate an *adjacency matrix*, **A(Z)** $= [a'_{ij}]$. When **Z** has $k = n \cdot m$ elements, the adjacency matrix is of size $[k, k]$ with $a'_{ij} = 1$ when a cell with the linear index *i* is a neighbor of cell *j*, and $a'_{ij} = 0$ otherwise (See Fig. 5.4a). Since **A** is populated primarily by zeros $(> n^2 - 8n)$ it can be classified as sparse. Sparse matrices are indicative of loosely coupled systems and allow for efficient storage organization as well as computation time proportional to the number of arithmetic operations on non-zero elements.

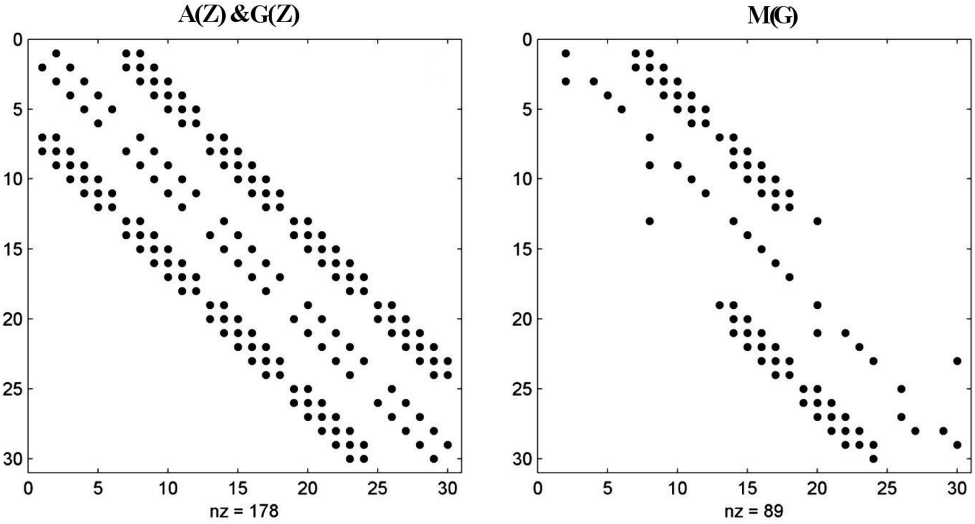

Figure 5.4: **(a)** Sparsity patterns for both the adjacency matrix $\mathbf{A}(\mathbf{Z})$ and the gradient matrix $\mathbf{G}(\mathbf{Z})$. **(b)** Sparsity pattern for the transfer matrix $\mathbf{M}(\mathbf{G})$. **Pictures** taken from [Schwanghart and Kuhn, 2010].

From the same DEM we can determine the gradient matrix **G**. For neighbor cells *i* and *j*, the matrix contains the elements:

$$G_{ij} = \frac{Z_i - Z_j}{d_{ij}}$$

where $d_{ij} = \sqrt{(X_i - X_j)^2 + (Y_i - Y_j)^2}$ is the distance between the neighboring cells. The result is the same sparsity pattern found in **A** but with negative and positive values depending on the slope. Thus **G** indicates both type, magnitude and direction of the gradient at any point across the DEM.

From **G** flow directions are determined using a multiple flow direction approach in which the discharge in each cell is partitioned and transferred to all downward neighbor cells, thus allowing for bifurcation and convergence of flow. This information constitutes the transfer matrix **M** in which the elements m_{ij} contains the relative discharge from a cell *i* to all 8 surrounding particles with index *i*. **M** is created from the slope matrix **G** by replacing all negative entries with zero and thereafter scaling all non-zero values along each row such that the sum of each row equals unity. In this way all local minima (cells surrounded only by cells that have higher elevation) are treated as flat areas over which the flow continues unhindered. In conclusion, rows of **M** hold information on the relative amount of discharge to surrounding cells, and columns hold information about how much discharge is gained by this one cell by its surrounding neighbors. The resulting sparsity pattern of the transfer matrix $\mathbf{M}(\mathbf{G})$ can be seen in Fig. 5.4b.

Finally the upslope contributing drainage area, which serves as a measure of discharge in many modeling approaches, can be determined by counting the number of cells draining in each grid cell. Let Q_i denote the storage of ice in cell $i = 1, ..., n$, and f_{ij} the flow from cell *i* to *j*. Assume that each flow f_{ij} depends on the storage Q_i and distribution ratio m_{ij} such that $f_{ij} = m_{ij} Q_i$. We can now formulate the differential equation for storage in each cell:

$$\frac{dQ_i}{dt} = \sum_{j=0}^{n} f_{ij} - \sum_{j=0}^{n} f_{ji} = \sum_{j=0}^{n} m_{ij} Q_i - \sum_{j=0}^{n} m_{ji} Q_j$$

where $m_{ii} = 0$. f_{0i} and f_{i0} are the external inflow and outflow rates in each cell, recognized as the accumulation and ablation, respectively. A steady state assumption implies:

$$\sum_{j=0}^{n} m_{ij} Q_i - \sum_{j=0}^{n} m_{ji} Q_j = 0 \tag{5.1}$$

The sum of the distribution ratios m_{ij} equal one all cells *i* where any $m_{ij} \neq 0$

$$\sum_{j=0}^{n} m_{ij} = 1 \tag{5.2}$$

Otherwise $m_{ij} = m_{0j} = 1$ and *i* is a sink. Incorporating this into a steady state flow calculation for a constant external inflow rate of f_{0i} in each cell *i*, eqn. (5.1) and eqn. (5.2) can be combined as:

$$\sum_{j=1}^{n} Q_i - \sum_{j=0}^{n} m_{ji} Q_j = f_{0i}$$

This can be written in matrix notation as:

$$\left(\mathbf{I} - \mathbf{M}^{T}\right) Q' = \mathbf{f0} \tag{5.3}$$

where **I** is the identity matrix and $\mathbf{M}^{T}$ is the transpose of the flow direction matrix. Q' is a $k \times 1$ vector containing the ice storage values in each cell and **f0** is a $k \times 1$ vector where the values correspond to the inflow rates in each cell, i.e. the accumulation. Since we desire knowledge on the storage in each cell we rearrange eqn. (5.3):

$$Q' = \left(\mathbf{I} - \mathbf{M}^{T}\right)^{-1} \mathbf{f0}$$

Due to our assumption of steady state geometry, the storage in each cell equals its discharge, which means that the surface velocity $\texttt{Vel}_i$ for the ith cell is simply:

$$\texttt{Vel}_i = \frac{Q_i}{L \cdot H_i}$$

where L is the surface area of one cell and H_i is the ice thickness for the ith cell. The x and y components V_i and U_i of $\texttt{Vel}_i$ are easily determined through a weighted average of the multiple flow matrix **M** [Schwanghart, W. - Personal communication]. Whereas **I** and $\mathbf{M}^{\mathcal{T}}$ require calculation only once for an entire Monte Carlo routine, Q' and **f0** will be varied for each model in the Monte Carlo routine as described below.

As a final justification of the use of balance velocities, we offer a comparison between the balance velocities obtained by this approach and the InSAR-determined surface velocities by [Bamber et al., 2000] (Fig. 5.5). While the InSAR data contains areas of no information inside our data region, as marked by the black octagon, the balance velocities are free of such discontinuities. Furthermore the largest differences between the InSAR data and the balance velocity data are found in areas consistently characterized in both datasets by low velocity. As the InSAR method is based on feature tracking, surface velocities in such areas are notoriously difficult for an InSAR analysis to quantify and we will thus assume that the balance velocity provides better coverage here as well.

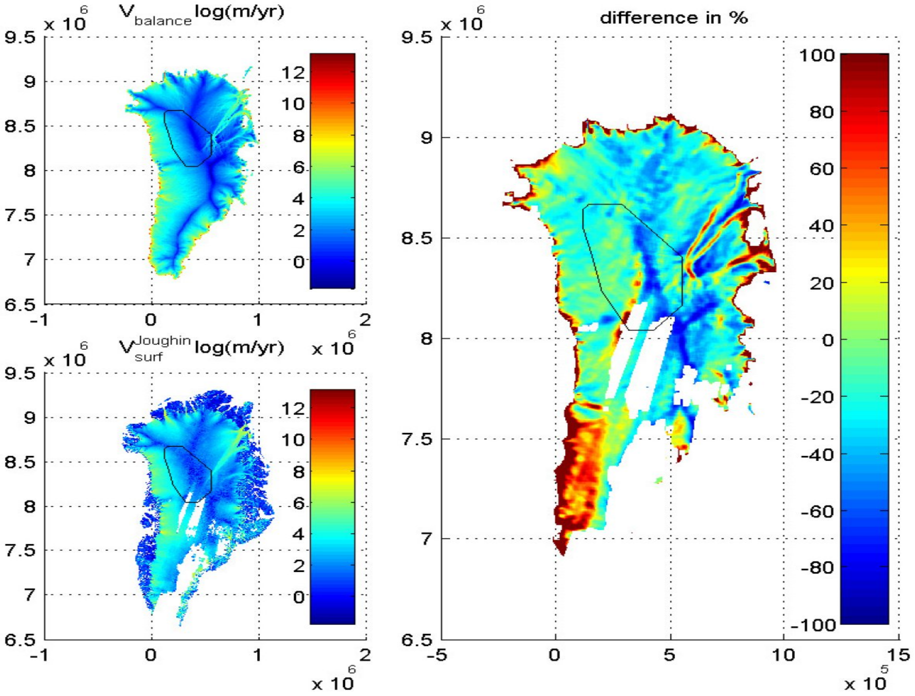

Figure 5.5: Comparison between balance velocity **(top left)** and surface velocities as determined by InSAR **(lower left)**[Joughin et al., 2010]. The difference in percentage is illustrated in the figure on the **right** and the region in which we have data is represented by a black octagon. As the InSAR data contain areas of no information and is notoriously unreliable in low velocity areas we choose to henceforth use balance velocities.

Balance velocity errors and solutions: The balance velocity approach presented here introduces unwanted boundary effects. To avoid their presence within the DR we extend the field in which we calculate the balance velocity to a bigger region. Since we have no information about the accumulation outside the DR (See section 5.3.2) we assign all accumulation values here as the mean of those inside the DR. This has very little effect on the real velocities in the boundary areas and ensures that the unwanted boundary effects remain outside of the DR. The boundary defects are clearly visible in the southern part of Fig. (5.6) which also suggests to us a general flow pattern through the DR. The latter information will be used shortly.

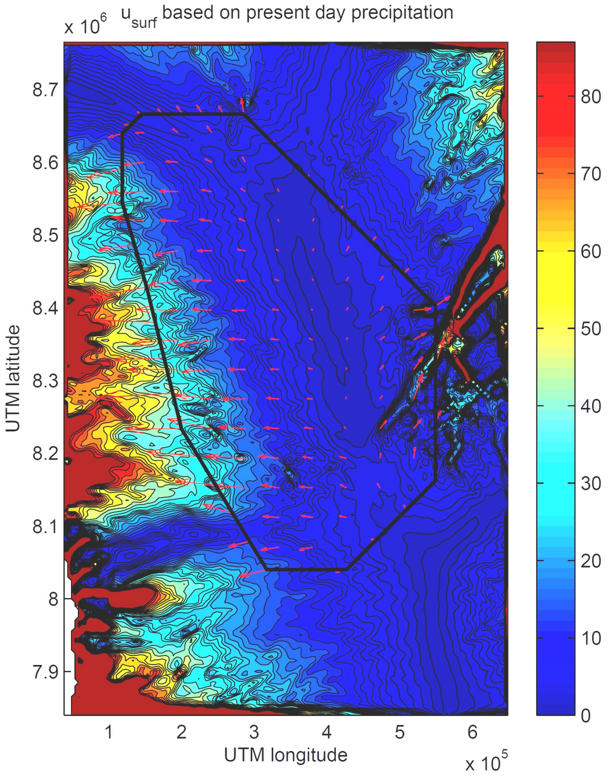

Figure 5.6: Horizontal surface velocity based on the present precipitation pattern, as provided by [Ettema et al., 2009].

5.2.2 Vertical velocity

The vertical velocity w is found through mass balance considerations. We anticipate the vertical velocity to be experiencing some forcing at the boundaries represented by the ice sheet surface S and the bedrock B such that the particles follow either when in their vicinity. We furthermore anticipate such an effect to decrease gradually away from either of the boundaries.

The assumptions made are listed here:

- Mass balance:

$$\frac{\partial w}{\partial z} = -\frac{\partial u_s}{\partial x} = -u_s'$$

  where u_s and $u_s + u_s'\Delta x$ are the horizontal velocities at the left and right side of the box with width Δx, signifying the length a particle moves within one time step, as illustrated in Fig. (5.7)

- No bottom melting

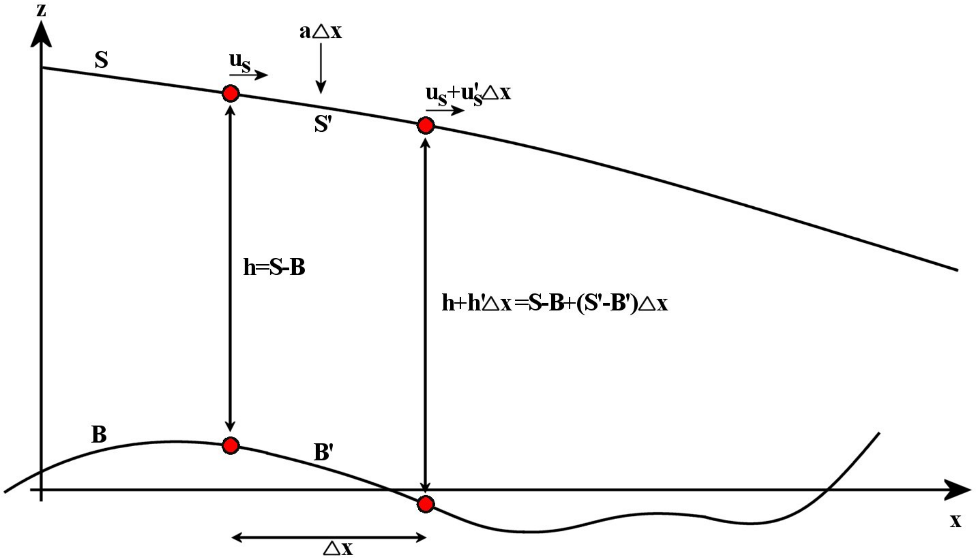

Figure 5.7: Detailed illustration of the terms evaluated during mass balance considerations leading to a formulation of the vertical velocity. Terms include: ice sheet surface S, bedrock B, horizontal velocity u_s and $u_s + u_s'\Delta x$ at left and right boundaries respectively, of the box with timestepping-width Δx. S' and B' are the inclinations of the surface and bedrock respectively, and a is the accumulation. h and $h'\Delta x$ are the ice thicknesses on either side of the box.

- Vertical velocity at boundaries such that either is followed completely:

  $$w(z = S) = u_s S' \quad , \quad w(z = B) = u_s B'$$

  where S' and B' are the inclinations of the surface and bedrock in Fig. (5.7).

- We assume that no melt layers have been present during the period of time for which we use isochrones in this study. Even if such layers were present for a brief period, we are effectively averaging results over 700- to 2000-year intervals between consecutive isochrones, thus making such contributions negligible.

Additional terms in Fig. (5.7) include the accumulation a, the ice thicknesses, h and h', on either side of the box. Thus to maintain mass balance:

$$\begin{aligned} hu_s + a\Delta x &= (u_s'\Delta x + u_s)(h + h'\Delta x) \Leftrightarrow \\ a\Delta x &= u_s'\Delta x h + u_s'\Delta x h'\Delta x + u_s h'\Delta x \Rightarrow \\ u_s' &= \frac{a - u_s h'}{h} = \frac{a - u_s(S' - B')}{S - B} \end{aligned}$$

where the term $u_s'\Delta x h'\Delta x$ vanishes in the limit $\Delta x \to 0$. From mass conservation and the assumption that $w(z = B) = u_s B'$, we get the following relation for the vertical velocity with depth:

$$w(z) = \int_B^z \frac{\partial w}{\partial z} dz + u_s B' = \boxed{-u_s'(z - B) + u_s B'} \tag{5.4}$$

At a particular depth, say 1/2 of the entire depth ($z = \frac{1}{2}(S+B)$), eqn. (5.4) becomes:

$$\begin{aligned} w(z) &= -u_s'\left(\frac{1}{2}(S+B)-B\right)+u_sB' \\ &= -\frac{a-u_s(S'-B')}{S-B}\left(\frac{S-B}{2}\right)+u_sB' \\ &= -\frac{a}{2}+\frac{u_s}{2}(S'+B') \end{aligned}$$

clearly indicating both a vertical velocity caused by the accumulation, $-\frac{a}{2}$, and an equal influence from the surface boundary and the bedrock boundary, $\frac{u_sS'}{2}$ and $\frac{u_sB'}{2}$ respectively. Repeating this evaluation for the boundaries $z = S$ and $z = B$ gives the vertical velocities:

$$\begin{aligned} w(z=S) &= -a+u_sS' \\ w(z=B) &= u_sB' \end{aligned}$$

which emphasizes that the influence of either boundary decreases linearly away from it, and that our requirement that the particle follows the boundaries completely in their vicinity is met. Also note how the accumulation decreases linearly from the surface, meaning that the thinning rate is constant with depth.

5.3 Tracing particles

When we refer to *forward* tracing of particles we are naturally discussing the evolution of ice particles into the ice sheet as consecutively younger layers of snow is added above them. Such tracing can easily result in unpredictable paths when no control is exerted on the starting points of the particles. For our purpose it is preferable to have the end-points of particle paths align in a grid which is fixed even for changing surface velocities and the use of different time periods, corresponding to different isochrones. This will ensure complete coverage of the DR and that the repeated misfit between measured and modeled isochrones (section 6.1.2) is performed at constant locations across the ice sheet. Such behavior cannot be achieved accurately by placing a uniform grid of points across the ice sheet and tracing them forward into it. Suppose our desired uniform grid of end-points is called p_{grid}. Disregarding vertical velocities for a moment and applying negative surface velocities allow us to trace these points backward across the ice sheet to find their points of origin, constituting an irregular grid p_0. As *forward* tracing involves the repeated addition of younger accumulation patterns, and thus also younger surface velocities, *backward* tracing must involve repeated addition of older accumulation patterns and older surface velocities. A 2D illustration of this is found in Fig. (5.8) for the case of isochrones of age 1951 b2k, 2736 b2k and 3962 b2k. Here p_{grid} is marked by red circles and p_0 is marked by blue circles. When forward tracing from the obtained p_0 we reach the near-uniform grid $p_{grid}^{'}$. The distinction between p_{grid} and $p_{grid}^{'}$, which by our logic should be equal, is necessary because of small numerical discrepancies arising as a result of time stepping issues which will be elaborated on shortly.

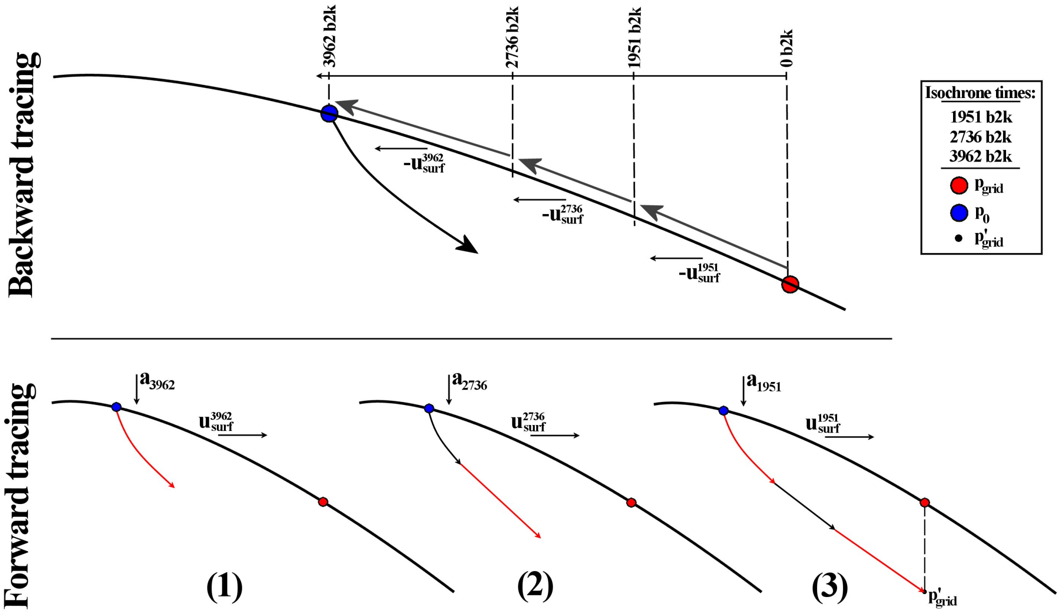

Figure 5.8: Example of backward and forward tracing of particles to determine p_0 and p'_{grid} respectively, from a desired grid of end-points p_{grid}. The example features three isochrones of times 1951 b2k, 2736 b2k and 3962 b2k but only the determination of p_0 and p'_{grid} for $t = 3938$ is illustrated here. Additional path lengths achieved during forward tracing are marked by alternating red and black colors to better illustrate the progression into the ice sheet.

Note how determining p_0 and p'_{grid} for $t = 3962$ b2k requires backward and forward tracing through all three time periods in the example. p_0 and p'_{grid} for $t = 2736$ b2k requires only the two youngest time periods (1951 b2k and 2736 b2k) and so on. Ultimately, for the case of three isochrones, we end up with three sets of p_0 and p'_{grid} values based on one set of p_{grid} values. This is illustrated in Fig. (5.9a) for our actual case of five time periods and 118 points in p_{grid}. The red dots indicate points which originate outside of the DR. This will be discussed shortly.

5.3.1 Timestepping

To relieve the computer in terms of calculation time we will not perform a time step for each year ($dt = 1$) but rather for a series of years ($dt > 1$). We do however require that the model reach the times corresponding to the ages of the isochrones such that it can change accumulation and surface velocities here. This results in a non-uniform series of time steps and we therefore need to be very accurate in ensuring that the paths for the backward and forward tracing are represented by the exact same time steps in reverse. Having made sure of this, any remaining difference between the p_{grid} and p'_{grid} is a matter of tuning dt low enough to move particles back and forth through the pattern of changing surface velocity in consistent paths. The resolution of the surface velocity can be a major factor in creating inconsistencies here. If the resolution of u_s is too high, large time steps will never be able to move along the same paths back and forth while increasingly smaller time steps will have an increasingly better chance. For our particular resolution of u_s we obtain, by setting $dt = 1$, $t_{max} = 7496$ b2k and tracing

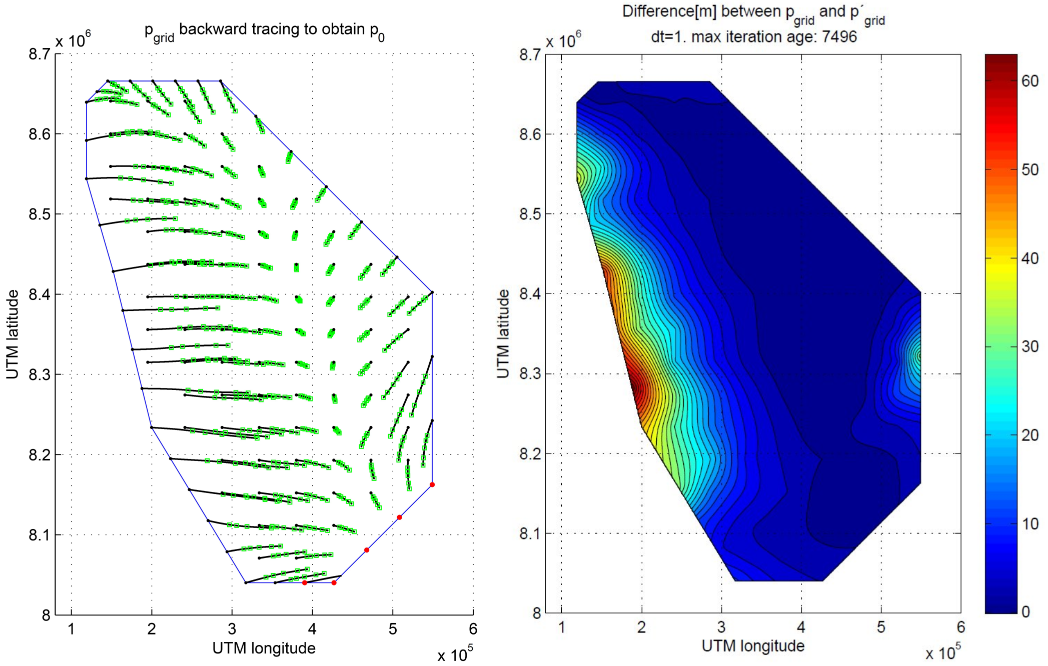

Figure 5.9: **(a)** Example of backward tracing from p_{grid}, marked by **black** and red points, to obtain locations of p_0 marked by green squares. **Black** points indicate p_{grid} which are successfully traced backward without exiting the DR, while red points indicate p_{grid} which left the DR during backward tracing. **(b)** Difference between p_{grid} and p'_{grid} for $dt = 1$.

back and forth, the following ranges of differences between p_{grid} and p'_{grid}, called Δ_{grid}:

$$\begin{aligned}\Delta^{2D}_{grid} &= 0.25m - 2.23m \\ \Delta^{3D}_{grid} &= 0.014m - 62.29m\end{aligned}$$

Comparing these distances with the size of the GIS emphasizes how accurate the presented process is. It should be noted that the much larger maximum errors occurring in the 3D case are caused both by the additional axis of possible error and the fact that the average maximum surface velocity found in the 3D case $(max(u^{3D}_s) \approx 35 - 40m/yr)$ is roughly a factor 8 larger than that found in the 2D case $(max(u^{2D}_s) \approx 4.5m/yr)$. This velocity dependence is intuitively satisfying and furthermore clearly evident when visualizing the errors such as in Fig. (5.9b) and comparing with the horizontal velocity pattern seen previously in Fig. (5.6).

Setting $dt_{2D} = 35$ and $dt_{3D} = 50$, which are much more computer efficient lengths of time steps, will roughly add a factor 35 and 50 respectively to the differences for $dt = 1$. The problem of increased Δ_{grid} is however alleviated by the fact that our data exists on 5km grids, allowing us to assume that our data is smooth within the radius of Δ_{grid} demonstrated in such case. Furthermore the large errors are local (See Fig. 5.9b) and we therefore accept these settings of dt as appropriate compromises between resolvability and computer time for the problem at hand.

In order to ensure complete p_{grid}-coverage within the DR we require points to reach the boundaries. Thus the appropriate setup of p_{grid} involves both boundary points and a uniform grid of points across the interior of DR. This explains the setup of p_{grid} seen previously in Fig. (5.9a)

5.3.2 Tracing errors and solutions

Two types of errors arise when using the tracing approach presented:

- **Escaping particles during forward tracing:** As will be explained shortly, each point in p_{grid} is a parameter to be optimized during the course of the inverse routine. Since we want the velocity field to change as these parameters change, our knowledge on the horizontal velocity field is limited to the DR. Consequently the forward tracing will fail when points exit the DR (we refer to them as *strays*). Since it is impossible to remove the differences Δ_{grid} entirely, without using unfeasibly small time steps we will have to find a general method to deal with the possibility of particles *straying* during the forward tracing. Our approach is to continuously check that particles remain inside the DR. If they escape the DR, the routine informs about the number and their individual index'. It also informs about the time step $(1 \rightarrow 7496)$ and the iteration in the inverse routine $(1 \rightarrow \mathcal{N})$ at which this happened. This allows the user to continuously evaluate whether this behavior should be allowed or if parameters such as dt should be changed. Subsequently further horizontal motion of the particle is refused and its coordinates are forced back one time step to again be inside the DR.

  Strays are mostly associated with the 3D model due to the larger Δ_{grid} here, and are repeatedly seen at the ice flow towards the North east, reflecting very large gradients that are unresolvable by our choice of dt. More importantly, when using our setting of dt_{3D}, all straying occur at the very last time step reflecting only the uncertainty associated with Δ_{grid}. This justifies our approach.

- **Escaping particles during backward tracing:** Just as the routine fails when points stray during forward tracing, the routine will fail when points exit the DR during backward tracing. Judging from the velocity pattern in Fig. (5.6), where knowledge on u_s extends beyond the DR because it is based on the present day precipitation pattern by [Ettema et al., 2009], we anticipate straying during backward tracing to occur only in the southeastern part of the DR. This anticipation was confirmed in Fig. (5.9b)

  An approach to dealing with this problem is to put some thought into the setup of p_{grid} in this region. Merely removing all points in the southeastern part of the DR only moves the problem further into the DR as points there will still experience lack of data for a backward tracing. Thus we allow points in this region but will consider them to be *inactive* in the sense that no new values of accumulation are determined here. Instead present day precipitation values from [Ettema et al., 2009] will be used here and the particles and p_{grid} points in question will be removed from the misfit calculations, described in section (6.1.2), to avoid interference. Furthermore, to deal with the constantly changing horizontal velocity pattern, and the subsequent potential for varying number and index of straying particles, much work has gone into the setup of p_{grid} resulting in a total of 118 points of which 4 points will stray every time during the backward tracing (The red dots in Fig. 5.9a). This is essential as we require consecutive misfit evaluations during the inverse routine to be based on an equal number of points.

5.4 Smoothing of data

Just as the tuning of dt to the resolution of the horizontal velocity field can cause inconsistencies in particle paths back and forth, the resolution of the bedrock, ice sheet surface and isochrones can cause similar effects. This goes for both the 2D and the 3D case, and we therefore list the smoothing approaches used (2D smoothing is illustrated in Fig. (5.10)). The resolution of the 2D and 3D data is $1 \cdot 10^3 m$ and $5 \cdot 10^3 m$ respectively. Consequently a 10-point moving average in the 2D case is equivalent to a smoothing over a 10km stretch, and a $[7 \times 7]$ point mean filter in the 3D data is equivalent to a smoothing over a $[35km \times 35km]$ region.

2D:

- Bedrock is smoothed twice using a 10-point moving average.
- u_{surf} is smoothed twice using a 20-point moving average.
- Isochrones are smoothed once using a 10-point moving average.

3D:

- The digital elevation model (DEM) for the balance velocity routine, consists of the raw ice sheet thickness and the raw bedrock combined and is not smoothed as the GIS, which it represents, is considered smooth.
- The bedrock field itself is smoothed by a $[7 \times 7]$ point mean filter.
- The ice thickness field itself is smoothed by a $[7 \times 7]$ point mean filter.
- u_{surf} is smoothed by a $[5 \times 5]$ point mean filter.
- Isochrones are smoothed by a $[5 \times 5]$ point mean filter.

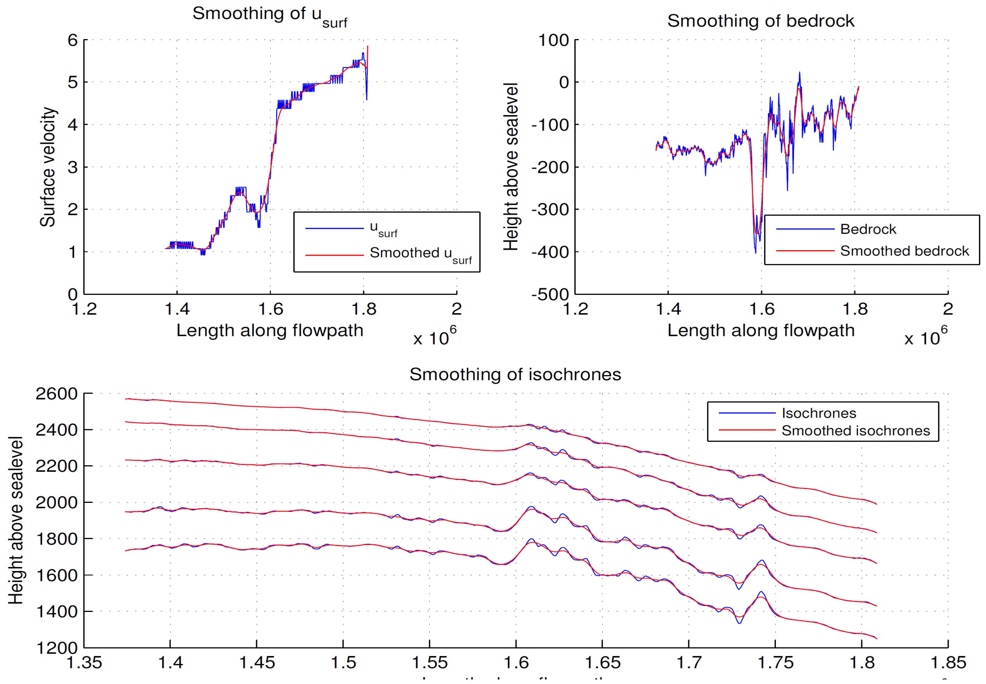

Figure 5.10: Smoothing of u_s, bedrock and isochrones in the 2D case

5.5 Conversion to ice-equivalent data

The presented model does not account for the presence of air in the uppermost layers of the ice sheet called the *firn*. Effectively this means that the model runs entirely with *ice equivalent* (ieq.) values. The depths in the RES datasets are however true in the sense that they do account for air in the firn, meaning that a correction for both the surface of the ice sheet and the analyzed isochrones within, is needed. No air is present at the depth of the youngest isochrones used in this study [Patterson, 1994]. Consequently the correction involves merely subtracting the meters worth of air in the firn from the measured depths of the isochrones z^{iso} and the thickness of the ice sheet S:

$$
\begin{aligned}
z^{iso}_{ieq.} &= z^{iso} - air_{firn} && (5.5)\\
S_{ieq.} &= S - air_{firn} && (5.6)
\end{aligned}
$$

The pattern of air in the firn across Greenland is kindly provided by S.B. Simonsen as part of the study [Simonsen et al., 2010] and is illustrated in Fig. (5.11).

Furthermore, to compare model results with the present day precipitation data, which is obviously given in water equivalent (weq.) values [Ettema et al., 2009], the latter must also be converted into ice equivalent values. This is simply done by multiplying with a factor corresponding to the differences in density of water and ice:

$$
a^{precip}_{ieq.} = a^{precip}_{weq.} \cdot \frac{\rho_{water}}{\rho_{ice}} = a^{precip}_{weq.} \cdot \frac{1000 kg \cdot m^{-3}}{917 kg \cdot m^{-3}}
$$

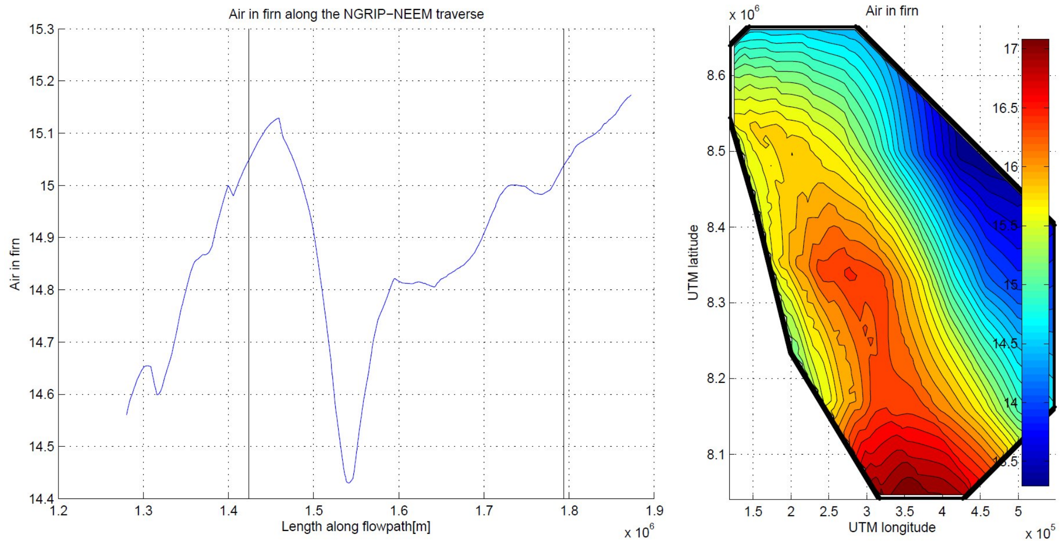

Figure 5.11: Air in firn for the **(a)** 2D case, with vertical lines representing NGRIP and NEEM on the left and right respectively, and the **(b)** 3D case.

6 Inverse problems

A forward problem is characterized as a problem where values for observable quantities are calculated based on values of model parameters. A simple example of such a problem is the calculation of height reached by a bottle-rocket, depending on amount of water used and amount of pressure in the bottle. By contrast, an inverse problem is characterized by one possessing knowledge of observed data, *a priori* (or *prior*) knowledge of values for model parameters, and how these relate to the observed data. For the case of the bottle-rocket this means that we have a large number of height measurements and an equal number of water and pressure measurements. We then also have some *a priori* information about reasonable amounts of water and pressure for the rocket to be propelled at all, and a theoretical model relating water and pressure to height based on our understanding of the underlying physics. Based on this, one anticipates, when solving the inverse problem, to acquire *a posteriori* (or *posterior*) information about the values of the model parameters. This *a posteriori* information could for instance consist of knowledge on the maximum likelihood model, which is a set of model parameters for which the *a posteriori* information is a global maximum. However, solutions to some inverse problem often exhibit bimodal tendencies, meaning that a number of distinct solutions satisfy the minimization requirement, and knowledge about the full *a posteriori* information is therefore preferable. This is also the case for the present study, in which a Monte Carlo approach will be used to gather this information. Specifically a combination of a *simulated annealing* approach and a *Metropolis-Hastings* approach will be used. These will be elaborated on shortly.

6.1 Theory

Much of the initial theory presented here follows [Buchardt, 2009]. Consider a system described by a model with a finite number of model parameters and by data obtained from observations on the system. When ignoring the measuring noise, the relationship between data and model parameters can be expressed as:

$$\mathbf{d}=\mathbf{g}(\mathbf{m}) \tag{6.1}$$

where **d** and **m** are vectors containing the exact data and the model parameters respectively. The latter should not be mistaken with the theoretical model relating data and model parameters. For our case the depth of the isochrones constitute the exact data, and the true accumulation pattern across the finite number of points in p_{grid} constitute the model parameters. All data reside in the *data space*, $\mathcal{D}$, and all model parameters reside in the *model space*, $\mathcal{M}$. It is evident that eqn. (6.1) constitutes a forward problem. In geophysics it is, however, more often the case that data are determined from measurements, and the model parameters are unknown. This inverse problem can be expressed as:

$$\mathbf{m}=\mathbf{g}^{-1}(\mathbf{d})$$

where $\mathbf{g}^{-1}$ is the inverse of the operator **g** in eqn. (6.1). The operators **g** and $\mathbf{g}^{-1}$ are therefore performing what we call a mapping from $\mathcal{M}$ to $\mathcal{D}$ and from $\mathcal{D}$ to $\mathcal{M}$ respectively (See the upper part of Fig. 6.1). The dimensions of $\mathcal{D}$ and $\mathcal{M}$ need not be the same, and generally they are not.

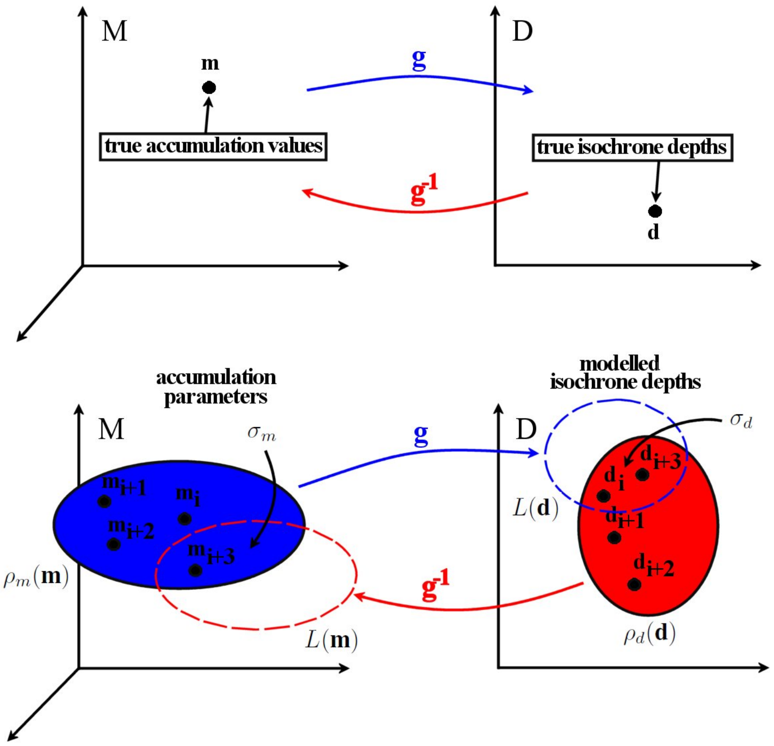

Figure 6.1: **TOP:** The relationship between g and g^{-1} when measurement noise is ignored. **(a)** The model space comprises one model representing a set of true accumulation parameters. **(b)** The data space comprises one set of true measured isochrone depths. **BOTTOM:** The relationship between g and g^{-1} when measurement noise is included. **(a)** The model space comprises individual *models*, each representing a set of accumulation parameters confined to a marginal probability density distribution $\rho_m(\mathbf{m})$. **(b)** Modeled isochrone depths based on each set of accumulation parameters, confined to a marginal probability density distribution $\rho_d(\mathbf{d})$. The operators g and g^{-1} perform a mapping of these into the likelihood functions for models and data respectively; $L(\mathbf{m})$ and $L(\mathbf{d})$. $\rho_m(\mathbf{m}) \cap L(\mathbf{m})$ and $\rho_d(\mathbf{d}) \cap L(\mathbf{d})$ constitute the *a posteriori* probability density functions $\sigma_m(\mathbf{m})$ and $\sigma_d(\mathbf{d})$ respectively.

6.1.1 Probability densities

In eqn. (6.1) measurement noise was ignored. If we include it we have:

$$\mathbf{d}_{obs} = \mathbf{g}(\mathbf{m}) + \mathbf{n}$$

where $\mathbf{d}_{obs}$ and $\mathbf{n}$ are vectors containing the observed data and the noise, respectively. While previously formulating each set of data as a single point in the data space, the uncertainty introduced by the noise forces us to instead consider each point, and consequently also the entire range of data sets as a whole, as an *a priori* probability density distribution, $\rho(\mathbf{d}, \mathbf{m})$. This probability density distribution lies in the system space $\mathcal{S}$ given by the cartesian product of the data and model spaces (Fig. 6.2). The case of no *a priori* information is represented by the null information function μ. Since, by definition, the *a priori* information on $\mathbf{m}$ is independent of the observations, we have:

$$\rho(\mathbf{d},\mathbf{m}) = \rho_d(\mathbf{d})\rho_m(\mathbf{m}) \tag{6.2}$$

$$\mu(\mathbf{d},\mathbf{m}) = \mu_d(\mathbf{d})\mu_m(\mathbf{m}) \tag{6.3}$$

where ρ_d and ρ_m are the marginal, or *individual*, *a priori* probability density functions for data and models (Fig. 6.1). As shown in the figure, the operators g and g^{-1} perform a mapping of $\rho_d(\mathbf{d})$ and $\rho_m(\mathbf{m})$ into the likelihood functions for models $L(\mathbf{m})$ and data $L(\mathbf{d})$, respectively. The overlapping regions $\rho_m(\mathbf{m}) \cap L(\mathbf{m})$ and $\rho_d(\mathbf{d}) \cap L(\mathbf{d})$ constitute the *a posteriori* probability density functions $\sigma_m(\mathbf{m})$ and $\sigma_d(\mathbf{d})$ respectively. Likelihood functions and the *a posteriori* probability density functions are discussed below. The theoretical relationship **g** between the data and the model parameters is not exact but merely a simplification of the real world and should as such also be described by a probability density function $\theta(\mathbf{d},\mathbf{m})$.

The combination of all our knowledge contained in ρ and θ allows us to formulate the *a posteriori* probability density function, $\sigma(\mathbf{d},\mathbf{m})$, and consequently the *a posteriori* marginal probability density functions, $\sigma_d(\mathbf{d})$ and $\sigma_m(\mathbf{m})$, as:

$$\sigma(\mathbf{d},\mathbf{m}) = k\frac{\rho(\mathbf{d},\mathbf{m})\theta(\mathbf{d},\mathbf{m})}{\mu(\mathbf{d},\mathbf{m})} \tag{6.4}$$

$$\sigma_d(\mathbf{d}) = \int_M \sigma(\mathbf{d},\mathbf{m})d\mathbf{m} \tag{6.5}$$

$$\sigma_m(\mathbf{m}) = \int_D \sigma(\mathbf{d},\mathbf{m})d\mathbf{d} \tag{6.6}$$

where $\sigma(\mathbf{d},\mathbf{m})$ is normalized by a constant $k = \int_{D,M} \sigma(\mathbf{d},\mathbf{m})d\mathbf{d}d\mathbf{m}$. Equation (6.5) solves the general forward problem, and eqn. (6.6) solves the general inverse problem. All probability density distributions discussed here are presented in Fig. (6.2)

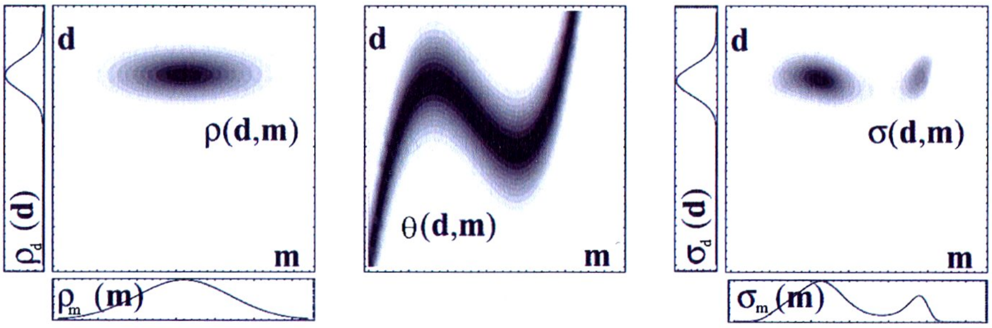

Figure 6.2: Probability distributions as described in the text. **Picture** taken from [Tarantola, 2005].

6.1.2 The likelihood function

For our purpose a solution to eqn. (6.6) is desired. No constraints exist on $\mathbf{m}$ in the theoretical model, and we therefore have:

$$\theta(\mathbf{d},\mathbf{m}) = \theta(\mathbf{d}|\mathbf{m})\mu_m(\mathbf{m}) \tag{6.7}$$

where $\theta(\mathbf{d}|\mathbf{m})$ is the theoretical probability density function for **d** given **m**. Combining eqn. (6.2), eqn. (6.3), eqn. (6.6) and eqn. (6.7) we get:

$$\sigma_m(\mathbf{m}) = \rho_m(\mathbf{m}) \int \frac{\rho_d(\mathbf{d})\theta(\mathbf{d}|\mathbf{m})}{\mu_d(\mathbf{d})} d\mathbf{d} = \rho_m(\mathbf{m}) L(\mathbf{m}) \tag{6.8}$$

where the likelihood function

$$L(\mathbf{m}) = \int \frac{\rho_d(\mathbf{d})\theta(\mathbf{d}|\mathbf{m})}{\mu_d(\mathbf{d})} d\mathbf{d} \tag{6.9}$$

can be interpreted as a measure of the agreement between the observed data and the data calculated from the model parameters [Mosegaard, 1998], as previously illustrated in Fig. (6.1). Analogously the *a posteriori* probability density function for data and the likelihood function for data mentioned previously is:

$$\sigma_d(\mathbf{d}) = \rho_m(\mathbf{m}) \underbrace{\int \frac{\rho_m(\mathbf{m})\theta(\mathbf{d}|\mathbf{m})}{\mu_m(\mathbf{m})} d\mathbf{m}}_{L(\mathbf{d})}$$

We now make the following two assumptions:

- Our experimental results are described as a vector of observed values $\mathbf{d}_{obs}$ with Gaussian experimental uncertainties described by a covariance matrix **C**.
- The theoretical probability density function $\theta(\mathbf{d}, \mathbf{m})$ equals unity when the misfit between true data and modeled data is zero:

  $$\theta(\mathbf{d}, \mathbf{m}) = \delta(\mathbf{g}(\mathbf{m}) - \mathbf{d})$$

  which amounts to saying that a true **m** exists such that $g(\mathbf{m})$ will give the true **d**. Inserting this in eqn. (6.9) where $\mu_d(\mathbf{d})$ is absorbed into $\rho_d(\mathbf{d})$ we have:

  $$L(\mathbf{m}) = \int_d \rho_d(\mathbf{d})\delta(\mathbf{g}(\mathbf{m}) - \mathbf{d}) dd = \rho_d(\mathbf{g}(\mathbf{m}))$$

From these assumptions it can be shown that the likelihood function takes the form:

$$L(\mathbf{m}) = k \exp\left(-S(\mathbf{m})\right) \tag{6.10}$$

where $S(\mathbf{m})$ is a misfit function and k is a normalization constant [Mosegaard and Tarantola, 1995]:

$$S(\mathbf{m}) = \left[-\frac{1}{2}(\mathbf{g}(\mathbf{m}) - \mathbf{d}_{obs})^T \mathbf{C}^{-1} (\mathbf{g}(\mathbf{m}) - \mathbf{d}_{obs}) \right] \tag{6.11}$$

The solution to the inverse problem thus becomes a minimization problem in which the misfit function needs to be minimized.

6.1.3 Determining the covariance matrix C

Having data in a fixed grid with equal distances between all data points would have allowed us to simply formulate a single value for experimental uncertainty in terms of distance from which any error, associated with the isochronous depth analysis, in one data point affect others in its vicinity. Instead we are faced with a highly non-uniform grid of chaotically intersecting lines, each featuring varying density of data points along their path. Therefore we need to introduce individual uncertainties for each model parameter, with respect to every other model parameter. This information is stored in the covariance matrix **C**.

Determining **C** involves a series of steps, in which a large number of surrogate datasets, each featuring raw radar data with noise corresponding to the uncertainty in depth of radar measurements and tracing, is being correlated to produce the **C**-matrix. These steps are described in detail in the appendix (section 13).

6.2 The Metropolis Algorithm

The Metropolis-Hastings (MH) algorithm, as proposed by [Metropolis and Ulam, 1949] [Metropolis et al., 1953] is a Markov Chain Monte Carlo method for obtaining a sequence of random samples from a probability distribution for which direct sampling provides no conclusive result. A Markov Chain refers to a random process with the property that the next state only depends on the current state. I.e.: The process has very little memory. *Monte Carlo* refers to a class of computational algorithms that rely on repeated random sampling for the global optimization problem of applied mathematics and physics. In more general terms, this class is also called *generic probabilistic meta-heuristics*. Meta-heuristics are advancements of *simple heuristics* in which algorithms accept only successively better solutions. Such algorithms requires fewer iterations but run the inherent risk of reaching only local optima in the probability distribution. Thus, the MH algorithm has two major advantages: First, it avoids extensive sampling from low-probability areas, which saves computer time. Second, it is not necessary to evaluate the whole *a posteriori* probability density distribution for the sampled models [Mosegaard and Tarantola, 2002].

A random walk is characterized by the conditional transition probability

$$\mathscr{P}_{ij} = \mathscr{P}(\mathbf{m}_i|\mathbf{m}_j) \tag{6.12}$$

that a random step takes us from $\mathbf{m}_j$ to $\mathbf{m}_i$. At each step the random walker must go somewhere, or stay at the same location, therefore $\mathscr{P}_{ij}$ satisfies $\sum_i \mathscr{P}_{ij} = 1$. Consider a random walk defined by the transition probability distribution $\mathscr{P}_{ij}$, with a distribution $\mathscr{K}_n(\mathbf{m})$ describing the position of the random walker after n steps. Each step of the random walk will modify the distribution $\mathscr{K}_n(\mathbf{m})$ and if $\mathscr{K}_n(\mathbf{m}) \to p(\mathbf{m})$ for $n \to \infty$ we say that $p(\mathbf{m})$ is an equilibrium probability distribution for the random walk [Mosegaard and Sambridge, 2002]. If the random walk for any initial distribution $\mathscr{K}_0(\mathbf{m})$ equilibrates to the same distribution $p(\mathbf{m})$ we say that $p(\mathbf{m})$ is the *unique* equilibrium distribution for $\mathscr{P}_{ij}$. In other words, it is possible for the random walk to reach any point within a sufficient number of steps. This allows us to recast the conditional transition probability eqn. (6.12) into an unconditional form:

$$\mathscr{P}(\mathbf{m}_i, \mathbf{m}_j) = \mathscr{P}(\mathbf{m}_i|\mathbf{m}_j)p(\mathbf{m}_j) \tag{6.13}$$

In the case of the Metropolis-Hastings algorithm the random walk is designed to have a chosen function $p(\mathbf{m})$ as its unique equilibrium distribution. Subsequently two conditions must be met:

1. **Microscopic Reversibility:**
   The probability, at any time, that the random walker enters an infinitesimal neighborhood N_j, surrounding the point $\mathbf{m}_j$, equals the probability that it leaves N_i.

2. **Detailed balance:**
   For any pair of points $\mathbf{m}_j$ and $\mathbf{m}_i$, the probability, at any time, that the random walker jumps from the infinitesimal neighborhood N_j, surrounding $\boldsymbol{m}_j$, to the infinitesimal neighborhood N_i (of the same volume), surrounding $\boldsymbol{m}_i$, equals the probability that it jumps from N_i to N_j.

The latter means that the unconditional transition probability distribution eqn. (6.13) satisfies the following symmetric condition:

$$\mathscr{P}(\mathbf{m}_i|\mathbf{m}_j)\sigma_m(\mathbf{m}_j) = \mathscr{P}(\mathbf{m}_j|\mathbf{m}_i)\sigma_m(\mathbf{m}_i) \tag{6.14}$$

where $p(\mathbf{m})$ has been relieved in favor of $\sigma_m(\mathbf{m})$, thus expressing our intent to construct a random walk with equilibrium probability density σ_m. By eqn. (6.8) we can rewrite eqn. (6.14) as:

$$\mathscr{P}(\mathbf{m}_i|\mathbf{m}_j)\rho_m(\mathbf{m}_j)L(\mathbf{m}_j) = \mathscr{P}(\mathbf{m}_j|\mathbf{m}_i)\rho_m(\mathbf{m}_i)L(\mathbf{m}_i)$$

This requirement is met when $\mathscr{P}(\mathbf{m}_j|\mathbf{m}_i)$ is chosen such that it is proportional to $\rho_m(\mathbf{m}_j)L(\mathbf{m}_j)$ [Mosegaard, 1998]. Assuming that the unmodified random walk has ρ_m as its equilibrium distribution, it can further be shown that the condition of a random walk which equilibrates at σ_m is met when imposing a biased acceptance rule[Mosegaard and Tarantola, 1995]:

$$\mathscr{P}_{ij}^{accept} = \begin{cases} \frac{L(\mathbf{m}_j)}{L(\mathbf{m}_i)} & \text{if } L(\mathbf{m}_j) < L(\mathbf{m}_i) \\ 1 & \text{otherwise} \end{cases} \tag{6.15}$$

for $j > i$. When $L(\mathbf{m}_j) > L(\mathbf{m}_i)$ the random walker will definitely take the suggested step. If the opposite is true the random walker can still take the step based on the ratio between the two likelihoods. If however the algorithm discards the perturbation, the algorithm will step back to the current model and information about this model will be saved again. For our purpose we setup the routine such that the steplength and stepdirection of the perturbations made at each iteration are given by a bounded symmetric uniform distribution centered around zero. The steplength should furthermore be tuned such that an acceptance rate of 30%-50% for each perturbation is obtained after equillibrium has been reached [Tarantola, 2005].

The MH algorithm was originally intended for a specific problem concerning the interaction of confined molecules. In this original problem the probability distribution being sampled was the Gibbs-Boltzmann distribution:

$$P(E) \propto \exp\left(-E/k_B T\right) \tag{6.16}$$

where E is the energy of a certain distribution of molecules, k_B is the Boltzmann constant and T is the thermodynamical temperature. Equation eqn. (6.16) expresses the idea that a system in thermal equilibrium at temperature T[K] has its energy probabilistically distributed among all different energy states E. This is a favorable description for our purpose as even low temperature models will have non-zero probabilities and thus a chance, albeit a small one, of being in a high energy state [Press et al., 2007]. In other words: the routine is permitted to venture along less optimal paths provided that the temperature is sufficiently high.

Sampling the Gibbs-Boltzmann distribution led to the following biased acceptance rule:

$$\mathscr{P}_{ij}^{accept} = \begin{cases} \frac{P(E_j)}{P(E_i)} & \text{if } E_j < E_i \\ 1 & \text{otherwise} \end{cases} \tag{6.17}$$

where by eqn. (6.16)

$$\frac{P(E_j)}{P(E_i)} = \exp\left(\frac{-(E_i - E_j)}{k_B T}\right) \tag{6.18}$$

It can be shown that eqn. (6.15) becomes exactly like eqn. (6.17) when used to sample the Gibbs-Boltzmann distribution[Mosegaard and Tarantola, 1995]. In the process we may compare eqn. (6.17) and eqn. (6.15) and find that the thermodynamic energy E_i is identified as the analog of the misfit function $S(\mathbf{m}_i)$ and $k_B T$ is identified as the equivalent of scaling the misfit function eqn. (6.10) by a factor $t = k_B T$, such that it corresponds to a certain *temperature*:

$$L_{Boltzmann}(\mathbf{m}) = \exp(-S(\mathbf{m})/t) \tag{6.19}$$

where $t = 1$ in the MH agorithm. The whole concept of introducing a term like *temperature* is essential for understanding the simulated annealing routine explained below.

6.3 Simulated Annealing

Simulated annealing (SA) is an adaptation of the MH algorithm, and as such also belong in the category of generic probabilistic meta-heuristics. It is based on the original formulation of the MH algorithm eqn. (6.17) in which the Gibbs-Boltzmann distribution is being sampled, but simulates natures own minimization technique by letting the thermodynamical temperature decrease slowly from high values. SA is inspired by the crystallization of cooling liquids and the annealing of cooling metals. At high temperature the molecules of a liquid or metal move freely with respect to one another. As the material is cooled gradually, thermal mobility is lost and the molecules continuously rearrange such that the system at any given temperature approximates thermodynamical equilibrium, thus ultimately reaching a state of least energy at $T = 0K$. If the temperature is decreased too rapidly, the material will not reach the stage of least energy for a particular temperature but will instead reach metastable polycrystalline or amorphous states with slightly higher energy. The same is true when using SA for minimization purposes, in that the routine might get trapped in local optima if the temperature is decreased too rapidly.

Essentially what happens when increasing the temperature is that the random walk is allowed to escape high probability areas. This means that the random walk will sample a large area without actually sinking into any optimal regions. As the temperature is gradually lowered its ability to pass high probability areas is gradually decreased and the random walk will begin sensing coarse *features* of the probability distribution it is sampling. As the temperature approaches $T = 0K$ the random walk loses its ability to accept less important models completely but has on the other hand by now found a better estimate of the true global optima than possible by the MH algorithm. In fact it has been shown analytically for certain cooling schemes [Nourani and Andresen, 1998] that for infinitely small temperature steps the solution will approach the true global solution. Infinitely small temperature steps are however unfeasible in most applications, and we thus need to formulate a cooling scheme that compromises between computer time and accuracy. Compared to the MH algorithm the SA algorithm is therefore superior when dealing with problems in which the sampled probability distribution is very large and/or problems in which the solution lies among many local optima. While we have no reason to expect many local optima in the present inverse problem, we can never be sure, and the SA routine is therefore a preferable approach. Given the slow cooling in the SA routine it is however important to note that the burn-in period described below will be longer than for the MH algorithm.

For our case, no *temperature* exists. Previously however, we determined the analog relationship between $k_B T$ and a scaling factor t, working on the misfit. For the purpose of SA this essentially means that we should increase t dramatically and let it decrease slowly to its minimum value $t = 1$. The reason behind not letting $t \rightarrow 0$ is that we would then violate the uncertainty limits described by the correlation matrix **C** (See eqns. eqn. (6.11) and eqn. (6.19)). Thus for our specific case the model is still able, but just barely, to accept less favorable steps when SA ends. Following its decrease, t remains constant at $t = 1$ for a longer period, thus effectively separating one entire minimization into a SA part and a MH part, as illustrated in Fig. (6.3). Incidentally only solutions achieved during the MH routine is applicable as the rules of microscopic reversibility is violated in our formulation of SA. As we expect the SA routine to deal primarily with rough solutions we do not expect changes in horizontal velocity to have such a big impact at this stage. Therefore, to further ease computation horizontal velocities used during the SA routine will only be re-calculated at every 20th iteration. As the MH routine takes over, horizontal velocities are again allowed to change as accumulation patterns change.

Cooling scheme The single most important aspect of SA is determining an efficient cooling scheme. Most applications of SA usually involve a stair-stepping cooling scheme in which each step is as long as required to guarantee system thermal equilibrium for its specific temperature [Nourani and Andresen, 1998]. As the primary requirement is that the temperature is decreased slowly we choose to instead stay true to the cooling scheme found in nature; A continuously decreasing profile. Specifically we define a Gaussian curve for the *temperature*, t, as illustrated in the SA part of Fig. (6.3). The upper limit $t(0)$ to the cooling scheme is specific for the 2D and 3D cases respectively. A lower limit $t(\mathcal{N})$ of 1 corresponds to reaching the lowest temperature possible for the system. The width of the distribution is tuned to the specific problem.

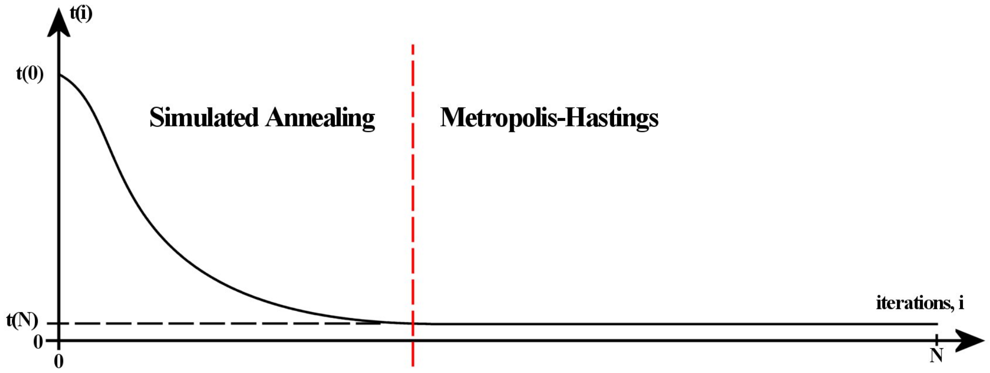

Figure 6.3: Our Monte Carlo routine is effectively separated into an initial SA routine and an MH routine.

6.3.1 Steplength & Stepregion

A step from $\mathbf{m}_i$ to $\mathbf{m}_j$ is made by perturbing $\mathbf{m}_i$ with a gaussianly distributed change in accumulation centered on a randomly selected point in p^{2D}_{grid} and p^{3D}_{grid}. To encourage rapid traveling in the solution space during the SA process the steplength and stepregion, defined as the size of the region in which points are affected by a step, are initially set higher than during the MH process and decrease slowly by way of a Gaussian profile similar to that used to slowly *cool* the inverse problem during SA (Fig. (6.3)). The width of the distribution is identical to that used in the cooling scheme such that the divide between the SA routine and the MH routine remains clearly defined. Illustrations of typical gaussianly distributed steps made in both the 2D and 3D model are illustrated in Fig. (6.4).

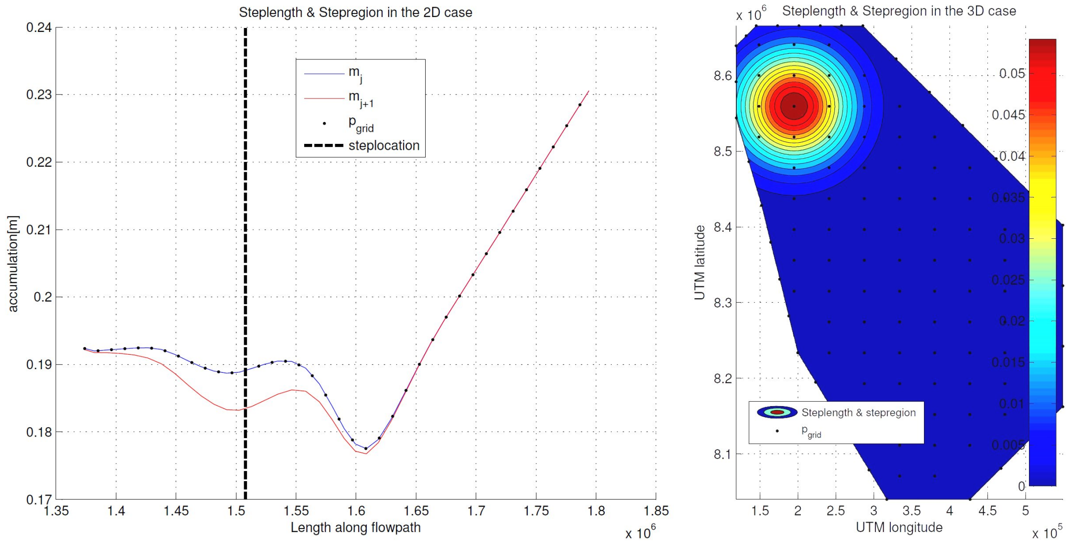

Figure 6.4: Steplength & stepregion for the 2D and the 3D case.

6.3.2 Burn-in and autocorrelation

We expect the Monte Carlo routine as a whole to work its way through a series of unlikely solutions before reaching a region in which solutions are more likely. Furthermore we expect the routine, as temperature is cooled, to eventually remain in this latter region. The initial series of solutions that are unlikely, represent the *burn-in* period whereas solutions drawn from the following equilibrium-like period, are all considered viable.

It is however most likely the case that consecutive solutions are too highly correlated to all actually represent unique models. Ideally we should only use unique models and we therefore perform an autocorrelation on the misfit series obtained after the conclusion of the burn-in. Autocorrelation provides a correlation of the misfit with itself when shifted forward one index at a time. It is widely accepted that when the autocorrelation drops beneath $1/e$ at index i_{ac} the misfit is no longer excessively correlated with itself. Therefore choosing post-burn-in solutions at integers corresponding to i_{ac} should ensure the use of unique and viable models only.

6.4 Curvature constraint

When solving the inverse problem to obtain accumulation patterns we anticipate a certain degree of smoothness of the result. This anticipation is considered to be an *a priori* information and is added to each step of the random walk such that the algorithm not only has to accept/discard a perturbation by eqn. (6.15), but also has to accept/discard a perturbation by:

$$\mathscr{C}_{ij}^{accept} = \begin{cases} \frac{\rho_m(\mathbf{m}_j)}{\rho_m(\mathbf{m}_i)} & \text{if } \rho_m(\mathbf{m}_j) < \rho_m(\mathbf{m}_i) \\ 1 & \text{otherwise} \end{cases} \tag{6.20}$$

where $\rho_m(\mathbf{m}_i)$ is the *a priori* likelihood of the curvature of the model $\mathbf{m}_i$. Contrary to the previous formulation of the misfit eqn. (6.11) associated with the likelihood function eqn. (6.10), the uncertainties in the curvature measurements are described by a Laplacian, and the ratio of the prior likelihoods thus become[Mosegaard and Tarantola, 1995]:

$$\frac{\rho_m(\mathbf{m}_j)}{\rho_m(\mathbf{m}_i)} = \frac{\exp\left(-\frac{1}{2}\left[\frac{c_0 - c(\mathbf{m}_j)}{s}\right]^2\right)}{\exp\left(-\frac{1}{2}\left[\frac{c_0 - c(\mathbf{m}_i)}{s}\right]^2\right)} \tag{6.21}$$

$$= \exp\left(-\eta\frac{(c_0 - c(\mathbf{m}_j))^2 - (c_0 - c(\mathbf{m}_i))^2}{2s^2}\right) \tag{6.22}$$

where c_0 is a reference curvature value understood to be acceptable, s is the variance of the curvature data, and η is an added constant which can be tuned to further encourage or discourage curvature constraint on the solutions. The trade-off occurring for $\eta \neq 1$ is between the resolution and variance of solutions. I.e. the models ability to accurately mimic real physical changes in the accumulation pattern and its ability to over-fit such changes.

The change in curvature associated with a change in model parameters is thus accepted or discarded based on the ratio of current model curvature $c(\mathbf{m}_i)$ and the reference curvature, chosen as $c_0 \equiv c(\mathbf{m}_0)$ where $\mathbf{m}_0$ is our initial model guess. We will use the present day accumulation found between NGRIP and NEEM by [Buchardt, 2009] and a uniform accumulation pattern of 0.2m/yr as $\mathbf{m}_0$ for the 2D and 3D case respectively. The reason for the use of an actual accumulation pattern in the 2D case rather than a fictive and very unlikely pattern such as that used in the 3D case, is simply that our understanding of the inverse problem was improved along the way. Specifically the 3D model appeared to excessively mimic the imposed first guess wherefore a uniform accumulation pattern was deemed preferable. It is reserved for future work to use the same type of fictive pattern in the 2D model for improved comparison. Although the curvature of the uniform accumulation pattern used in the 3D case is obviously zero, the pattern, and thus also curvature, will change as the minimization routine is executed. The following is a description of our quantification of the curvature of both the 2D and 3D accumulation pattern as the routine runs:

The curvature values are determined by first subtracting the mean of each accumulation pattern, as formed by $\mathbf{m}_i$, from itself. Thereafter we apply filters, in which each point in this altered accumulation pattern is averaged over itself and its neighbors. In practice this means applying filters of the type:

$$\texttt{filter}_{2D} = \begin{bmatrix} 1 \\ -2 \\ 1 \end{bmatrix} \quad , \quad \texttt{filter}_{3D} = \begin{bmatrix} 1 & 1 & 1 \\ 1 & -8 & 1 \\ 1 & 1 & 1 \end{bmatrix}$$

where each point is averaged over 3 points and 9 points for the 2D and 3D cases, respectively. The final curvature is then found by summing over all individual curvature values in these curvature patterns, while leaving out the boundaries which due to the filtering has unphysically large values. The unitless curvature values of the initial accumulation patterns thus become:

$$\begin{aligned} c_{2D}(\mathbf{m}_0) &= 1.7263 \cdot 10^{-5} \\ c_{3D}(\mathbf{m}_0) &= 0 \end{aligned}$$

Examples of individual curvature values within the present day accumulation pattern and the present day precipitation pattern[Ettema et al., 2009], which serves as a good example of what our eventual solution for the accumulation pattern could look like, are illustrated in Fig. (6.5).

Since no information concerning the variance s of the curvature data exist, we choose a reasonable value of acceptable curvature and tune the entire expression by η. While we set $s_{2D} = c_{2D}(\mathbf{m}_0)$, setting $s_{3D} = 0$ would naturally cause a breakdown of eqn. (6.22), and we instead set $s_{3D} = 0.0644$ which is the unitless curvature value describing the present precipitation pattern as determined by [Ettema et al., 2009]. The choice of s is not essential as its impact is mostly controlled by the tuning parameter η anyway. The two acts as a combined tuning parameter of the uncertainties describes by the $\mathbf{C}$-matrix.

It should be noted that $c_{2D}(\mathbf{m}_i)$ and $c_{3D}(\mathbf{m}_i)$ are arbitrary values required merely to increase/decrease in accordance with increased/decreased accumulation pattern curvature. Therefore numerous filters and approaches are possible for their determination.

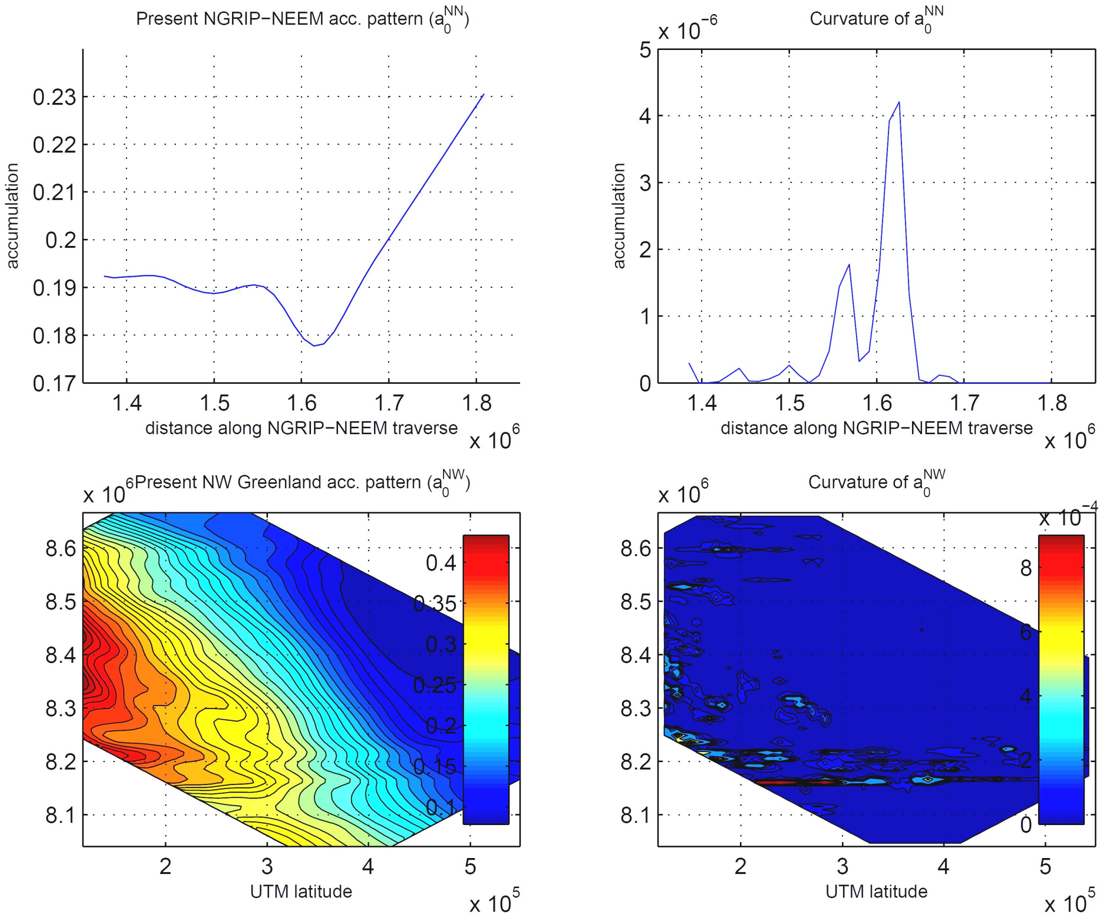

Figure 6.5: **TOP:** Curvature pattern for the present day NGRIP-NEEM 2D accumulation pattern. **BOTTOM:** Curvature pattern for the present day 3D precipitation pattern found in Northwestern Greenland.

7 Setting up the Monte Carlo routine

Based on sessions of trial and error a set of optimal parameters for the Monte Carlo routine has been found for both the 2D and 3D case.

7.1 2D Monte Carlo

Iterations and cooling scheme: For the 2D case we are less restricted by computational time limitations and are therefore allowed to perform long Monte Carlo routines. In this case $\mathcal{N} = 1.6 \cdot 10^5$ iterations will be performed. Out of these, $\mathcal{N}_{SA} = 2.5 \cdot 10^4$ is reserved for the initial SA routine for which the upper bound on the cooling scheme is set to $t_0 = 50$. In terms of slow cooling we feel that N_{SA} is a sufficiently high number to avoid *quenching* of the system. Indeed when the MH algorithm is initiated it merely fine tunes the solution found by the SA routine rather than find a completely new solution, suggesting that the SA routine has worked as intended.

Bounds on accumulation: Upper and lower bounds in possible accumulations are set at $UB = 0.4m/yr$ and $LB = 0.05m/yr$ respectively. Indeed no final solution features accumulation patterns which reach these values and they are thus added to prevent runaway behavior especially during the SA routine where steplengths and stepregions are large.

Steplength and Stepregion: The steplength decreases from $0.01m/yr$ to $3{\cdot}10^{-3}m/yr$ during the SA routine and is hereafter fixed at $3 \cdot 10^{-3}m/yr$ during the MH routine. The stepregion, determined as the width of a Gaussian distribution, decreases from $5 \cdot 10^4 m$ to $3 \cdot 10^4 m$ during the SA routine and is hereafter fixed at $3 \cdot 10^4$ during the MH routine.

Curvature: The zeroth curvature is, as previously mentioned, set at the curvature $c_0^{2D} = 1.7263 \cdot 10^{-5}$ for the present day accumulation pattern. Furthermore $\eta = 5$.

C-matrix: The number of surrogate datasets created in the process of determining the $\mathbf{C}$-matrix is set to $\mathcal{N}_{sur} = 1000$.

7.2 3D Monte Carlo

Iterations and cooling scheme: For the 3D case we are restricted by computational time limitations and are therefore not allowed to perform excessively long Monte Carlo routines. In this case $\mathcal{N} = 5.2 \cdot 10^4$ iterations will be performed. Out of these, $\mathcal{N}_{SA} = 3 \cdot 10^4$ is reserved for the initial SA routine for which the upper bound on the cooling scheme is set to $t_0 = 2.8 \cdot 10^4$. As will be shown both $\mathcal{N}$ and $\mathcal{N}_{SA}$ are not long enough for the model to reach an accurate solution.

Bounds on accumulation: Upper and lower bounds in possible accumulations are set at $UB = 0.65m/yr$ and $LB = 0.04m/yr$ respectively. Once more no final solution features accumulation patterns which reach these values.

Steplength and Stepregion: The steplength decreases from $0.016m/yr$ to $1\cdot 10^{-3}m/yr$ during the SA routine and is hereafter fixed at $1 \cdot 10^{-3}m/yr$ during the MH routine. The stepregion, determined as the width of a Gaussian distribution, decreases from $4.5 \cdot 10^4 m$ to $2 \cdot 10^4 m$ during the SA routine and is hereafter fixed at $2 \cdot 10^4 m$ during the MH routine.

Curvature: The zeroth curvature is, as previously mentioned, set at the curvature $c_0^{3D} = 0$, reflecting our use of a uniform accumulation pattern of $0.2m/yr$. Furthermore the tuning parameter $\eta = 12$.

C-matrix: The number of surrogate datasets created in the process of determining the **C**-matrix is set to $\mathcal{N}_{sur} = 500$.

8 Results and discussion

8.1 2D case

The misfit, as calculated by eqn. (6.11), during the SA-MH routine is illustrated in Fig. (8.1b) along with the curvature, the cooling parameter and the steplength. The burn-in ends at iteration $i = 9 \cdot 10^5$ where both the misfit and curvature has reached an equilibrium around which it oscillates with an acceptance rate of 30.43%. This leaves $7 \cdot 10^5$ possible solutions. To estimate the number of unique solutions autocorrelation is performed on the misfit of the $7 \cdot 10^5$ possible solutions. The autocorrelation becomes smaller than $1/e$ (represented by a green line in Fig. 8.2) at index $i_{ac} = 4369$, meaning that we have $\frac{16 \cdot 10^5 - 9 \cdot 10^5}{4369} \approx 16$ unique solutions. All 16 solutions are fairly similar and to better determine a final solution we allow the use of 500 models chosen uniformly among the $7 \cdot 10^5$ possible models, to create the five accumulation patterns seen in Fig. (8.3a-e). The lines are colorcoded for density of solutions, thus indicating regions of more and less likelihood of being the actual solution. Applying a running median filter to each gives the final solution for past accumulation patterns along the NGRIP-NEEM traverse as seen in Fig. (8.4). A typical histogram for an arbitrary accumulation parameter after burn-in, along the NGRIP-NEEM traverse, is shown in Fig. (8.2a) where the 50th percentile is the median and thus the value we use as a final result. We furthermore use the 5th and 95th percentiles as uncertainties in later illustrations where accumulation results from the 2D and 3D model is being compared along the NGRIP-NEEM traverse.

As a final check that the minimization routine has in fact centered on one solution we offer a plot of two arbirary accumulation parameters, indicating the path taken by the minimization routine (Fig. 8.5). During the SA routine, the minimization checks a very large portion of the solution space, and does in fact zero in on a region of the solution space. The fact that the solutions suggested during the SA routine are so widespread around the actual solution suggests that the routine has entered, and left, the region of interest several times during its initial phases. Again just as intended. As the MH routine takes over, the search remains confined to the region found by the SA routine, indicating once more that the solution presented is indeed trustworthy.

The results presented in Fig. (8.4) suggest a general pattern that has remained fairly stable for the southern section of the NGRIP-NEEM traverse which is situated more inland in the vicinity of NGRIP, and a general, but less stable, pattern for the northern section of the NGRIP-NEEM traverse near NEEM. This is expected as any changes in climate, in terms of changes in temperatures, moisture content and wind circulation patterns around Greenland, is expected to have a greater impact in the coastal and immediate inland regions than in the regions far inland.

The oldest accumulation pattern presented here does however reveal a questionable incline of 0.1m over the last 100km of the northernmost section of the NGRIP-NEEM traverse. [Vinter et al., 2009] showed how site elevation of the northernmost drill site *Camp Century* (CC) changed rapidly around $115 m/kyr$ before the age 6000 b2k, while the trend at NGRIP remained roughly constant at $20 m/kyr$. As NEEM, and the northernmost section of the NGRIP-NEEM traverse in general, is located between NGRIP and CC their changes in elevation might give an indication of the elevation changes around NEEM. Even if CC is a coastal coastal drilling site with much higher sensitivity to climate changes. The elevation of a site requires increased accumulation, but when site elevation is increased dramatically we also expect colder climate and thus less accumulation. This is a negative feedback process and greatly complicates the evaluation of consequences associated with an increased site elevation. If the elevation at NEEM did indeed change rapidly from 6000 b2k and back our assumption of steady state is effectively only satisfied until 6000 b2k and would certainly be a possible clue as to the rapid incline in accumulation seen for the period $5927 - 7496$ b2k for the section of the traverse tending toward CC.

Another possible explanation for the rapid incline in the accumulation in the northernmost section of the NGRIP-NEEM traverse is unwanted boundary effects in the model. Boundary issues has in general been a notorious opponent throughout the duration of this study and while much work has gone into understanding and mitigating such effects (cf. section 5.3.2) we cannot fully disproof the possibility of their presence.

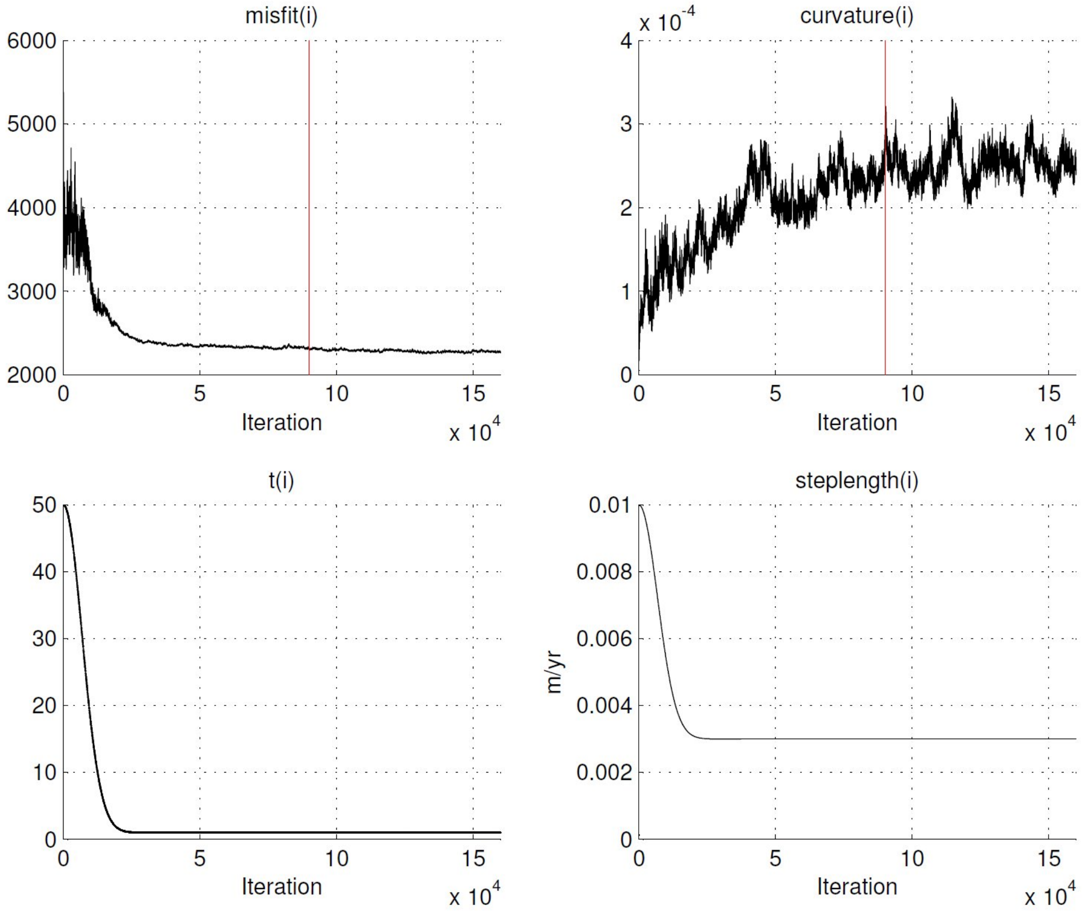

Figure 8.1: Misfit, curvature, cooling scheme and steplength, for the final solution to the 2D problem. The end of burn-in is marked with a vertical red line at $i = 9 \cdot 10^5$

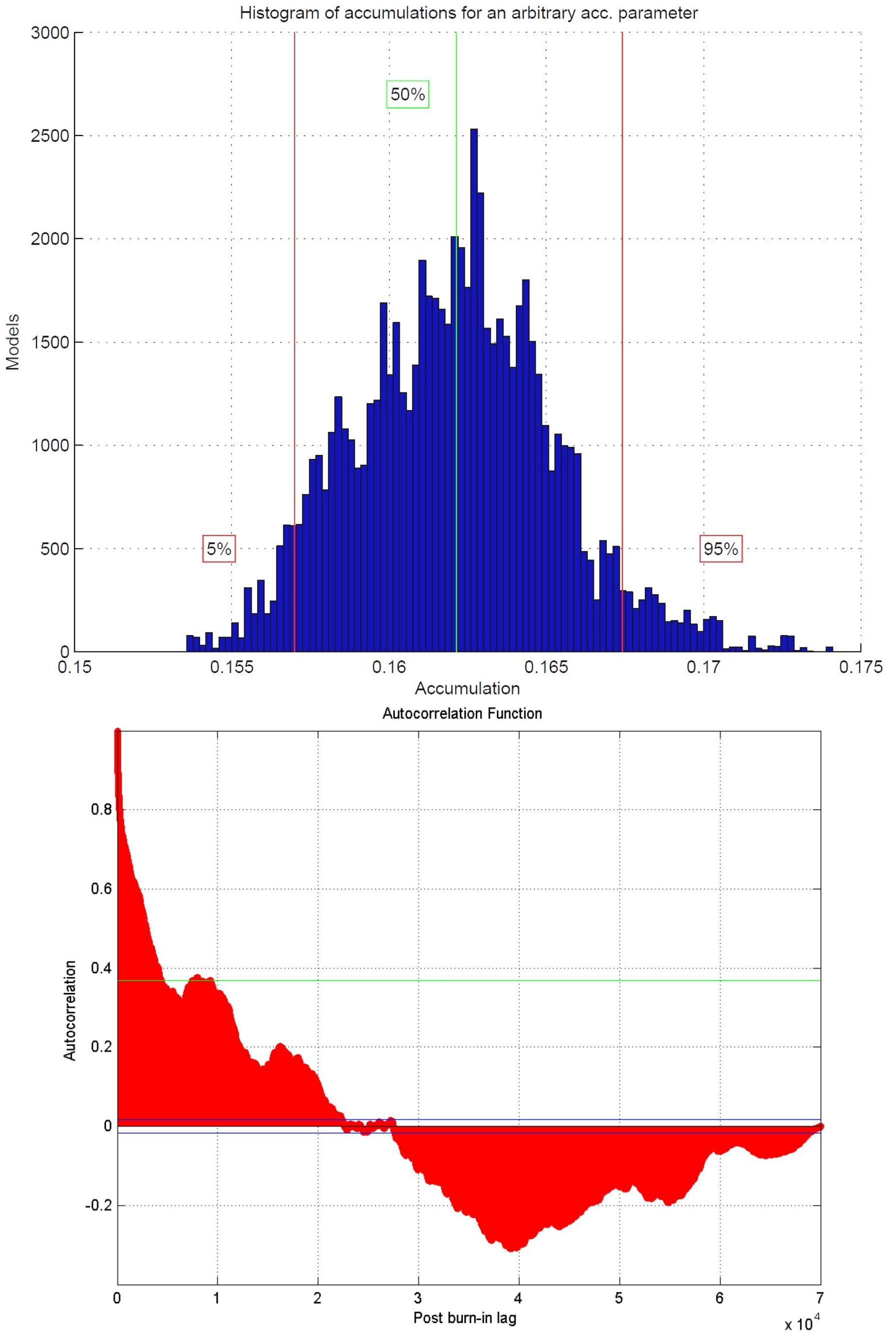

Figure 8.2: **(a)** histogram of an arbitrary accumulation parameter along the NGRIP-NEEM traverse for the 2D model. The 5th and 95th percentiles are used as estimates of uncertainty and the 50th percentile is used as the best solution. **(b)** Autocorrelation of the post burn-in misfit.

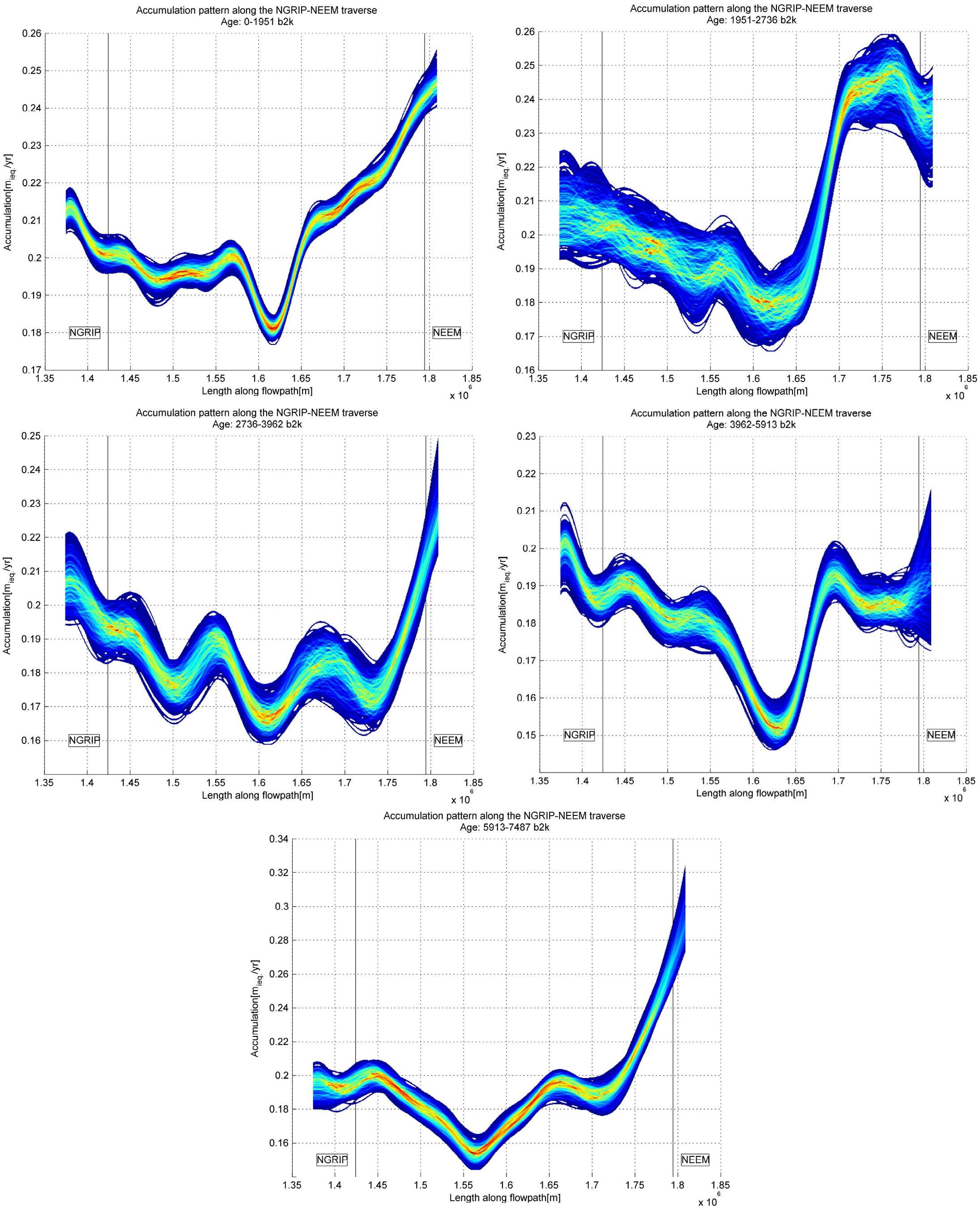

Figure 8.3: **(a)-(e)** 500 accumulation models chosen uniformly from the end of burn-in to the end of the MH routine for all time periods examined. Lines are color coded for density of solutions, suggesting regions with more and less likelihood of being the actual solution.

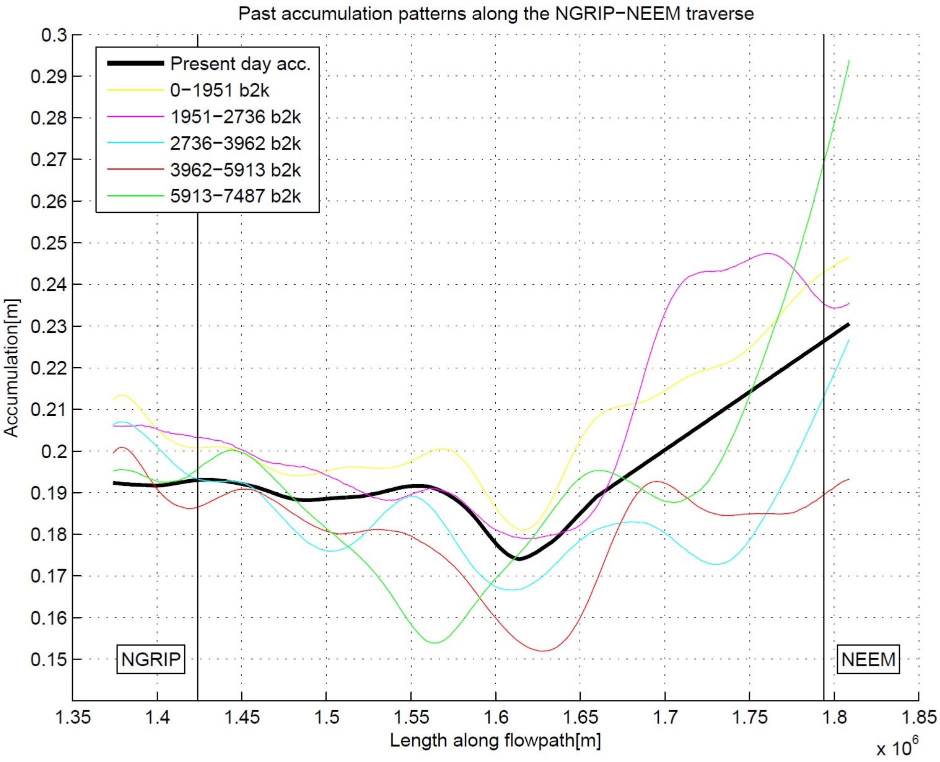

Figure 8.4: Past accumulation patterns along the NGRIP-NEEM ice divide traverse, as determined by 2D modeling

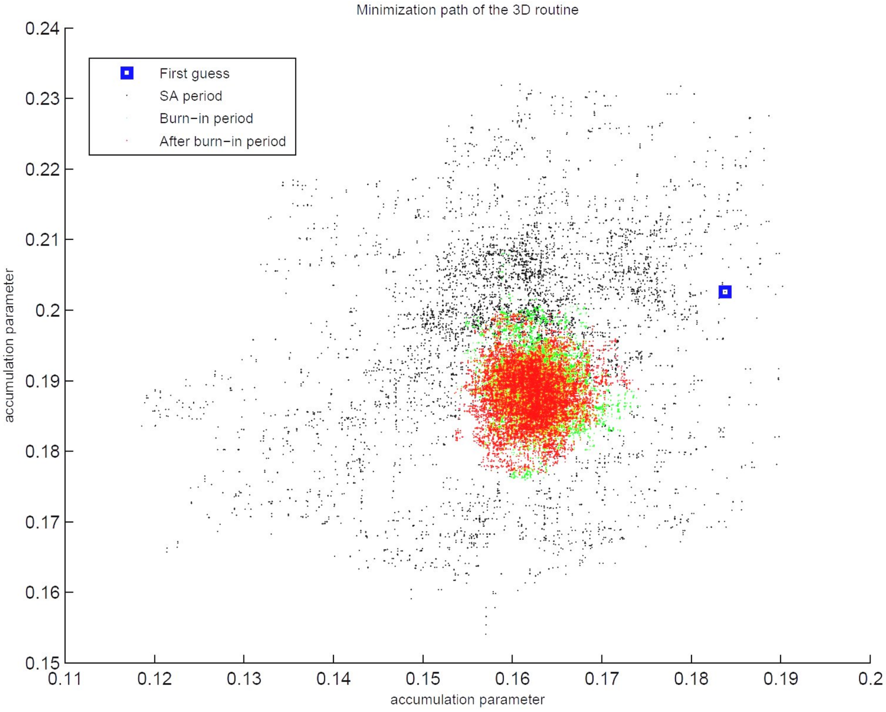

Figure 8.5: Plot of arbitrary accumulation parameters, color coded by their chronology in the Monte Carlo minimization routine. **Black** is solutions found during the SA period ($i = 1 \rightarrow 2.5 \cdot 10^4$), green is solutions found during the remaining iterations in the burn-in period ($i = 2.5 \cdot 10^4 \rightarrow 9 \cdot 10^5$) and red is solutions found after the burn-in period. The **blue** square marks the first accumulation guess.

8.2 3D Case

Contrary to the results shown for the 2D model, we were forced to settle for less optimal results for the 3D case. This happened mainly because many unexpected issues with the model remained unresolved or even undetected until very late in the study. That being said, we feel very confident in the model as it is currently presented in this paper, and furthermore feel that all shortcomings of the results could be resolved easily by tweaking the parameters for the model, if given more time.

The misfit determined during the entire Monte Carlo minimization is illustrated in Fig. (8.6) along with the curvature, the cooling parameter and the steplength. The burn-in ends at iteration $i = 3 \cdot 10^4$ thus leaving us with $2.2 \cdot 10^4$ viable solutions. The acceptance rate after burn-in is 50.35%. It is clear however that the minimization routine has not yet reached equillibrium. Judging from the misfit a progression towards better solutions is still evident, suggesting the need for more iterations. This emphasizes a major drawback of the 3D model and minimization method, presented in this paper; It takes some time running a single evaluation for a single set of minimization parameters (Number of iterations, length of SA routine, upper and lower boundaries/temperature, etc). In fact the results presented here are based on a 20hour Monte Carlo minimization.

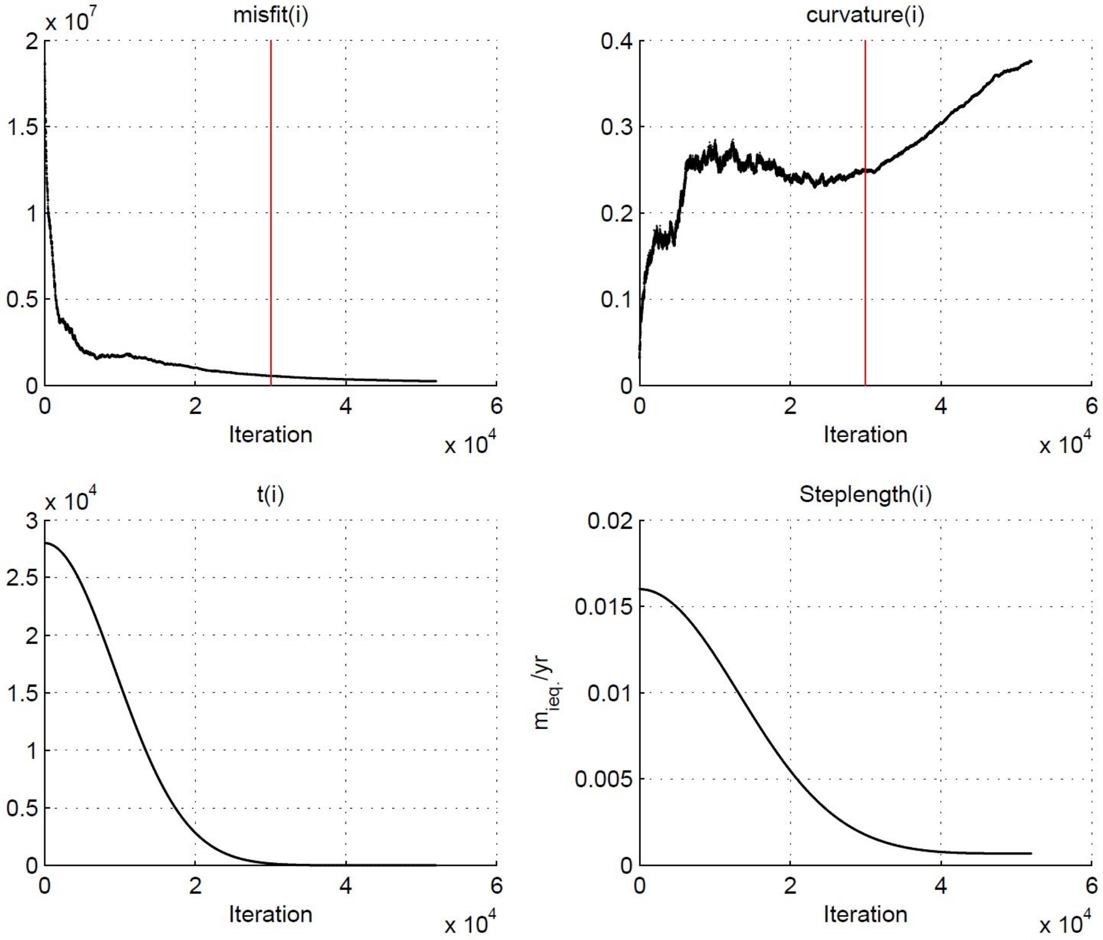

Figure 8.6: Misfit, curvature, cooling scheme and steplength, for the final solution to the 2D problem. The end of burn-in is marked with a vertical red line at $i = 3 \cdot 10^4$

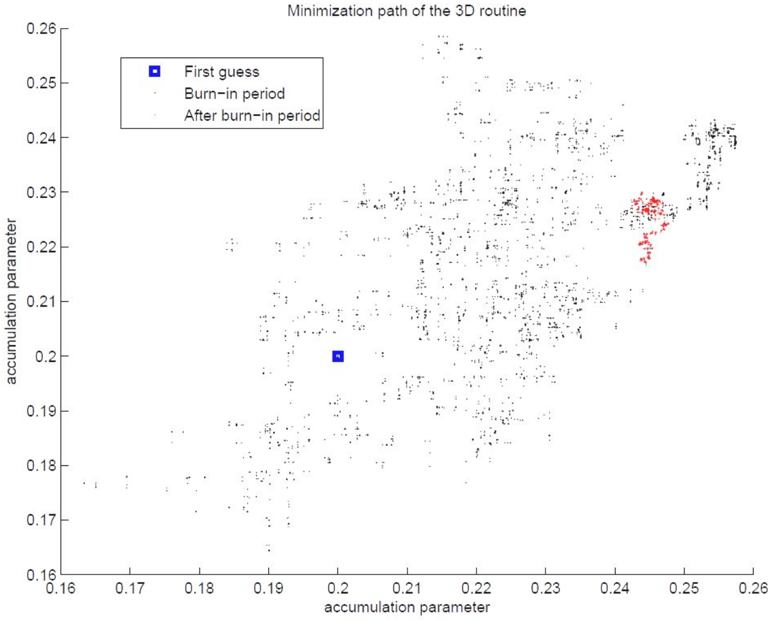

Figure 8.7: Plot of arbitrary accumulation parameters, color coded by their chronology in the Monte Carlo minimization routine. **Black** is solutions found during the SA period, which in this case is also the burn-in period ($i = 1 \rightarrow 3 \cdot 10^4$) and red is solutions found after the burn-in period. The **blue** square marks the first accumulation guess.

Nevertheless the minimization seems to have found the region of interest as movement during the post burn-in period appears limited (Fig. 8.7). These solutions are likely too correlated to all represent unique solutions, and we therefore perform an autocorrelation on the misfit of the entire post burn-in Monte Carlo minimization, resulting in an autocorrelation index of $i_{ac} = 4499$. This means that we have $\frac{5.2 \cdot 10^4 - 3.0 \cdot 10^4}{4499} \approx 5$ unique models after the burn-in. Having a pool of $2.2 \cdot 10^4$ solutions to choose from, with only 5 models that are actually unique is of course not satisfactory, but it serves as a clear indication that the steplength has simply been set too low in this particular run. In such cases the Monte Carlo method requires more iterations to create entirely new models from old ones. As with the 2D results, we choose instead to base the final results on a uniform selection of the post-burn-in models such that we end up with a selection of 500 individual models.

In order to accurately illustrate 3D results, we need a slightly different approach than that used in the 2D case. We still form series of 500 points for each of the 118 accumulation parameters in p_{grid} and calculate their 5th, 50th and 95th percentiles. A histogram and associated percentiles of an arbitrary accumulation parameter for all models past the burn-in is illustrated in Fig. (8.8). The very narrow spread of solutions, in terms of accumulation value, indicate that the minimization has reached the region of interest. The gaps seen in the distribution are however an indication that too few models are evaluated after the burn-in but can easily be corrected if running longer Monte Carlo minimizations. While the 50th percentile appears reasonable for this particular parameter, the many gaps in the solution distributions for other parameters cause increased uncertainty of the 50th percentile. if we disregard this fact and leave the improvement of this issue to future work, the 50th percentile can again be considered the best guess for a final accumulation pattern solution. The 5th and 95th percentiles are considered to be uncertainties associated with each such final accumulation pattern solution. Instead of illustrating color coded solution densities we now trust the information described by the calculated percentiles and merely plot those. An illustration of one accumulation pattern aged $0 - 1981$ b2k and corresponding uncertainties is found in the upper part of Fig. (8.9). The uncertainties seen here are small and since this is the case for all other accumulation patterns as well, the remaining four patterns are illustrated without their uncertainties in the lower two rows of the same figure. While the youngest 4 ages feature a generally consistent gradient in accumulation, the oldest, aged at $5927 - 7496$ b2k seem to have changed, particularly in the northernmost region. This we once again attribute to changes in the ice sheet elevation as described previously in section 8.1.

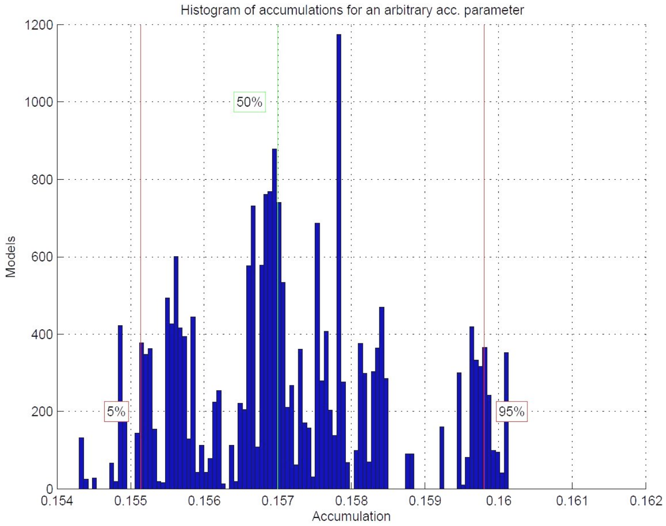

Figure 8.8: Histogram of all post-burn-in models of an arbitrary accumulation parameter along the NGRIP-NEEM traverse for the 3D model. The 5th and 95th percentiles are used as estimates of uncertainty and the 50th percentile is used as the best solution. Contrary to the 2D case, the histogram is based on models from a Monte Carlo minimization that have yet to find its equillibrium. Consequently the percentiles are more uncertain and the histogram is more spread out, often with no distinct peak.

The accumulation patterns and uncertainties shown in Fig. (8.9) results in the NGRIP-NEEM traverse accumulation patterns seen in Fig. (8.10). Results found using the 2D model are shown in red and results found in the 3D model are shown in green. Both are shown along with their uncertainties. As expected the solutions for the age $0 - 1981$ b2k are very similar. This is of course the case because traced ice particles move shorter distances in the horizontal directions for shallow isochronous surfaces. Secondly the characteristic trough found in the present accumulation pattern at $1.6 \cdot 10^6 m$ along the flow line, is evident to varying extent in both the 2D and 3D results, emphasizing that it reflects actual physics rather than undesired numerical effects. The trough appears to be shifted slightly toward the south (left) in the 3D results compared to the 2D results in some of the accumulation patterns shown. This may be caused by two interconnected sources: The main ice-ridge bifurcates into a NW tending and a NE tending ice-ridge in the area where the dip is generally found. This creates a very complicated flow in this region. To further complicate things the NGRIP-NEEM traverse data is, contrary to most of the CReSIS data analyzed, based on ground based RES and has reportedly deviated up to a few kilometers from the actual ridge. Since we never make assumptions as to the location of the ice-ridge in the 3D model, this suggests that the dip is found elsewhere in the 3D model and that evaluating it over the same potentially flawed ice ridge coordinates used in the 2D model is responsible for the slight shift observed.

All accumulation patterns along the NGRIP-NEEM traverse found by 3D modeling are illustrated in Fig. (8.11). Whereas the 2D model showed the stability of the inland accumulation pattern compared to the coastal accumulation pattern, the 3D model appears to show great variability in both regions with high stability between the two regions. The increased variability in the inland regions contradict our understanding of the climate system but can again most likely be attributed to an incorrect definition of the ice-ridge coordinates. As mentioned before the 3D model makes no assumptions about the ice-ridge, but when we interpolate data from our 3D model to the ice-ridge coordinates that we have determined from measurements which can be up to several kilometers off from the actual ridge, we are essentially not comparing ice-ridge flows from the two models. To support this idea we present an illustration of the surface balance velocities along the NGRIP-NEEM traverse (Fig. 8.12). The velocities are irrelevant here but the directions are not. If the coordinates for the ice-ridge were correct, all arrows would be following the traverse. This is clearly not the case for the inland region in the vicinity of the major ice flow in North-East Greenland. A clear indication that the coordinates for the ice divide should be moved further to the west for this particular section of the NGRIP-NEEM traverse, if comparison between accumulation patterns should be optimal. Judging from the accumulation patterns in Fig. (8.9) performing such a change will generally increase the accumulations found along the ridge in the southernmost part of the NGRIP-NEEM traverse. An accurate estimate of the coordinates for the ice ridge is needed to resolve this discrepancy. It will be a subject for future work to determine one such estimate.

Having discussed the inherent source of potential difference in accumulation patterns between the 2D and 3D models, caused by the likely different understanding of term *ice ridge* in either model, we can still make some simple observations based on the accumulation differences observed between the 2D and 3D model in Fig. (8.10). Essentially, if the 2D model assumes no transverse flow, and the 3D model makes no assumptions on this matter, a comparison of accumulation patterns along the NGRIP-NEEM traverse (even if deviating slightly from the actual ridge) should indicate the properties of the transverse flow which the 2D model will not pick up on. When less accumulation is found by the 3D model compared to that found in the 2D model, such as in Fig. (8.10a), it suggests that the transverse flow has been responsible for a positive inflow of ice, or '*thickening*' of the region in the 3D model, thus diminishing the need for accumulation to create the observed isochrones. By that logic, if the opposite is true such as for the remaining four isochrones, the transverse flow has been responsible for a greater outflow of ice, or '*thinning*' of the region, thus increasing the need for accumulation to create the observed isochrones. It makes sense that the less shallower layers indicate a thinning because the 3D flow field of the ice sheet will progressively move particles away from the center of the ice sheet, thus thinning it. Although small differences between the 2D and 3D accumulations are likely within the limit of uncertainty associated with the fact that the Monte Carlo has yet to reach an equillibrium, there is a clear indication that transverse flow has an effect along the ice ridge.

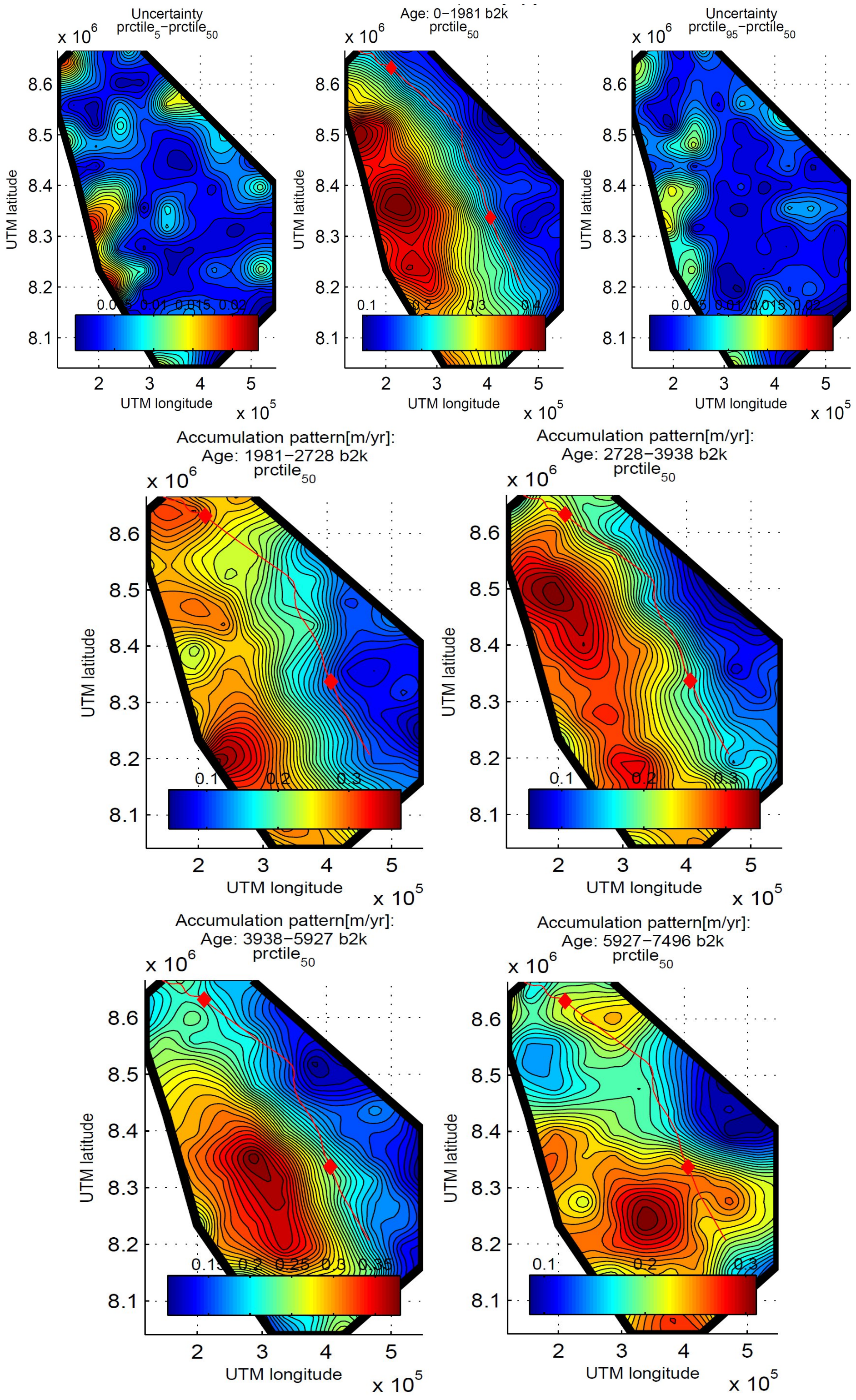

Figure 8.9: **TOP:** Accumulation pattern solution for the age 0 – 1981 b2k. **(a)** Difference between the 5th and the 50th percentile (lower bound uncertainty on the solution). **(b)** 50th percentile (actual solution). **(c)** Difference between the 50th and the 95th percentile (upper bound uncertainty on the solution). **MIDDLE & BELOW:** Accumulation pattern solutions (50th percentiles) alone for the ages 1981 – 2728 b2k, 2728 – 3938 b2k, 3938 – 5927 b2k and 5927 – 7496 b2k.

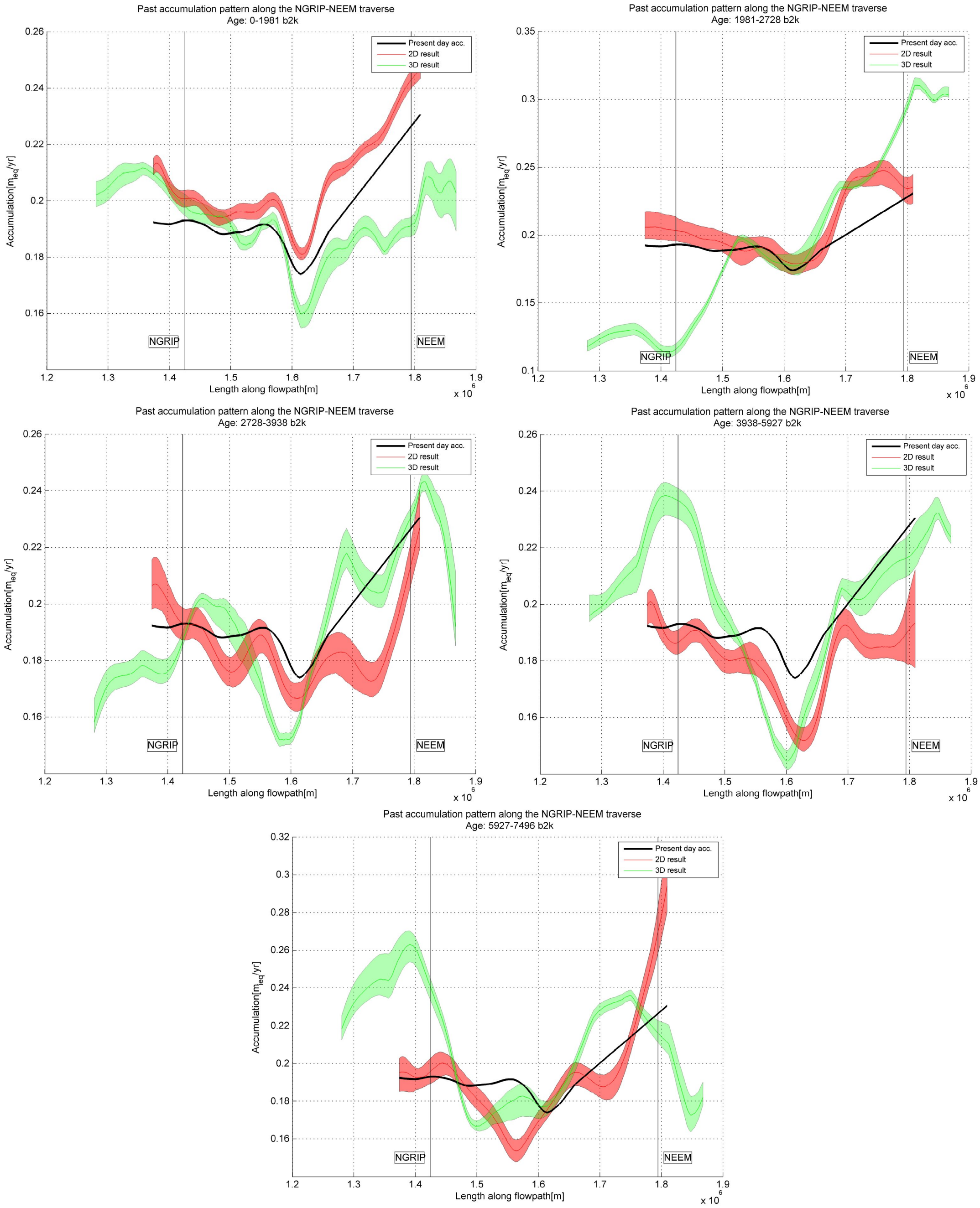

Figure 8.10: Comparison of NGRIP-NEEM traverse accumulation patterns determined from the 2D model shown in red and the 3D model shown in green. Both are shown along with their uncertainties. NGRIP and NEEM has been marked along with the present day accumulation pattern as determined by [Buchardt, 2009].

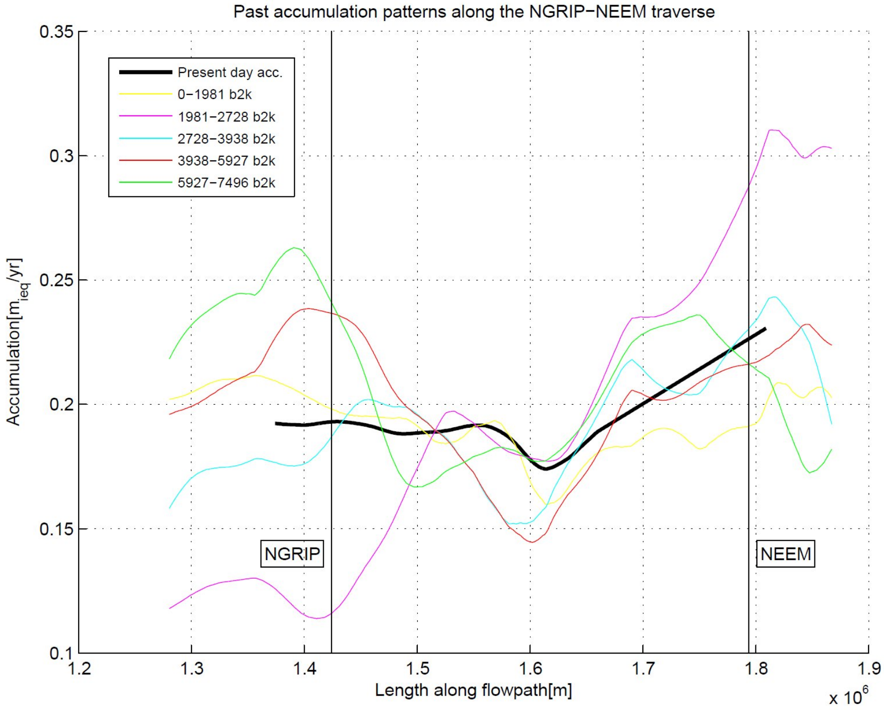

Figure 8.11: Final solutions of accumulation patterns along the NGRIP-NEEM traverse, determined by the 3D model. NGRIP and NEEM has been marked along with the present day accumulation pattern as determined by [Buchardt, 2009].

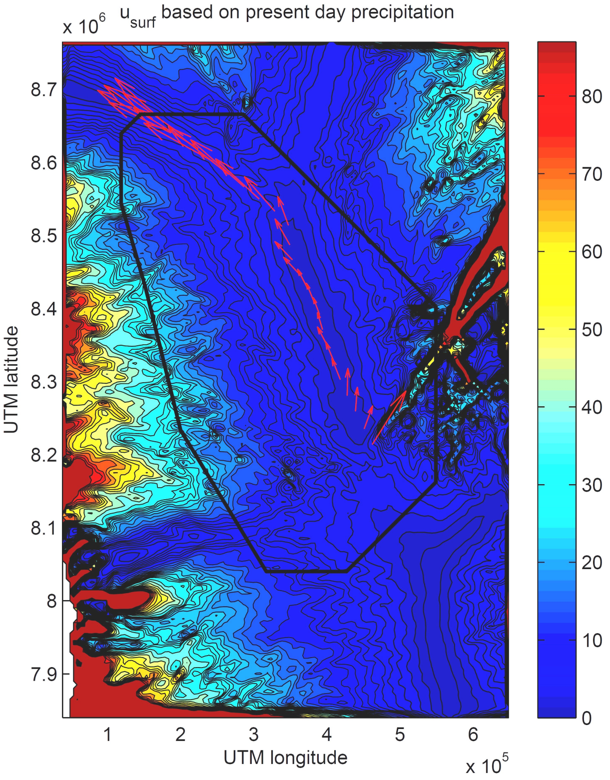

Figure 8.12: Balance velocities and directions along the NGRIP-NEEM traverse.

8.3 Pre-industrial times

From a global warming perspective the change in accumulation from pre-industrial times to present day is of particular interest. We use the present day precipitation pattern (Fig. 8.13a) determined by [Ettema et al., 2009] and the accumulation pattern determined for the period $0 - 1981$ b2k. Subtracting these such that the result indicates accumulation change going from pre-industrial times to present day we get the accumulation-change pattern seen in Fig. (8.13b). I.e.: It snows on average $0.02m/yr$ more in the Northernmost part of the DR and generally $0.08 - 0.14m/yr$ less in the innermost part of the DR today, than it did 1981 years ago. Evaluating the validity and causes of such change requires a more in depth discussion of the weather patterns in Northern Greenland and is outside the scope of this study.

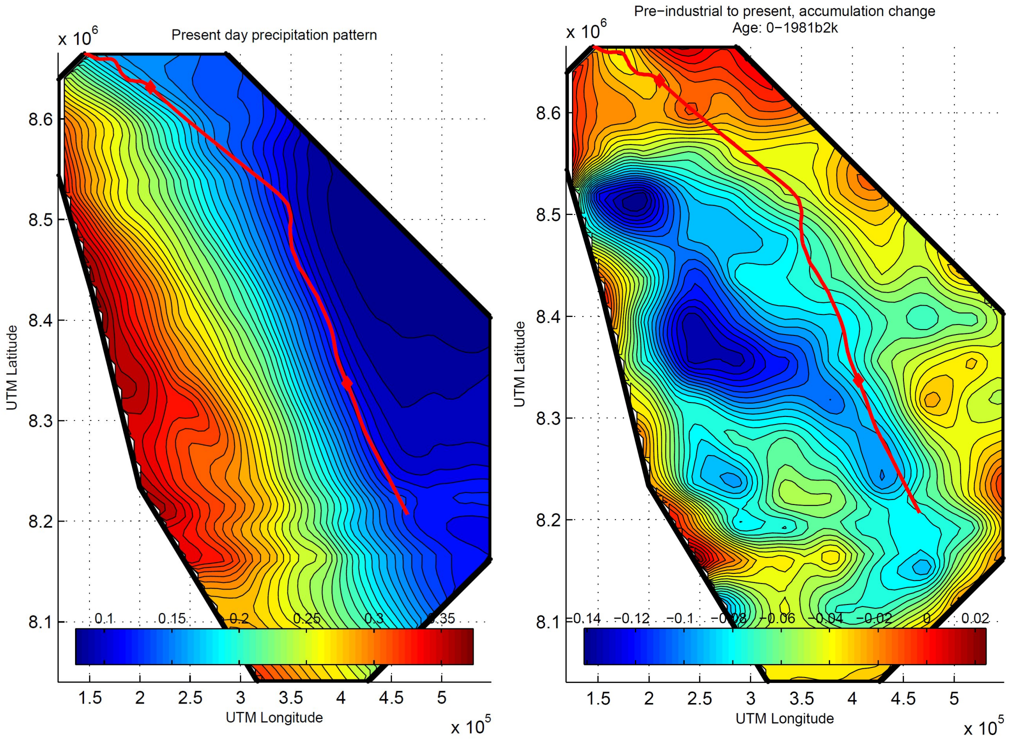

Figure 8.13: **(a)** Present precipitation pattern [Ettema et al., 2009]. **(b)** Change in accumulation when going from 1981 b2k to present day.

9 Conclusion & outlook

It was the ambition of this study to progress from inferring accumulation patterns from isochrones found within single aerial RES flight lines, to inferring accumulation patterns across a 3D surface, from isochronous surfaces across great expanses of the GIS.

A large part of the effort presented in this study was associated with the analysis of isochronous features within the massive CReSIS RES data archive for the GIS. We developed a Matlab routine which greatly improved the otherwise tedious and slow process of analyzing IRHs within RES data. Over a period of many months isochrones for 25 fixed ages were analyzed for a total of 55 individual flight segments within said data archive. These data were then consolidated to form 25 isochronous surfaces covering a large region in North-Western Greenland including the ice-ridge between ice core drilling sites NGRIP and NEEM.

Very early on it was recognized that regardless of the outcome of the subsequent attempts to infer accumulation patterns, the isochrone dataset itself would serve as an important result. The fact that much effort went into analyzing a full 25 isochronous layers, when only around half could ever be put to use in the present study serves as a recognition of the potential of such dataset. It is hoped that the dataset will find its way to a large number of interesting applications in the future.

The traditional approach to inferring climatic data from isochrones is using RES data from single aerial or ground based along-track operations and making assumptions about the transverse flow. To compare such an approach with a 3D approach, data from a ground based RES operation along the ice-ridge between NGRIP and NEEM was included. 2D and 3D models describing the flow of ice particles within the GIS over time, were setup. Requirements to the models included a certain theoretical simplicity as well as large similarity, and led us to discuss horizontal balance velocities, vertical velocities, tracing of particles and time stepping. Much work went into setting up these models and despite of their inherent simplicity we feel that for the region in which we have data, they really do, to a great extent, reflect the actual flow pattern being observed on the GIS.

As a final step a combined Simulated Annealing and Metropolis-Hastings inverse method, featuring an *a priori* curvature constraint, was presented. The inverse routine for the 2D problem succeeded in finding a likely accumulation pattern. For the 3D problem however, the combination of the computationally demanding nature of the 3D model and the fact that many unexpected issues with the model remained unresolved or even undetected until very late in the study resulted in limited time spent tweaking the parameters for the inverse routine and consequently less optimal solutions. As previously stated the solutions are acceptable but could be improved if more time was given to improve on said parameters and perhaps if access to faster computers could be arranged.

Nevertheless the comparison of the 2D and 3D results revealed several interesting aspects of the accumulation pattern, among which its sensitivity to climate changes in coastal regions versus inland regions. based on the comparison the presence of a transverse flow was also discussed. The conclusions were however all pointed out to be affected by the fact that the inverse routine never reached equilibrium for the 3D case, and the clear indication that our coordinates for the NGRIP-NEEM traverse deviates from the actual ice-ridge.

In conclusion we are satisfied with the amount of output data created during this study and feel that we have succeeded in accurately interpreting these data in the context of accumulation patterns, even if much work is still suggested for further development of the tools to solve this problem.

10 Future work

During this study many ideas and ambitions for further development of the tools for solving the presented problem was discussed and discarded on the basis of the limited time. Some of the more notable suggestions are presented here:

- It was part of the initial ambition to analyze as many interconnected RES datasets and infer accumulation rates across as vast a region of the GIS, as possible. Within the time frame of this study we are very satisfied with the data output. It remains however of course among future tasks to analyze data for an even bigger region. For the model presented here analyzing data for the highest point on Greenland would as an added bonus most likely resolve the issues of points exiting the DR during backward tracing, thus resulting in an entirely *active* p_{grid}.

- From the very beginning it was decided to analyze RES data older than 9700 b2k although our condition of steady state clearly stated that such data could not be used. This was done as a recognition of the labor intensiveness of RES data analysis and an understanding that we had made such analysis much more efficient and fast with our analysis routine. It was basically a recognition of the need for this type of data and a choice made such that it allowed for further studies in this area, using models capable of dealing with older isochrones.

- We chose to re-date the data used for the 3D model based on isochrone depths at NGRIP. This happened in the 11th hour of the study and prevented us from making a new 2D dataset based on our 3D data, to essentially end up with data of same age. Instead we accepted the relatively insignificant differences in age of isochrones. It is of course suggested that this be corrected for future projects.

- For the 2D inverse problem we chose an actual accumulation pattern as our first guess, whereas a uniform, and thus unlikely, accumulation pattern was chosen as first guess for the 3D model. This change in first guess were carried out since the 3D model had a tendency to excessively mimic the first guess, unless patterns with no features where applied. We did not have time to conduct an investigation into the possibility of such effects in the 2D model and it is therefore left as a future assignment.

- The flow model presented here was very simple and based on some quite basic assumptions. For future work it would be interesting to further develop this model to better describe complex ice flow patterns and to include terms like ablation and bottom melting.

- Apart from advancing the model used, it would also be interesting to apply such a model to a faster computer allowing for smaller time steps and for much longer Monte Carlo routines, ultimately providing much more accurate results. In general longer Monte Carlo routines need to be applied for the 3D model such that the minimization finds an equilibrium and we can provide even more detailed and trustworthy data. This would also serve to improve our estimate of the histogram percentiles in the solutions.

11 The First Appendix

The following is a chronological description of the analysis, using the matlab routine described in section 4.1.2:.

1. **Choice of flightline:**
   In order to select a flight line for subsequent analysis of isochronous layers, the user is asked to either select a previously analyzed RES dataset from a list (Fig. 11.1a), or prompt a graphical display of all flight lines across Greenland by pressing cancel (Fig. 11.1b). Blue lines signify lines that have yet to be analyzed, and red lines signify lines that have been analyzed, even if only for some of the 25 isochrones. If choosing a line that has already been analyzed, the user is confronted by the option to continue working on an old analysis or clear the data recorded for this RES dataset and start all over. As the whole analysis starts from the NGRIP-NEEM traverse which has already been analyzed, a red line from which to build a grid of analyzed flightlines, will appear between NGRIP and NEEM.

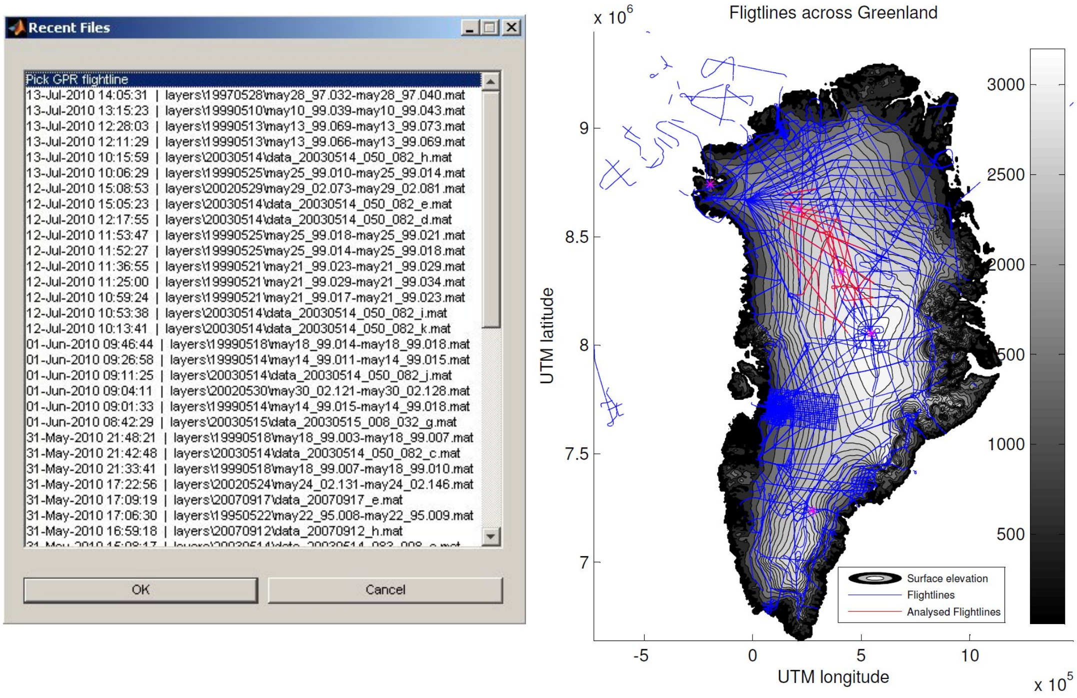

```
Pick GPR flightline
13-Jul-2010 14:05:31  |  layers\19970528\may28_97.032-may28_97.040.mat
13-Jul-2010 13:15:23  |  layers\19990510\may10_99.039-may10_99.043.mat
13-Jul-2010 12:28:03  |  layers\19990513\may13_99.069-may13_99.073.mat
13-Jul-2010 12:11:29  |  layers\19990513\may13_99.066-may13_99.069.mat
13-Jul-2010 10:15:59  |  layers\20030514\data_20030514_050_082_h.mat
13-Jul-2010 10:06:29  |  layers\19990525\may25_99.010-may25_99.014.mat
12-Jul-2010 15:08:53  |  layers\20020529\may29_02.073-may29_02.081.mat
12-Jul-2010 15:05:23  |  layers\20030514\data_20030514_050_082_e.mat
12-Jul-2010 12:17:55  |  layers\20030514\data_20030514_050_082_d.mat
12-Jul-2010 11:53:47  |  layers\19990525\may25_99.018-may25_99.021.mat
12-Jul-2010 11:52:27  |  layers\19990525\may25_99.014-may25_99.018.mat
12-Jul-2010 11:36:55  |  layers\19990521\may21_99.023-may21_99.029.mat
12-Jul-2010 11:25:00  |  layers\19990521\may21_99.029-may21_99.034.mat
12-Jul-2010 10:59:24  |  layers\19990521\may21_99.017-may21_99.023.mat
12-Jul-2010 10:53:38  |  layers\20030514\data_20030514_050_082_i.mat
12-Jul-2010 10:13:41  |  layers\20030514\data_20030514_050_082_k.mat
01-Jun-2010 09:46:44  |  layers\19990518\may18_99.014-may18_99.018.mat
01-Jun-2010 09:26:58  |  layers\19990514\may14_99.011-may14_99.015.mat
01-Jun-2010 09:11:25  |  layers\20030514\data_20030514_050_082_j.mat
01-Jun-2010 09:04:11  |  layers\20020530\may30_02.121-may30_02.128.mat
01-Jun-2010 09:01:33  |  layers\19990514\may14_99.015-may14_99.018.mat
01-Jun-2010 08:42:29  |  layers\20030515\data_20030515_008_032_g.mat
31-May-2010 21:48:21  |  layers\19990518\may18_99.003-may18_99.007.mat
31-May-2010 21:42:48  |  layers\20030514\data_20030514_050_082_c.mat
31-May-2010 21:33:41  |  layers\19990518\may18_99.007-may18_99.010.mat
31-May-2010 17:22:56  |  layers\20020524\may24_02.131-may24_02.146.mat
31-May-2010 17:09:19  |  layers\20070917\data_20070917_e.mat
31-May-2010 17:06:30  |  layers\19950522\may22_95.008-may22_95.009.mat
31-May-2010 16:59:18  |  layers\20070912\data_20070912_h.mat
```

Figure 11.1: **(a)** An interactive list of previously analyzed layers ease the process of correcting errors when they arise as consecutively analyzed flight lines reach back to the 2007 NGRIP-NEEM traverse. **(b)** Blue lines signify lines that have yet to be analyzed whereas red lines signify those already analyzed. Ice core drilling sites are marked by purple stars. from south to north: Dye3, GRIP, NGRIP, NEEM, Camp Century.

2. **Analysis of isochrones:**
   Depending on the users choice of flight line either an empty echogram appears, or an echogram with previously traced lines, such as in (Fig. 11.2), appears. If an un-analyzed flight line was chosen, only the green x's would appear on the

echogram. These indicate crossings with analyzed parts of other echograms and are essentially the way consistency is maintained throughout the grid of analyzed flight lines. Above the image are the names of the files with which the crossings occur. When clicking these, .png images appear for quick reference to other files. There are 25 layers in total, of which number 22 is red, indicating that it is active, and the remaining 24 are yellow indicating that they are inactive. When a layer is active it means that the user can add points to this layer only. The user can place points by left-clicking the mouse at any location, and remove the closest point by right-clicking the mouse in the vicinity of the undesired point or right-click-dragging a box on a series of undesired points. Pressing +/- allows the user to cycle through the 25 layers. Pressing 'u' allows for cycling through 4 drawmodes for the echogram, 1 being the 'raw' image and 2-4 being various filtered and alternatively colored drawmodes which sometimes allow for localization of very faint layers. The program even features undo (ctrl+z), redo (ctrl+y) and save (ctrl+s) options. Data is saved into a structure in which each point is represented by latitude, longitude and true depth with respect to the surface. When layers become indiscernible in faint data one has the option of adding a single 'nan'. Such regions of indiscernible layers can be seen in (Fig. 11.2) for the deeper isochrones.

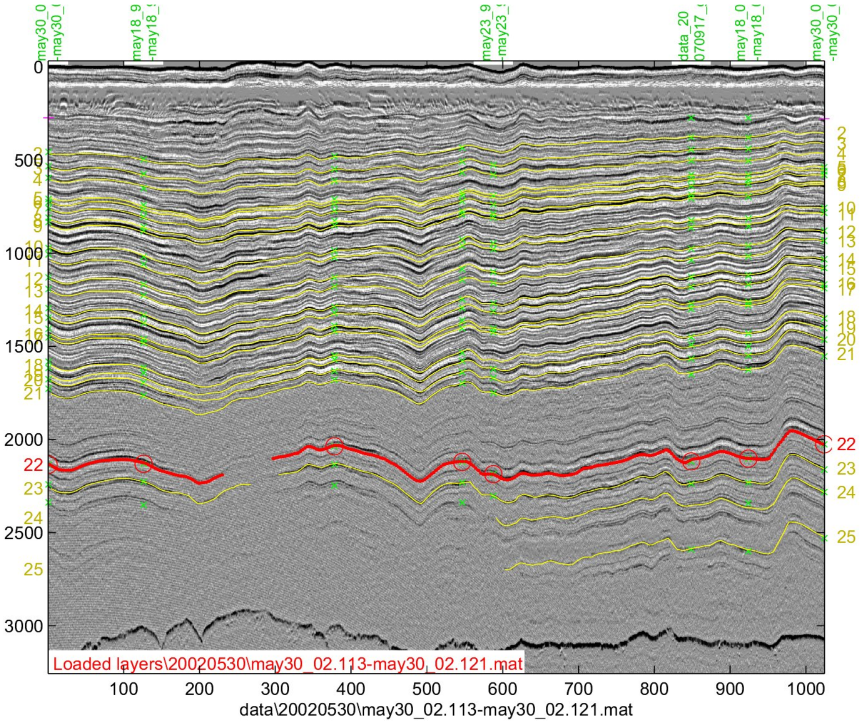

Figure 11.2: Analysis of an echogram

3. **Autotrace**
An especially handy feature of the program is an autotrace function. This feature, which is activated by pressing 'a', allows for automatic tracing of isochrones. When activated the routine saves the greyscale shading of the pixel marked by the

position of the mouse, and for each pixel in the entire picture calculates the color-shading variance in 21 directions (covering $-45°$ to $45°$) along 15 points centered around each individual pixel (See Fig. 11.3). Thus for each pixel, a likely path, based on its greyscale shading, is established, and can be drawn automatically. It is only necessary to perform the search for most likely paths for each pixel once for each echogram. Of course this process is highly dependent on the clarity of the isochrone being traced. To avoid problems in case of obscured isochrones, the routine picks up on the pattern of surrounding isochrones already traced out and corrects to fit the general pattern. Another approach to assisting the routine along obscured paths is tracing single points at key locations along the path as the routine is required to track paths such that end-points along automatically traced paths, and individual points already traced, coincide. An obvious drawback is the routines inability to trace paths with an inclination not covered by the $-45°$ to $45°$ span, for which tracing will have to be done manually.

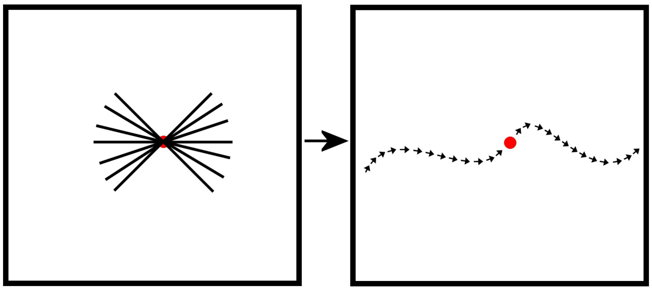

Figure 11.3: Autotrace function. **Left:** 21 lines covering the $-45°$ to $45°$ span, each with a 15 point colorshading variance. **Right:** Path achieved based on the most likely direction of the 21 for each pixel in the entire echogram.

12 The Second Appendix

Below is a list of ages and depths at NGRIP for the 25 isochrones analyzed as part of this study. Their depths are illustrated in Fig. (12.1). The difference in 2D and 3D data are caused by a re-analysis, and consequent re-dating, of the data provided by [Buchardt, 2009] for use in the 3D model. and consequently

age (b2k)	Depth (m)
1371	273.5
1951	372.4
2360	440.9
2736	501.1
3180	570.6
3348	596.7
3519	622.7
3790	663.6
3962	688.9
4775	803.3
5043	839.3
5913	954.6
6283	1000.7
7105	1101.4
7487	1146.3
8157	1221.2
8555	1259.9
10162	1396.2
11409	1476.6
12567	1517.1
14587	1599.9
37716	2054.7
45035	2182.5
50979	2284.3
74603	2552.8

age (b2k)	Depth (m)
1372	273.6
1981	377.9
2379	444.1
2728	499.9
3180	570.6
3366	599.2
3529	624.2
3796	664.4
3938	685.4
4775	803.3
5058	841.3
5927	956.5
6271	999.1
7105	1101.4
7496	1147.4
8180	1223.5
8567	1261.2
10092	1391.1
11073	1456.8
12515	1515.7
14365	1588.5
37758	2055.9
44705	2177.0
50440	2275.2
72241	2534.8

Table 3: Ages and depths at NGRIP for all isochrones used in this study in the **Left:** 2D case provided by [Buchardt, 2009], and the **Right:** 3D case. The very final age surpasses the 60202 b2k age limit in the GICC05 timescale and have therefore been dated by extrapolating the GICC05 timescale with the NGRIP ss09sea flow model [Vinther, B. - Personal communication]

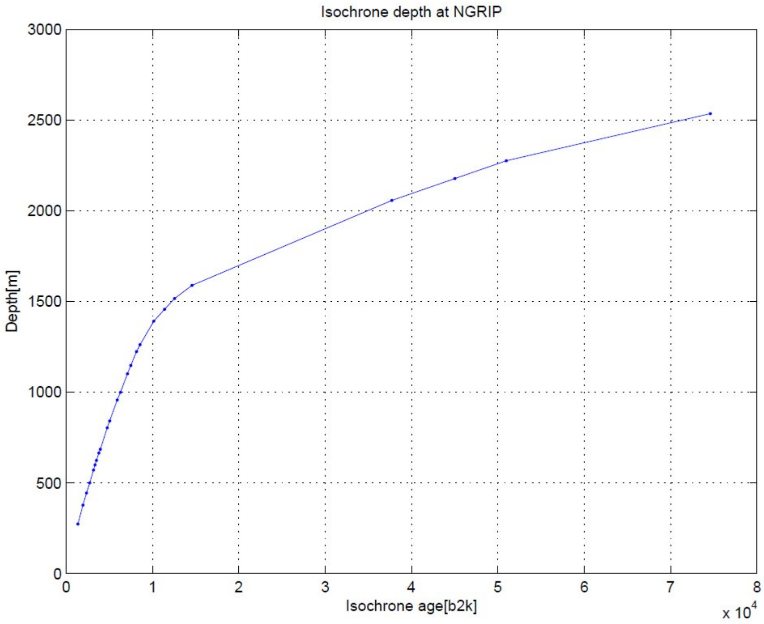

Figure 12.1: Depth of Isochrones at NGRIP

13 The Third Appendix

Determining **C** involves a series of steps:

2D case:

1. Create a number of surrogate datasets n by taking the raw isochrone data R and adding:
    - a general vertical red noise n_r^{radar} with standard deviation 4.2, corresponding to the uncertainty in radar depth as described in section 4.1, and a decorrelation length of $1 \cdot 10^3$.
    - a general vertical red noise n_r^{trace} with standard deviation 2.0, corresponding to an uncertainty in tracing of the isochrones and a decorrelation length of $1 \cdot 10^3$.
2. Interpolate from each surrogate dataset to p_{grid}, hereby determining n isochrone depths for each point in p_{grid}. Arrange the results in a matrix F with n columns of isochrone depths.
3. normalize each column by subtracting its mean value.
4. Take the covariance of F to determine C.

3D case:

1. Create a number of surrogate datasets n by taking the raw isochrone data R and adding:
    - a general vertical red noise n_r^{radar} with standard deviation 4.2, corresponding to the uncertainty in radar depth as described in section 4.1, and a decorrelation length of $1 \cdot 10^4$.
    - a general vertical red noise n_r^{trace} with standard deviation 2.0, corresponding to an uncertainty in tracing of the isochrones, and a decorrelation length of $1 \cdot 10^4$.
2. Perform gridding by kriging on each surrogate dataset, as described in 5.1.
3. Interpolate from each gridded surrogate dataset to p_{grid}, hereby determining n isochrone depths for each point in p_{grid}. Arrange the results in a matrix F with n columns of isochrone depths.
4. normalize each column by subtracting its mean value.
5. Take the covariance of F to determine C.

References

[Bamber et al., 2000] Bamber, J., Hardy, R., and Joughin, I. (2000). An analysis of balance velocities over the greenland ice sheet and comparison with synthetic aperture radar interferometry. *Journal of Glaciology*, 46(152):67–74.

[Bamber et al., 2001] Bamber, J., Layberry, S., and Gogineni, S. (2001). A new ice thickness and bed data set for the greenland ice sheet. *Journal of Geophysical Research*, 106(D24):33773–33788.

[Bjerrum, 1951] Bjerrum, N. (1951). Structure and properties of ice. *Kongelige Danske Videnskabernes Selskab - Matematiske-Fysiske meddelelser*, 27:1–56.

[Buchardt, 2009] Buchardt, S. (2009). *Basal Melting and Eemian ice along the main ice ridge northern Greenland.* PhD thesis, Centre for Ice and Climate, University of Copenhagen, Denmark.

[Clough, 1977] Clough, J. (1977). Reflections from internal layers in ice sheets. *Journal of Glaciology*, 18(78):3–14.

[Dowdeswell and Evans, 2004] Dowdeswell, J. and Evans, S. (2004). Investigations of the form and flow of ice sheets and glaciers using radio-echo sounding. *Reports on Progress in Physics*, 67(2004):1821–1861.

[Ettema et al., 2009] Ettema, J., van den Broeke, M., van Meigaard, E., van de Berg, W., Bamber, J., Box, J., and Bales, R. (2009). Higher surface mass balance of the greenland ice sheet revealed by high-resolution climate modeling. *Geophysical Research Letters*, 36(L12501).

[Fujita and Mae, 1994] Fujita, S. and Mae, S. (1994). Causes and nature of ice-sheet radio-echo internal reflections estimated from the dielectric properties of ice. *Annals of Glaciology*, 20:80–86.

[Glen and Paren, 1975] Glen, J. and Paren, J. (1975). The electrical properties of snow and ice. *Journal of Glaciology*, 15(73):15–37.

[Gogineni et al., 1998] Gogineni, S., Chuah, T., Allen, C., Jezek, K., and Moore, R. (1998). An improved coherent radar depth sounder. *Journal of Glaciology*, 44(148):659–669.

[Griffiths, 2009] Griffiths, D. (2009). *Introduction to Electrodynamics - 3rd ed.* Pearson.

[Gruber and Ludwig, 1996] Gruber, S. and Ludwig, F. (1996). Application of ground penetrating radar in glaciology and permafrost prospecting.

[Hammer, 1980] Hammer, C. U. (1980). Acidity of polar ice cores in relation to absolute dating, past volcanism, and radio-echos. *Journal of Glaciology*, 25(93):359–372.

[Harrison, 1973] Harrison, C. H. (1973). Radio echo sounding of horizontal layers in ice. *Journal of Glaciology*, 12(66):383–397.

[Hecht, 2008] Hecht, E. (2008). *Optics - 4th ed.* Pearson.

[Hempel et al., 2000] Hempel, L., Thyssen, F., Gundestrup, N., Clausen, H. B., and Miller, H. (2000). A comparison of radio echo sounding data and electrical conductivity of the grip ice core. *Journal of Glaciology*, 46(154):369–374.

[Joughin et al., 2010] Joughin, I., Smith, B., Howat, I., Scambos, T., and Moon, T. (2010). Greenland flow variability from ice-sheet-wide velocity mapping. *Journal of Glaciology*, 56(197):416–430.

[Letreguilly et al., 1991] Letreguilly, A., Huybrechts, P., and Reeh, N. (1991). Steady-state characteristics of the greenland ice sheet under different climates. *Journal of Glaciology*, 37(125):149–157.

[Metropolis et al., 1953] Metropolis, N., Rosenbluth, A., Rosenbluth, M., Teller, A., and Teller, E. (1953). Equations of state calculations by fast computing machines. *Journal of Chemical Physics*, 21(6):1087–1092.

[Metropolis and Ulam, 1949] Metropolis, N. and Ulam, S. (1949). The monte carlo method. *Journal of the American Statistical Association*, 44(247):335–341.

[Millar, 1981] Millar, D. (1981). Radio-echo layering in polar ice sheets and past volcanic activity. *Nature*, 292(5822):441–443.

[Mosegaard, 1998] Mosegaard, K. (1998). Resolution analysis of general inverse problems through inverse monte carlo sampling. *Inverse Problems*, 14:405–426.

[Mosegaard and Sambridge, 2002] Mosegaard, K. and Sambridge, M. (2002). Monte carlo analysis of inverse problems. *Inverse Problems*, 18:R29–R54.

[Mosegaard and Tarantola, 1995] Mosegaard, K. and Tarantola, A. (1995). Monte carlo sampling of solutions to inverse problems. *Jounal of Geophysical Research*, 100 B7:12431–12447.

[Mosegaard and Tarantola, 2002] Mosegaard, K. and Tarantola, A. (2002). Probabilistic approach to inverse problems. *International Handbook of Earthquake and Engineering Seismology*, 81A:237–265.

[Nourani and Andresen, 1998] Nourani, Y. and Andresen, B. (1998). A comparison of simulated annealing cooling strategies. *Journal of Physics A: Mathematical and General*, 31:8373–8385.

[Paden et al., 2010] Paden, J., Akins, T., Dunson, D., Allen, C., and Gogineni, P. (2010). Ice-sheet bed 3-d tomography. *Journal of Glaciology*, 56(195).

[Paren and Robin, 1975] Paren, J. G. and Robin, G. d. Q. (1975). Internal reflections in polar ice sheets. *Journal of Glaciology*, 14(71):251–259.

[Patterson, 1994] Patterson, W. (1994). *The Physics of Glaciers - 3rd ed.* Butterworth-Heinemann.

[Pauling, 1935] Pauling, L. (1935). The structure and entropy of ice and of other crystals with some randomness of atomic arrangement. *Journal of the American Chemical Society*, 57:2680–2684.

[Petrenko and Whitworth, 1999] Petrenko, V. and Whitworth, R. (1999). *Physics of ice*. Oxford.

[Plewes and Hubbard, 2001] Plewes, L. and Hubbard, B. (2001). A review of the use of radio-echo sounding in glaciology. *Progress in Physical Geography*, 25(2):203–236.

[Press et al., 2007] Press, W., Teukolsky, S., Vetterling, W., and Flannery, B. (2007). *Numerical Recipes - 3rd ed.* Cambridge University Press.

[Schwanghart and Kuhn, 2010] Schwanghart, W. and Kuhn, N. (2010). Topotoolbox: A set of matlab functions for topographic analysis. *Environmental Modelling and Software*, 25:770–781.

[Simonsen et al., 2010] Simonsen, S., Soerensen, L., Nielsen, K., Lucas-Picher, P., Spada, G., Adalgeirsdottir, G., Forsberg, R., and Hvidberg, C. (2010). Mass balance of the greenland ice sheet, a study of icesat data, surface density and firn compaction modelling. *The Cryosphere Discuss.*, 4:2103–2141.

[Tarantola, 2005] Tarantola, A. (2005). *Inverse problem theory and methods for model parameter estimation*. SIAM.

[Vinter et al., 2009] Vinter, B., Buchardt, S., Clausen, H., Dahl-Jensen, D., Johnsen, S., Fisher, D., Koerner, R., Raynaud, D., Lipenkov, V., Andersen, K., Blunier, T., Rasmussen, S., Steffensen, J., and Svensson, A. (2009). Holocene thinning of the greenland ice sheet. *Nature*, 461.

[Vinter et al., 2006] Vinter, B., Clausen, H., Johnsen, S., Rasmussen, S., Andersen, K., Buchardt, S., Dahl-Jensen, D., Seierstad, I., Siggaard-Andersen, M.-L., Steffensen, J., Svensson, A., Olsen, J., and Heinemeier, J. (2006). A synchronized dating of three greeland ice cores throughout the holocene. *Journal of Geophysical Research*, 111(D13102).

[Waite and Schmidt, 1962] Waite, A. H. and Schmidt, V. (1962). Gross errors in height indication from pulsed radar altimeters operating over thick ice or snow. *Proc. Inst. Radio Engineers*, 50(6):1515–1520.